Supplementary Information

# Polyamide Nanofilms with Janus Microporous Framework for Sustainable Solvent Filtration

Fuxin Zheng,[1] Zhenxiang Pan,[1] Yu Liao,[1] Jiang Zhan,[1] Songjun Fang,[1] Jiandong Pang,[2] Tong Zhang,[1,*] and Gang Han[1,*]

[1]College of Environmental Science and Engineering, Tianjin Key Laboratory of Environmental Remediation and Pollution Control, Nankai University, 38 Tongyan Road, Tianjin, 300350 China

[2]School of Materials Science and Engineering, Smart Sensing Interdisciplinary Science Center, Collaborative Innovation Center of Chemical Science and Engineering, Nankai University, 38 Tongyan Road, Tianjin, 300350 China

**[*]Corresponding author. Email: zhangtong@nankai.edu.cn (T.Z.); hangang@nankai.edu.cn (G.H.)**

**Supplementary Information includes Supplementary Methods, 64 Figures, and 14 Tables**

## Supplementary Methods

### Supplementary Note 1. Chemical and materials

Trimesoyl chloride (TMC, 98.0%), 4,4'-diaminodiphenyl ether (ODA, 98.0%), 4,4'-oxybis(3-(trifluoromethyl)aniline) (6FODA, 99.0%), and 2,2'-bis(trifluoromethyl)benzidine (PFMB, 98.0%) ordered from Macklin (Shanghai, China) were used as the monomers to synthesize the polyamide nanofilms and the polyamide thin-film composite (TFC) membranes via interfacial polymerization. 1-butyl-3-methylimidazolium tetrafluoroborate ($[C_4mim]BF_4$, 99.0%) and hexane (98.0%) purchased from Macklin were used as the solvents for the monomers during interfacial polymerization. Methanol, ethanol, isopropanol (IPA), acetone, tetrahydrofuran (THF), toluene, hexane, and heptane were obtained from Macklin as representative solvents for membrane performance tests. Azobenzene (ABZ), methyl red (MR), methyl orange (MO), orange G (OG), eriochrome black T (EBT), indigo carmine (INCA), acid fuchsin (AF), congo red (CR), methylene blue (MB), crystal violet (CV), rhodamine B (RB), victoria blue B (VBB), alcian blue 8GX (AB), and vitamin B12 (VB12) from Macklin were used as the model solutes for molecular separation experiments. Bisphenol A (BPA), sulfadiazine (SDZ), ciprofloxacin (CIP), carbenicillin disodium (CBD), moxifloxacin hydrochloride (MHX), doxycycline hydrochloride (DC), oxytetracycline (OTC), cefotaxime sodium salt (CS), tetracycline hydrochloride (TC), and clindamycin phosphate (CLP) were obtained from Macklin as model solutes for drug molecule separation experiments. Potassium chloride (KCl), hydrochloric acid (HCl), and sodium hydroxide (NaOH) obtained from Macklin were used for surface zeta potential measurements. Glycerol and diiodomethane were ordered from Macklin for surface contact angle measurements. Dimethyl sulfoxide (DMSO) and acetonitrile were obtained from Macklin for membrane solvent stability tests. Polyacrylonitrile (PAN) ultrafiltration membrane with a molecular weight cutoff of 100 kDa from Lanjing Membrane Technology Co., Ltd., China was used as the substrate for preparing the polyamide TFC membranes. N,N-dimethylformamide (DMF) purchased from Macklin was used to isolate the

polyamide layer of the TFC membrane by dissolving the PAN substrate. Unless otherwise specified, all chemicals and reagents were used as received without further purification. Deionized water was supplied by a Millipore-D 24 UV ultrapure water integrated system (Millipore Instruments, 18.2 MΩ cm).

**Supplementary Note 2. Characterization**

**Scanning electron microscopy (SEM).** The membrane surface morphology was observed on a field emission scanning electron microscope (FESEM, ESCALAB 250Xi, Thermo Scientific, USA) with an accelerating voltage of 5 kV. All membrane samples were sputtered with a gold coating of approximately 5 nm in thickness to prevent surface charging.

**Atomic force microscopy (AFM).** The surface morphology and roughness of polyamide nanofilms and membranes were examined by atomic force microscopy (AFM, NanoWizard 4, Bruker, Germany). AFM images were processed with a sampling resolution of at least 512 points per line at a speed of 0.2 to 1 Hz. AFM images were analyzed using the NanoScope Analysis 3.00 software.

**Fourier transform infrared spectroscopy (FTIR).** The characteristic chemical functional groups of polyamide nanofilms were characterized using Fourier transform infrared spectroscopy (FTIR, Nicolet IN10, Thermo Fisher, USA) in attenuated total reflection (ATR) mode. 32 scans were performed for each sample with a wavenumber range of 600 to 4000 $cm^{-1}$ and a resolution of 4 $cm^{-1}$.

**X-ray photoelectron spectroscopy (XPS).** The elemental and chemical characteristics of polyamide nanofilms were analyzed by X-ray photoelectron spectroscopy (XPS, Escalab 250Xi, Thermo Fisher, USA) using a monochromatic Al-Kα X-ray source (hν = 1486.6 eV). High-resolution scans of the C, N, O, and F regions were performed in an increment of 0.5 eV, and the XPS peaks were fitted using the Advantage software.

**Raman spectroscopy.** The chemical structure of polyamide nanofilms was characterized using Raman spectroscopy (XploRA PLUS, Horiba, Japan). All spectra were recorded under the conditions of an excitation wavelength of 532 nm, a laser power of not less than 50 mW, and a spectral range of 500 to 2000 $cm^{-1}$.

**X-ray diffraction (XRD).** The *d*-spacing values of polyamide powders were determined by X-ray diffractometer (XRD, D8 Discover, Germany) scanning from 5–40° (2θ) at a speed of 6° per min.

**Gas sorption.** The carbon dioxide ($CO_2$) and nitrogen ($N_2$) adsorption-desorption isotherms of polyamide powders were measured on an automated gas sorption analyzer (ASAP 2460, Micromeritics, USA) at 273 and 77 K, respectively. The Brunauer-Emmett-Teller specific surface area was calculated using the Micromeritics software based on the Langmuir theory, and the pore size distribution was obtained using the nonlocal density functional method. Before the test, the membrane samples were degassed under vacuum at 120 °C for 12 h.

**Surface contact angle.** The surface contact angles of the membranes with water, glycerol, and diiodomethane were measured at room temperature using a contact angle goniometer (HARKE-SPCA, HARKE, China). At least six readings were taken at random locations on each membrane sample, and the average value was reported.

**Vapor sorption.** The sorption isotherms of methanol and hexane vapors on polyamide powder were acquired on a gas and vapor adsorption analyzer (BELSORP-max II, MicrotracBEL, Japan) at 25 °C. In the isotherm experiments, each pressure change was maintained for at least 1 h to reach a steady state. The vapor pressure of each solvent at the operating temperature was calculated using the Antoine equation.

**Zeta potential.** The surface zeta potential of polyamide membranes was measured on a SurPASS electrokinetic analyzer (SurPASS 3, Anton Paar, Austria) using 1 mM KCl solution as the background electrolyte. The solution pH was adjusted with HCl and NaOH buffer solutions.

For characterizations requiring dried samples, membrane samples were thoroughly washed with deionized water and then dried in a freeze dryer under vacuum.

**Supplementary Note 3. Transfer and thickness measurement of free-standing polyamide nanofilms**

The polyamide TFC membrane (top polyamide layer facing up) and silicon wafer were carefully placed in a petri dish, and then DMF was slowly added. After soaking in DMF for 20 min, the PAN substrate layer dissolved and the nonwoven fabric was removed, leaving a free-standing polyamide nanofilm floating on the surface. The solution in the petri dish was slowly removed, and the nanofilm was washed three times with DMF, methanol, and water, respectively. Afterwards, the excess solution was discarded, and the polyamide nanofilm was deposited on a silicon wafer, which was subsequently dried under vacuum at 30 °C overnight. The thickness of the polyamide nanofilm was then measured by scanning the height drop at the junction of the film and the silicon substrate using AFM.

**Supplementary Note 4. Calculation of the crosslinking degree of polyamide nanofilms**

Based on the molecular structure shown in Supplementary Fig. 23, the crosslinking degree (x) of the polyamide nanofilm was calculated using the O/N atomic ratio obtained from XPS elemental analysis (Supplementary Table 1). x and y represent the proportion of the fully crosslinked and incompletely crosslinked portions of the polyamide, respectively. The crosslinking degree was calculated as follows[1]:

$$x + y = 1 \tag{S1}$$

For ODA-M and 6FODA-M:

$$\frac{O}{N} = \frac{4x + 5y}{3x + 2y} \tag{S2}$$

For PFMB-M:

$$\frac{O}{N} = \frac{3x + 4y}{3x + 2y} \tag{S3}$$

**Supplementary Note 5. Membrane stability tests**

**Long-term performance stability test.** The methanol permeance and INCA rejection of the 6FODA-M membrane were tested at 3 bar for 120 h using a 50 ppm INCA methanol solution as the feed to evaluate the long-term stability of the polyamide membrane.

**Pressure stability test.** The methanol permeance and INCA rejection of the 6FODA-M membrane were measured over the operating pressure range of 2 to 15 bar using a 50 ppm INCA methanol solution as the feed to evaluate the pressure stability of the polyamide membrane.

**Solute concentration stability test.** The methanol permeance and INCA rejection of the 6FODA-M membrane were tested at 3 bar using methanol solutions containing 25 to 200 ppm INCA as the feed to evaluate the membrane stability against dye concentration.

**Solvent resistance stability test.** The 6FODA-M membrane was immersed in water, DMF, DMSO, acetonitrile, methanol, ethanol, IPA, acetone, THF, toluene, hexane, and heptane for 7 days, respectively. After cleaning with methanol, the solvent permeance and INCA rejection were measured at 3 bar using a 50 ppm INCA methanol solution as the feed to evaluate the solvent stability of the polyamide membrane. In addition, the solvent permeance and INCA rejection of the 6FODA-M membrane were tested at 3 bar using 50 ppm INCA solution in methanol, acetone, and hexane as the feed, respectively, to evaluate the membrane stability upon switching between organic solvents with different polarities.

**Supplementary Note 6. Surface free energy and Gibbs free energy calculations**

**Surface free energy calculation.** The surface free energy of the polyamide membrane was calculated from the surface contact angles of probe liquids using the following formula[2]:

$$\gamma_s^{\text{total}} = \gamma_s^{\text{LW}} + \gamma_s^{\text{AB}} = \gamma_s^{\text{LW}} + 2\sqrt{\gamma^+\gamma^-} \quad \text{(S4)}$$

$$(1+\cos\theta)\gamma_1^{\text{total}} = 2\left(\sqrt{\gamma_s^{\text{LW}}\gamma_1^{\text{LW}}} + \sqrt{\gamma_s^+\gamma_1^-} + \sqrt{\gamma_s^-\gamma_1^+}\right) \quad \text{(S5)}$$

where $\gamma_s^{\text{total}}$ and $\gamma_l^{\text{total}}$ are the surface free energies of the membrane and liquid, respectively. LW and AB represent the components of the nonpolar and polar interactions, respectively. + and − are the electron acceptor and electron donor components of polar interactions, respectively. θ is the contact angle of the test liquid on the membrane surface. The surface energy-related parameters of the three tested liquids are shown in Supplementary Table 3.

**Gibbs free energy calculation.** The Gibbs free energy (ΔG) was calculated to reveal the interactions of polyamide with hexane, which was determined by the following equations[2]:

$$\Delta G = \Delta G^{\text{LW}} + \Delta G^{\text{AB}} \quad \text{(S6)}$$

$$\Delta G^{LW} = -2\left(\gamma_3^{LW} + \sqrt{\gamma_1^{LW}\gamma_2^{LW}} - \sqrt{\gamma_1^{LW}\gamma_3^{LW}} - \sqrt{\gamma_2^{LW}\gamma_3^{LW}}\right) \quad \text{(S7)}$$

$$\Delta G^{\text{AB}} = -2\left\{\sqrt{\gamma_1^+\gamma_2^-} + \sqrt{\gamma_2^+\gamma_1^-} - \sqrt{\gamma_3^+}\left(\sqrt{\gamma_1^-} + \sqrt{\gamma_2^-} - \sqrt{\gamma_3^-}\right) - \sqrt{\gamma_3^-}\left(\sqrt{\gamma_1^+} + \sqrt{\gamma_2^+} - \sqrt{\gamma_3^+}\right)\right\} \quad \text{(S8)}$$

where subscripts 1, 2, and 3 represent the surface tension parameters of hexane, membrane, and water, respectively. For example, $\gamma_2^{\text{LW}}$ represents the nonpolar component parameter of the membrane surface tension. The subscript "total" represents the total energy, and LW and AB are the Lifshitz–van der Waals and acid-base interaction components of the total energy, respectively.

**Supplementary Note 7. Calculation and comparison of the relative affinity (distance) between organic solvents and polyamide membranes**

The affinity of organic solvents to polyamide membranes was analyzed by calculating the relative distance between the Hansen solubility parameters (HSP) of the solvents and diamine monomers/polyamide fragments in the HSP comparison diagram[3]. The relative affinity obtained is a vector value that was calculated by:

$$\text{Relative affinities} = \overrightarrow{\text{SM}} = \sqrt{(\delta_{\text{ds}} - \delta_{\text{dm}})^2 + \left(\delta_{\text{ps}} - \delta_{\text{pm}}\right)^2 + (\delta_{\text{hs}} - \delta_{\text{hm}})^2} \qquad \text{(S9)}$$

where $\delta_d$, $\delta_p$, and $\delta_h$ represent the dispersion, polar, and hydrogen bonding force components of the Hansen solubility parameter ($\delta$), respectively. The s and m represent solvent and monomers/polyamide fragments, respectively.

**Supplementary Note 8. Density functional theory (DFT) calculations**

DFT calculations were performed with the ORCA quantum chemistry software version 5.0.4[4]. The B3LYP functional was adopted for the calculations in tandem with the D3BJ dispersion correction[5, 6]. Geometry optimization and single-point calculations were performed using the def2-SVP and def2-TZVP basis sets, respectively, following the AutoAux generation procedure[7]. Conformation searches were performed using the gfn2-xtb method in the xtb software. The 100 conformations obtained were optimized and their energies were calculated. Structures with similar energies (energy threshold = 1 kcal $mol^{-1}$) and similar structures (geometry threshold = 1 Å) were identified as the same structure. Typical polyamide molecular fragments of 6FODA-M, ODA-M, and PFMB-M were constructed, and the single-point energies were calculated after geometry optimization. The binding conformations of different solvent molecules (methanol, acetone, and hexane) with polyamide fragments were subsequently optimized, and the calculated single-point energies were converted to binding energies. Specifically, the binding energy was calculated as $E_B = E_{total} - E_{PA} - E_{sol}$, where $E_{total}$ represents the total energy of polyamide fragments with the solvent molecules, $E_{PA}$ is the energy of polyamide fragments, and $E_{sol}$ refers to the energy of solvent molecules. Moreover, the adsorption energies ($\Delta E_{ads}$) were calculated as $\Delta E_{ads} = E_{total} - E_{sub} - E_{hexane}$, where $E_{total}$ is the total energy of hexane adsorbed on the representative polyamide fragments, $E_{sub}$ is the total energy of polyamide fragments, and $E_{hexane}$ is the energy of adsorbed hexane. The energy required for hexane to desorb from the surface of the polyamide fragments could be calculated as $\Delta E_{des} = E_s - E_u$, where $\Delta E_{des}$ is the desorption energy, $E_s$ is the total energy of hexane on polyamide fragments, and $E_u$ is the total energy of hexane at an infinite distance. The distribution of electrostatic potential (ESP), average local ionization energy (ALIE), local electron attachment energy (LEAE), Fukui function, nucleophilicity index, and energy levels of the highest occupied molecular orbital (HOMO) and lowest unoccupied molecular orbital (LUMO) of the monomer were analyzed using the Multiwfn software package[8, 9]. Subsequently, the RESP and EEM charges of the structure were analyzed using the Multiwfn software package, and the electrostatic potential

was projected onto a two-dimensional space[10]. The B3LYP functional with D3BJ dispersion corrections was applied for all calculations. Geometry optimization and single-point energy calculations were carried out using the def2-TZVP basis set. After the geometry optimization was completed, single-point energy calculations were performed. Both geometry optimization and single-point energy calculations were conducted in a vacuum environment. All visualization images were generated by the Visual Molecular Dynamics (VMD, Version 1.9.3) software and VESTA[11].

**Dihedral angle calculation of diamine monomers.** The molecular geometries of the diamine monomers (ODA, 6FODA, and PFMB) were optimized using DFT as implemented in the ORCA 5.0.4 software package. Geometric optimizations were performed at the B3LYP/def2-SVP level of theory without any symmetry constraints, and all optimized structures were confirmed to be true energy minima by the absence of imaginary frequencies in harmonic oscillation analyses. To quantitatively describe the torsional relationship between adjacent aromatic rings, the inter-benzene dihedral angle was determined from the optimized geometries using the Multiwfn program. The dihedral angle was defined by four atoms (C1–C2–X–C3), where C2–X represents the central connecting bond (X = O for ODA and 6FODA, X = C for PFMB), and C1 and C3 are the ortho-carbon atoms adjacent to the linking atom in each benzene ring.

**Torsional energy barrier calculation of PA fragments.** Representative structural fragments of ODA-M and 6FODA-M PAs were constructed to assess the torsional flexibility of the polymer backbone. Each PA fragment consists of two benzene rings connected by an amide linkage and an ether linkage, corresponding to the repeating structural motifs in the polymer chains. All calculations were performed using the ORCA 5.0.4 quantum chemistry package. The B3LYP functional with D3BJ dispersion corrections was adopted for all calculations. Geometric optimizations and single-point energy refinements were conducted at the def2-SVP and def2-TZVP levels, respectively, following the AutoAux procedure. All computations were performed in the gas phase without solvation models. Three representative rotatable bonds were selected in each

PA fragment: the C–N–C–C around the amide linkage and the C–O–C–C around the ether linkage. Torsional energy profiles were obtained by incrementally rotating the selected dihedral angles from 0° to 360° in 10° steps. For each torsion site, 36 conformations were generated, resulting in a total of 108 conformations per system (three torsion sites × 36 steps), followed by a single-point energy calculation at the def2-TZVP level. The relative torsional energy barrier (ΔE) was defined as: $\Delta E = E_{torsion} - E_{min}$, where $E_{torsion}$ is the energy of the conformation at a given dihedral angle, and $E_{min}$ is the global minimum energy of the optimized fragment. All energies are reported in $kJ \cdot mol^{-1}$.

**Supplementary Note 9. Molecular dynamics (MD) simulations**

**Polymerization simulation methods.** Monomer molecular models were constructed and described using the general AMBER force field[12]. 1050 TMC molecules and 1575 ODA/6FODA/PFMB molecules were packed in a cubic cell of size 100 Å with a low density of 0.4 g $cm^{-3}$. The chlorines in TMC molecules and the amino hydrogens in ODA/6FODA/PFMB molecules were removed. Carbons of carbonyls in TMC molecules and nitrogens in ODA/6FODA/PFMB molecules were marked with a tag, and then the polymerization steps were performed between the tagged carbons and nitrogens within a cut-off of 6 Å, using energy minimization and molecular dynamics (MD) steps to adjust the molecules. Unreacted carbonyls and amine ends were restored to chlorines and hydrogens. GROMACS 2023.2 was used in the MD steps for both polymerization and equilibrium[13]. Zeo++ was used to analyze fractional free volume and accessible surface, with a probe radius of 0.6, 1.0, and 1.8 Å, respectively. Zeo++ was used to analyze voids, pore size distribution, and surface area[14].

**MD Parameters.** All all-atom MD simulations were based on a general AMBER force field with RESP charges and were conducted using the Gromacs-2023.2 software package. The system was a relaxed liquid configuration at 298 K. The total run time for the equilibrium MD simulation was 50 ns NPT. We used the relaxed system as a starting configuration. As it is prior to system relaxation MD, energy minimization was carried out with a composite protocol of steepest descent using termination gradients of 100 kJ $mol^{-1}$ $nm^{-1}$. The equilibrium temperature was maintained at 298 K using a Nose′-Hoover thermostat, and periodic boundary conditions were imposed on all three dimensions[15]. The Particle Mesh-Ewald method was used to compute the long-range electrostatics within a relative tolerance of $1\times10^{-6}$ [16]. A cut-off distance of 1nm was applied to real-space Ewald interactions. The same value was used for van der Waals interactions. The LINCS algorithm was applied to constrain the bond lengths of hydrogen atoms[17]. A leap-frog algorithm was used with a time step of 2 fs[18].

Conformational dynamics of polyamide polymer fragments. To observe the conformational dynamics of the $–CF_3$ groups in the polyamide at the macroscopic scale, a polymer fragment comprising 15 TMC and 31 amine monomers was constructed. These monomers reacted to form a crosslinked network, ensuring that each amide and amine group, except for those at the edges, underwent crosslinking. The polymer was then placed in the center of a cubic simulation box with dimensions 10 nm × 10 nm × 10 nm, and the vacuum regions of the box were filled with 2000 hexane molecules to simulate a solvent environment. To better observe the group oscillations, we also constructed a polymer formed by crosslinking 1 TMC and 3 amine monomers, along with 150 hexane molecules, within a cubic simulation box of 3 nm × 3 nm × 3 nm in dimension. The calculations were performed using GROMACS version 2020.6. In these calculations, the General Amber Force Field (GAFF) was adopted, and atomic charges were assigned to each atom to more accurately describe the molecular-level motion. These atomic charges were obtained through DFT calculations and the Multiwfn program, where molecules with no more than 200 atoms were described using RESP charges, while molecules with more than 200 atoms were described using EEM charges. Before calculating the atomic charges, the molecular structures were optimized using DFT to obtain accurate results. After energy minimization and preliminary equilibration, the MD simulations were performed with the following parameters: A leap-frog integrator was employed with a timestep of 0.001 ps for a total of 20 million steps (20 ns). Holonomic constraints were applied using the LINCS algorithm, with no bond constraints imposed. Neighbor searching was performed using the Verlet cutoff scheme. Short-range electrostatic and van der Waals interactions were truncated at 1.2 nm. Long-range electrostatic interactions were calculated using the Particle Mesh Ewald (PME) method with a cubic interpolation order of 4 and a Fourier spacing of 0.16 nm. Temperature coupling was achieved using the modified Berendsen thermostat (V-rescale), maintaining the system temperature at 298.15 K, with a time constant of 0.1 ps. Pressure coupling employed the Berendsen barostat for isotropic pressure coupling, setting the reference pressure at 1.01325 bar, with a time constant of 2.0 ps. Periodic boundary conditions were enforced

in all three spatial dimensions. No initial velocity generation was applied. In addition, to determine the density of hexane molecules around the polymer, we fixed the polymer formed by the crosslinking of 1 TMC and 3 amine monomers in the center of the simulation box, orienting it along the Y-axis. Subsequently, 150 hexane molecules were added around the polymer, and the polymer was frozen. A 20 ns NVT ensemble simulation was performed without considering pressure, while all other parameters were kept consistent with the above conditions.

## Supplementary Figures

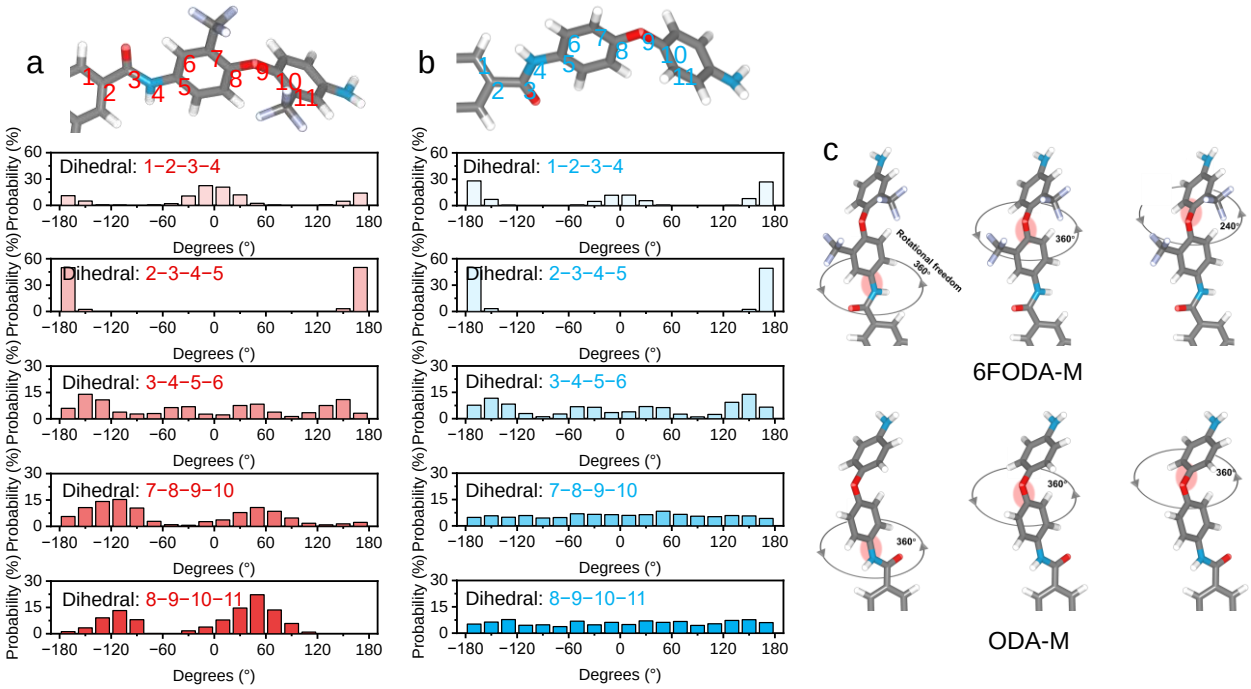


**Supplementary Fig. 1. Torsion capability analysis of 6FODA-M and ODA-M polyamide backbones. a**, **b** Distribution of the dihedral angles generated by segmental torsion at different positions of the polymer backbone of (**a**) 6FODA-M and (**b**) ODA-M polyamides. **c**, Schematic diagram of the torsion angle range at different positions of 6FODA-M and ODA-M polyamide backbones. Atoms color code: C, gray; O, red; N, blue; F, violet.

**Supplementary Note 10:** The torsion behavior of ODA-M and 6FODA-M polyamide polymer chains was assessed through DFT calculations. The results show that the benzene rings in the backbones of both polyamides can twist to a certain extent around the flexible amide and ether bonds, leading to the formation of noncoplanar structures. More specifically, 6FODA-M polyamide can rotate freely within a range of 360° at the amide bond linkages, while the torsional rotation is limited to 240° at the ether bond connections. In contrast, ODA-M polyamide can rotate freely at both the amide and ether bond positions. The restricted torsional rotation of the two benzene rings around the phenyl ether bonds in 6FODA-M polyamide mainly stems from the steric

hindrance imparted by the $–CF_3$ substituents at the ortho position. Therefore, the torsion angles of 6FODA-M are mainly concentrated at 60° and –120°. Such a highly contorted noncoplanar molecular structure is expected to generate more free volume and enhance the structural rigidity in the polyamide layer of 6FODA-M.

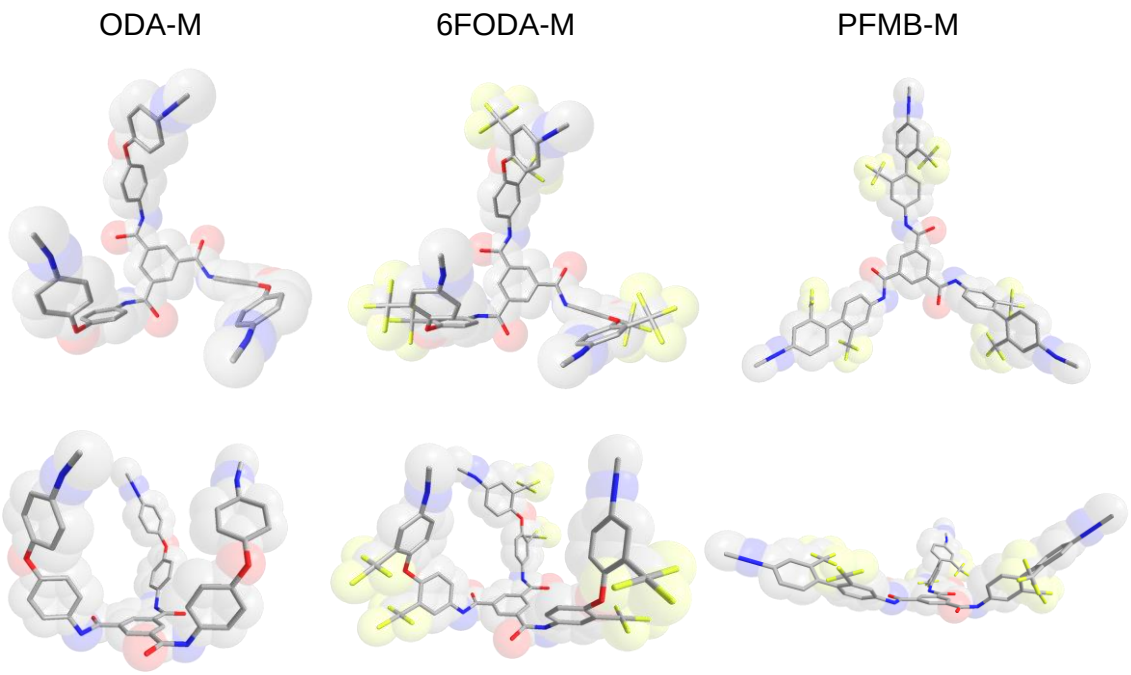


**Supplementary Fig. 2. Chemical structure of polyamide polymers.** Three-dimensional chemical structure of representative chain fragments of polyamide polymers formed by the polymerization of 6FODA (6FODA-M), ODA (ODA-M), and PFMB (PFMB-M) monomers with TMC, respectively. Atoms color code: C, gray; O, red; N, blue; F, yellow.

**Supplementary Note 11:** Owing to the torsion of the two benzene rings linked by ether bonds in the 6FODA and ODA molecules and the rotation of the benzene rings, contorted noncoplanar conformational structures are formed in the polyamide networks of 6FODA-M and ODA-M upon crosslinking with TMC during IP. In comparison, PFMB-M polyamide shows fewer contorted noncoplanar conformations due to the absence of ether bonds and less rotation between the two benzene rings.

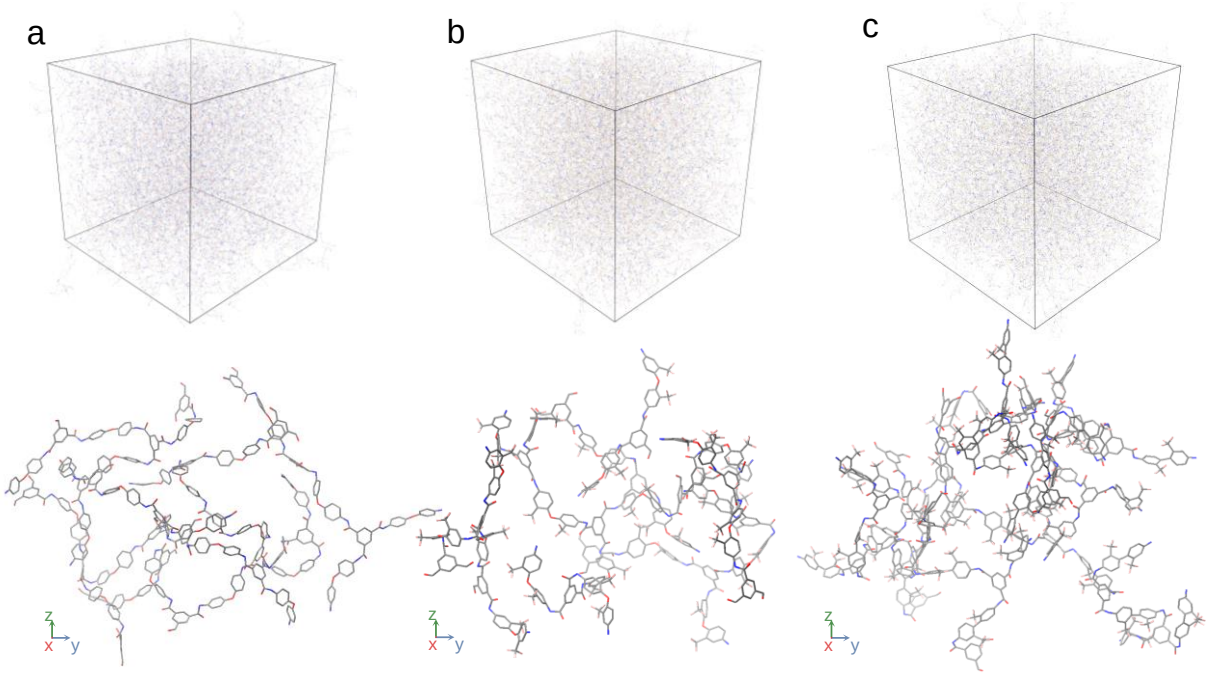


**Supplementary Fig. 3. Microporous structure characterization of polyamide polymers.** Energy minimization model (top) and 3D spatial structure (bottom) of polyamide constructed by molecular dynamics (MD) simulations. **a** ODA-M, **b** 6FODA-M, and **c** PFMB-M. Atoms color code: C, gray; O, red; N, blue; F, pink.

**Supplementary Note 12:** Polyamide model polymers were constructed by simulating the polymerization of the diamine monomers with TMC using MD simulations to access the microporous structure of the polyamide nanofilm. The results reveal that the polyamide fragments extracted from the 6FODA-M and ODA-M model polyamide networks exhibit relatively low chain packing densities compared to PFMB-M polyamide. This can be attributed to the rotational freedom of the benzene rings around flexible ether linkages in the 6FODA and ODA monomers, resulting in a larger torsional space within the polymer network. This structural flexibility promotes the formation of twisted non-coplanar conformations, thereby increasing the intrinsic microporosity of the resulting polyamide polymer.

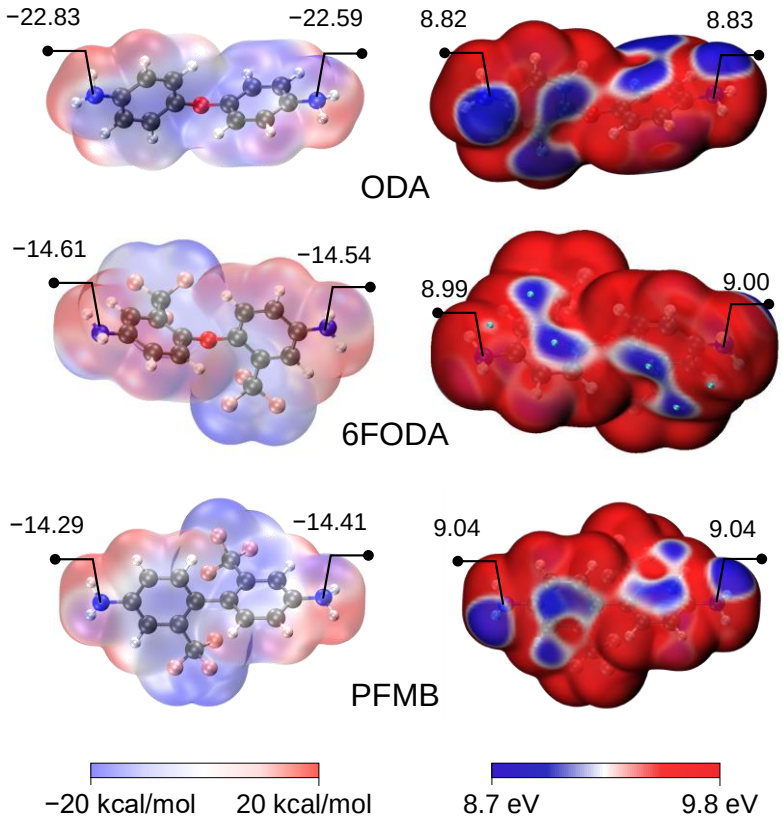


**Supplementary Fig. 4. Electronic structure characterization of diamine monomers using DFT calculations.** Molecular structures and visualization of their electrostatic potentials (ESP, left) and distributions of the average local ionization energy (ALIE, right). Atoms color code: C, gray; H, white; O, red; N, blue; F, pink.

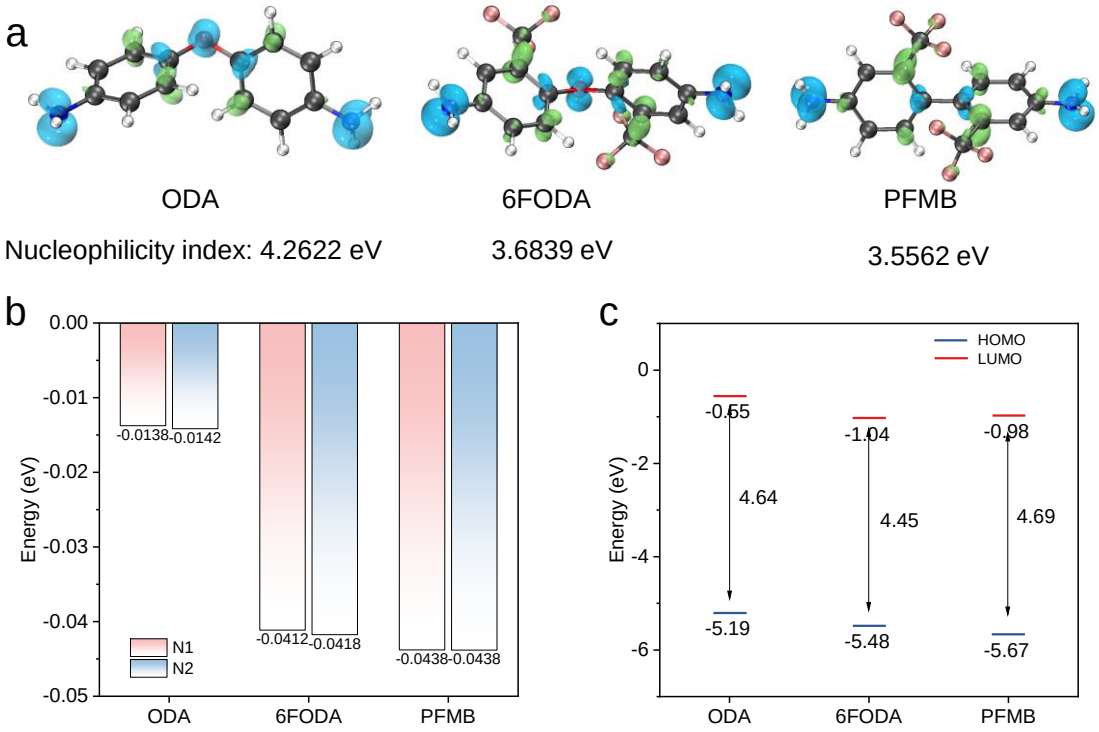


**Supplementary Fig. 5. Electronic structure characterization of diamine monomers using DFT calculations. a** Fukui function and nucleophilicity index. Atoms color code: C, gray; H, white; O, red; N, blue; F, pink. **b** Local electron attachment energy (LEAE) at the amino (N) sites. **c** Highest occupied molecular orbital (HOMO) and lowest unoccupied molecular orbital (LUMO) energy levels.

**Supplementary Note 13:** To evaluate the intrinsic reactivity of the diamine monomers to TMC, density functional theory (DFT) was used to calculate multiple electronic descriptors, including electrostatic potential (ESP), average local ionization energy (ALIE), Fukui functions, local electron attachment energy (LEAE), and frontier orbital energies (HOMO/LUMO). ESP and ALIE maps show that the overall nucleophilic reactivity follows the order of ODA > 6FODA > PFMB. The ALIE values of the amine nitrogen atoms reflect the local ionization potential and serve as the main indicator of nucleophilic reactivity, while ESP represents electrostatic interactions and the spatial accessibility of the reactive sites. The Fukui functions, LEAE, and HOMO energy levels

further confirm this trend, collectively indicating that ODA has the highest nucleophilic activity, followed by 6FODA, whereas PFMB exhibits the weakest reactivity. The corresponding nucleophilicity indices are 4.26 eV (ODA), 3.68 eV (6FODA), and 3.56 eV (PFMB), respectively. Overall, the multi-descriptor DFT analysis provides a consistent and quantitative understanding of the relative reactivity order ODA > 6FODA > PFMB, which is consistent with the observed differences in polyamide formation kinetics.

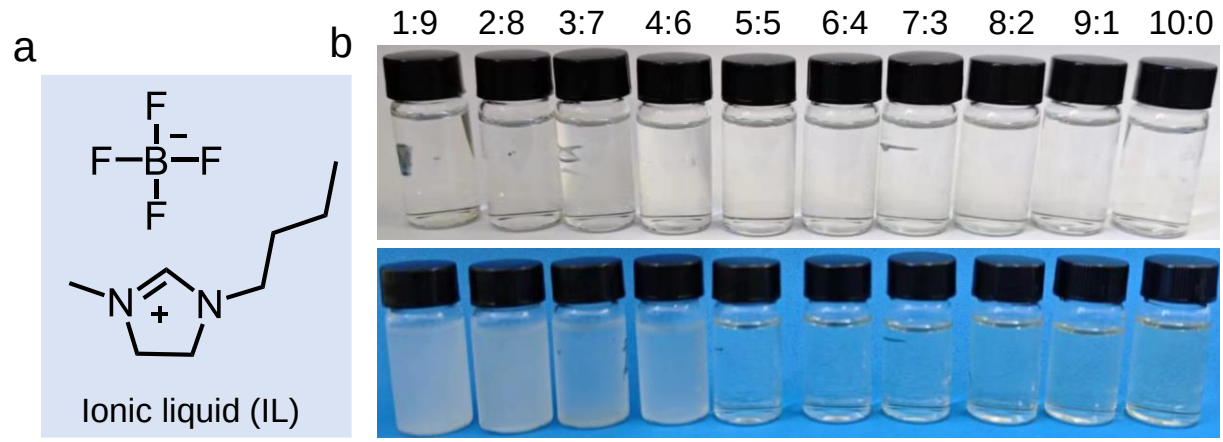


**Supplementary Fig. 6. Ionic liquid enables the dissolution of diamine monomers in water for interfacial polymerization. a** Molecular structure of the $[C_4mim]BF_4$ ionic liquid (IL). **b** Digital photos depicting the dissolution state of 1.0 wt/v% 6FODA in a mixture of IL and water with various IL/water volume ratios (e.g., 1:9, 2:8, 3:7, 4:6, 5:5, 6:4, 7:3, 8:2, 9:1, and 10:0). The upper and lower photos show the pure solvents and the dissolved state of 1.0 wt/v% 6FODA in the corresponding solvent, respectively.

**Supplementary Note 14:** A certain amount of 6FODA was dissolved in a mixture of IL and water at different IL/water volume ratios, with a target concentration of 1.0 wt/v% in the solvent. The resulting mixture was sonicated for 30 min and then left to stand for some time to observe the state of the solution. The upper photos show that $[C_4mim]BF_4$ IL is highly miscible with water at any volume ratio. 6FODA monomer is almost insoluble in water, while IL is an excellent solvent. As demonstrated by the lower photos, 6FODA gradually dissolves in the binary mixed solvent as the content of IL increases. A transparent 6FODA solution was obtained when the IL/water volume ratio reached 1:1. Therefore, a mixture of IL and water with a volume ratio of 1:1 was used as the aqueous solvent for the diamine monomers.

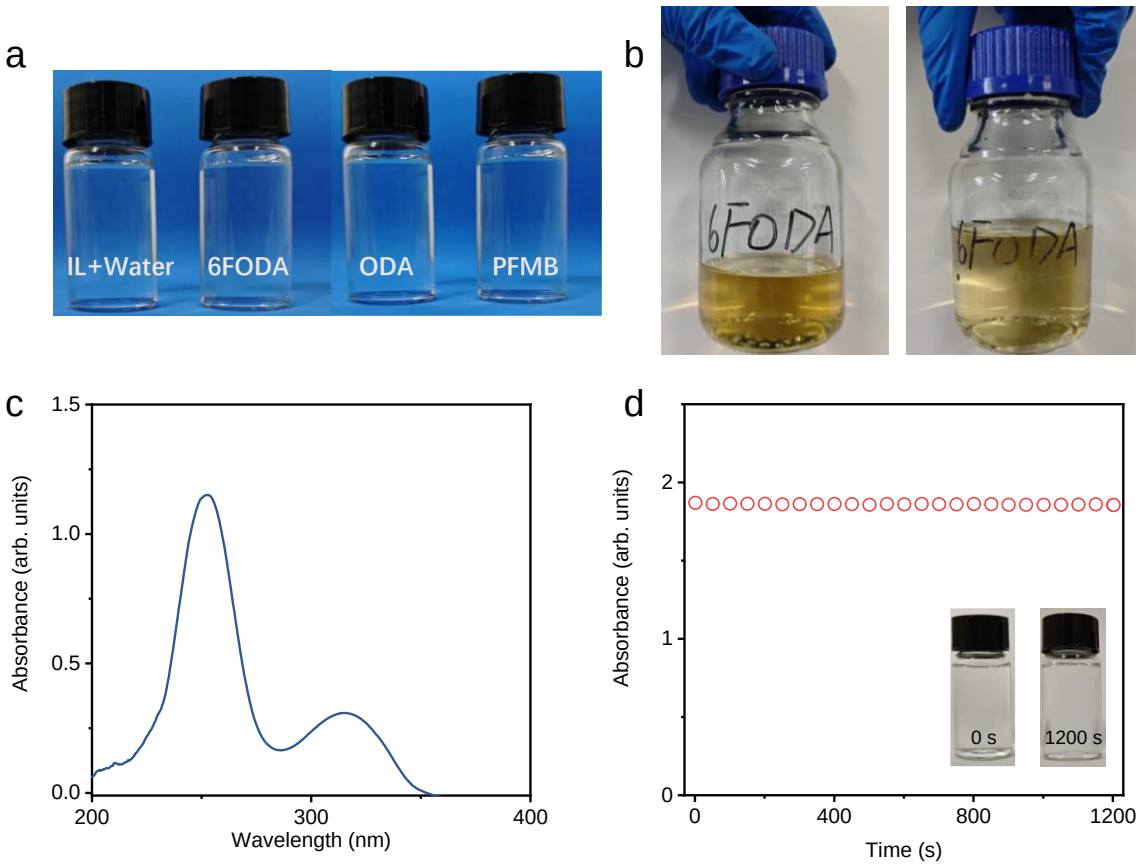


**Supplementary Fig. 7. Solubility examination of the diamine monomers in a binary mixed solvent of IL and water. a** Digital photos of the IL/water mixture with a volume ratio of 1:1 and its solutions containing 1.0 wt/v% 6FODA, ODA, and PFMB, respectively. **b** Photographs of the 6FODA solutions in pure IL and IL/water (1:1, v/v) mixture. **c** UV-vis spectrum of the 6FODA solution in a mixture of IL/water (1:1, v/v). **d** UV-vis absorbance curves of the diluted IL/water solutions of 6FODA at $\lambda$ = 255 nm over 1200 s. The inset shows the photographs of the corresponding solutions.

**Supplementary Note 15:** The 6FODA, ODA, and PFMB diamine monomers exhibit high solubility in the IL/water (1:1, v/v) solvent. Photographs and UV-vis spectroscopy data show that the resulting 6FODA solution remained stable during a long-term absorbance test of 1200 s, indicating that the amine monomer was completely dissolved in the solvent and the obtained solution was stable.

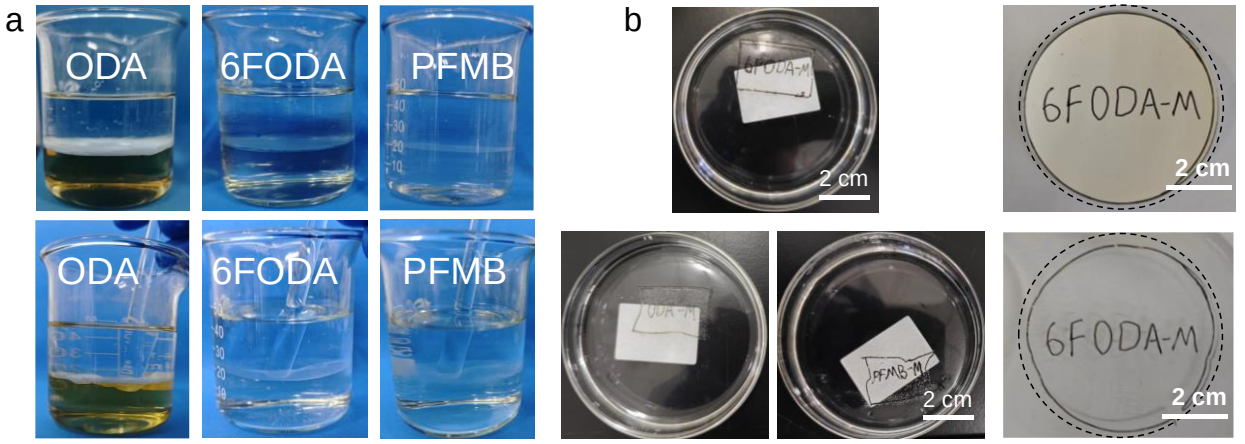


**Supplementary Fig. 8. Visualization of polyamide nanofilms prepared by interfacial polymerization. a** Photographs showing the formation of polyamide nanofilms at the interface of aqueous and hexane phase solutions after interfacial polymerization (IP) of a diamine with TMC in the beaker (top) and the perturbation of the formed polyamide nanofilms with a glass rod (bottom). **b** Photos of polyamide TFC membranes prepared by in situ IP on PAN substrate when the polyamide nanofilms were detached in DMF solution (the polyamide films floating on the solution surface). The three polyamide TFC membranes were prepared with the same concentration of diamine monomer (1.0 wt/v%) and TMC (0.1 wt/v%). The IP reaction time for 6FODA-M and ODA-M was 2 min, while that for PFMB-M was 20 min.

**Supplementary Note 16:** ODA, 6FODA, and PFMB diamine monomers dissolved in the aqueous solution can react quickly with TMC in hexane at the interface to form robust and flexible polyamide nanofilms. In addition, polyamide TFC membranes can also be prepared by in-situ interfacial polymerization on the PAN substrates. Free-standing polyamide nanofilms that float on the solution surface can be obtained by dissolving the PAN substrate using DMF.

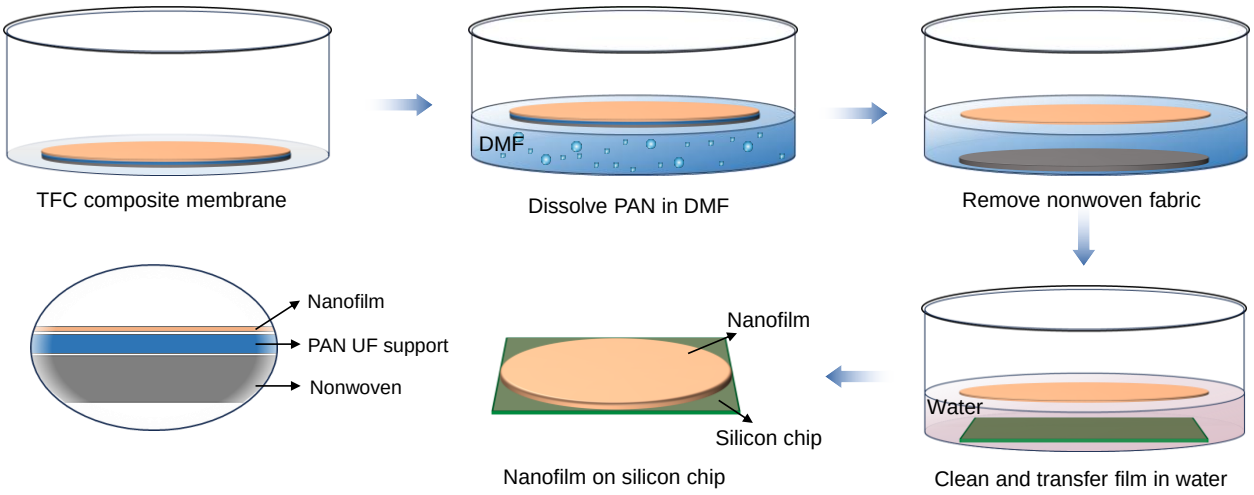


**Supplementary Fig. 9. Exfoliation and transfer of free-standing polyamide nanofilm formed in situ on a PAN substrate.** Schematic diagram of the process for exfoliating the polyamide layer of the polyamide TFC membrane by dissolving the PAN substrate using DMF to obtain a free-standing polyamide nanofilm, which can be subsequently transferred onto a silicon chip.

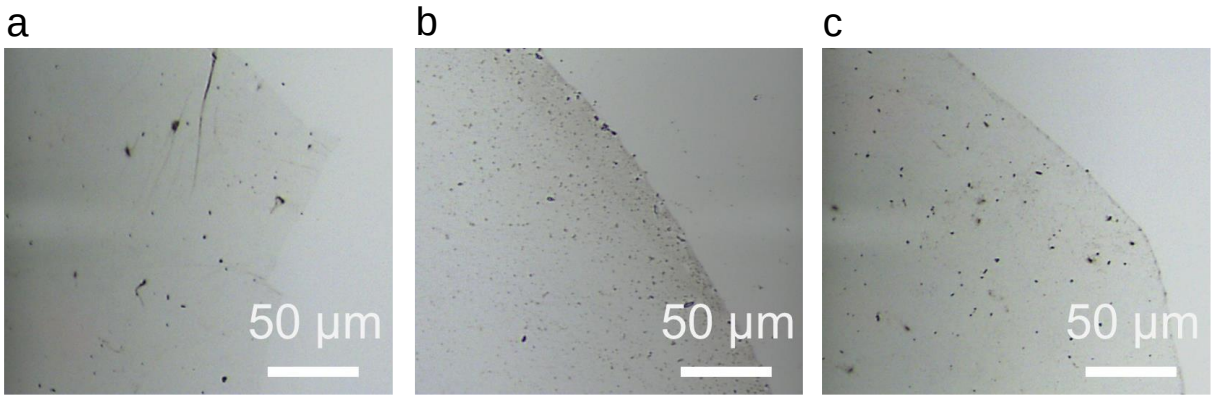


**Supplementary Fig. 10. Optical microscope images of free-standing polyamide nanofilm on a silicon wafer. a** ODA-M, **b** 6FODA-M, and **c** PFMB-M. The three polyamide TFC membranes were prepared with the same concentration of diamine monomer (1.0 wt/v%) and TMC (0.1 wt/v%). The IP reaction time for 6FODA-M and ODA-M was 2 min, while that for PFMB-M was 20 min.

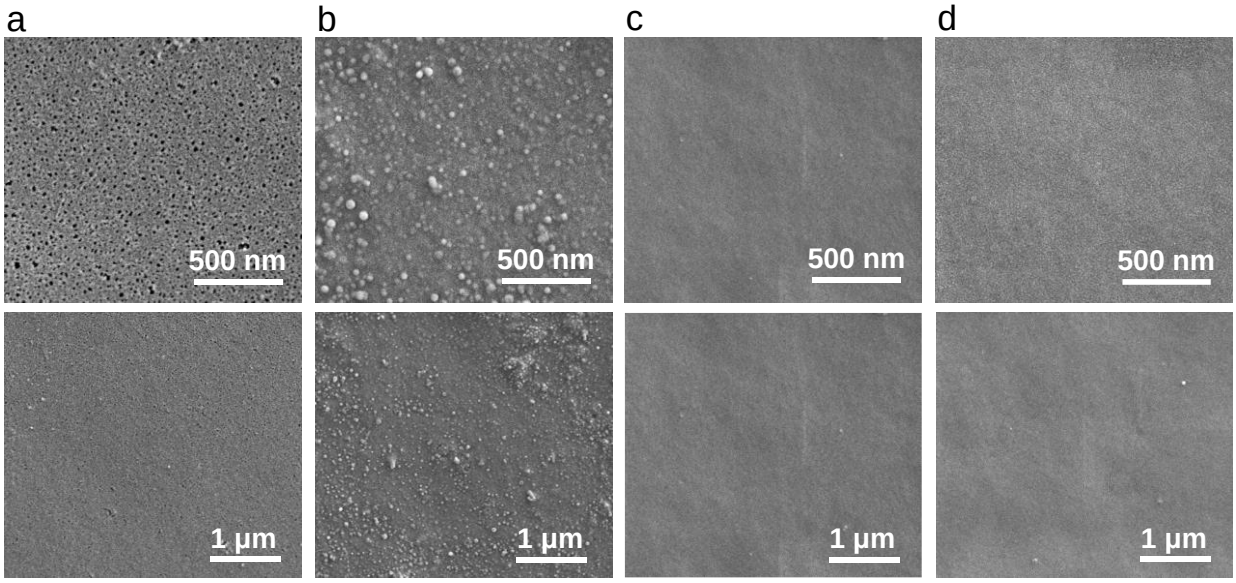


**Supplementary Fig. 11. a–d Membrane surface morphology observation.** Surface SEM images of (**a**) PAN substrate, (**b**) ODA-M, (**c**) 6FODA-M, and (**d**) PFMB-M polyamide TFC membranes. The three polyamide TFC membranes were prepared with the same concentration of diamine monomer (1.0 wt/v%) and TMC (0.1 wt/v%). The IP reaction time for 6FODA-M and ODA-M was 2 min, while that for PFMB-M was 20 min.

**Supplementary Note 17:** Surface SEM images show that the top surface of the PAN substrate is uniformly distributed with macropores. After the in-situ IP, the macropores are covered by a dense and continuous thin layer, indicating the successful formation of a polyamide nanofilm on top. Different from the smooth and flat surfaces of the polyamide nanofilms of PFMB-M and 6FODA-M membranes, the surface of ODA-M polyamide exhibits a nodular structure, which is probably due to the stronger reactivity of ODA monomer with TMC.

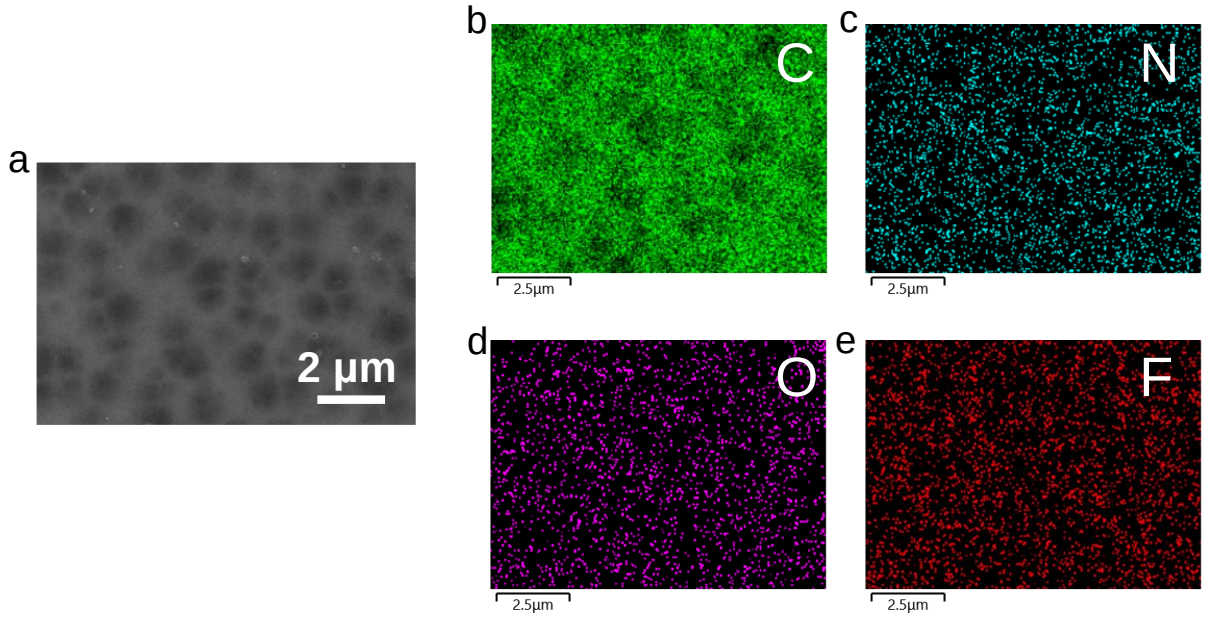


**Supplementary Fig. 12. SEM-EDS elemental mapping of the 6FODA-M membrane surface.** **a**, SEM morphology of the mapping region. **b–e** Elemental distribution diagram of (**b**) carbon (C, green), (**c**) nitrogen (N, blue), (**d**) oxygen (O, violet), and (**e**) fluorine (F, red) on the surface.

**Supplementary Note 18:** Taking 6FODA-M as an example, the SEM-EDS surface elemental scanning results show that C, N, O, and F elements are uniformly distributed on its surface, demonstrating that a continuous and uniform polyamide layer was formed on top of the PAN substrate during interfacial polymerization.

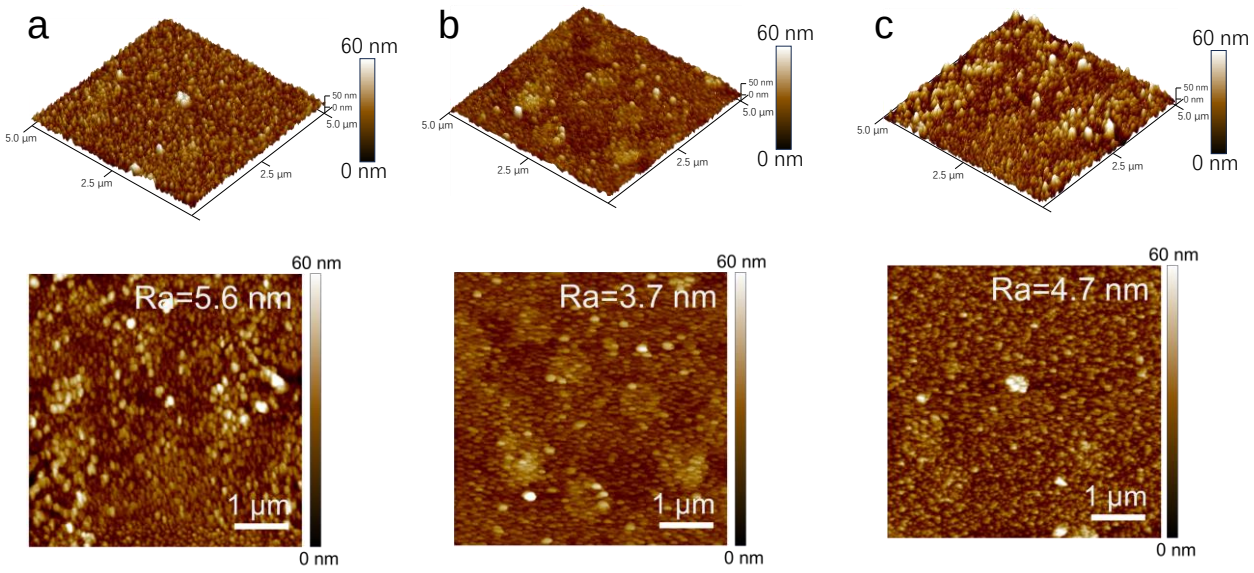


**Supplementary Fig. 13. Surface topology observation of the polyamide TFC membranes based on AFM.** 3D (top) and 2D (bottom) AFM surface images of **a** ODA-M, **b** 6FODA-M, and **c** PFMB-M TFC membranes with the calculated surface roughness. The three polyamide TFC membranes were prepared with the same concentration of diamine monomer (1.0 wt/v%) and TMC (0.1 wt/v%). The IP reaction time for 6FODA-M and ODA-M was 2 min, while that for PFMB-M was 20 min.

**Supplementary Note 19:** AFM images reveal that all three polyamide TFC membranes possess smooth surfaces with extremely low roughness (Ra < 6 nm). The low surface roughness of polyamide films is generally associated with the retarded diffusion of the diamine monomers in aqueous solution toward the interface and their relatively low reactivity with TMC during IP. The surface roughness values of the polyamide TFC membranes follow the order of ODA-M > PFMB-M > 6FODA-M, which coincides with the difference in reactivity of the diamine monomers.

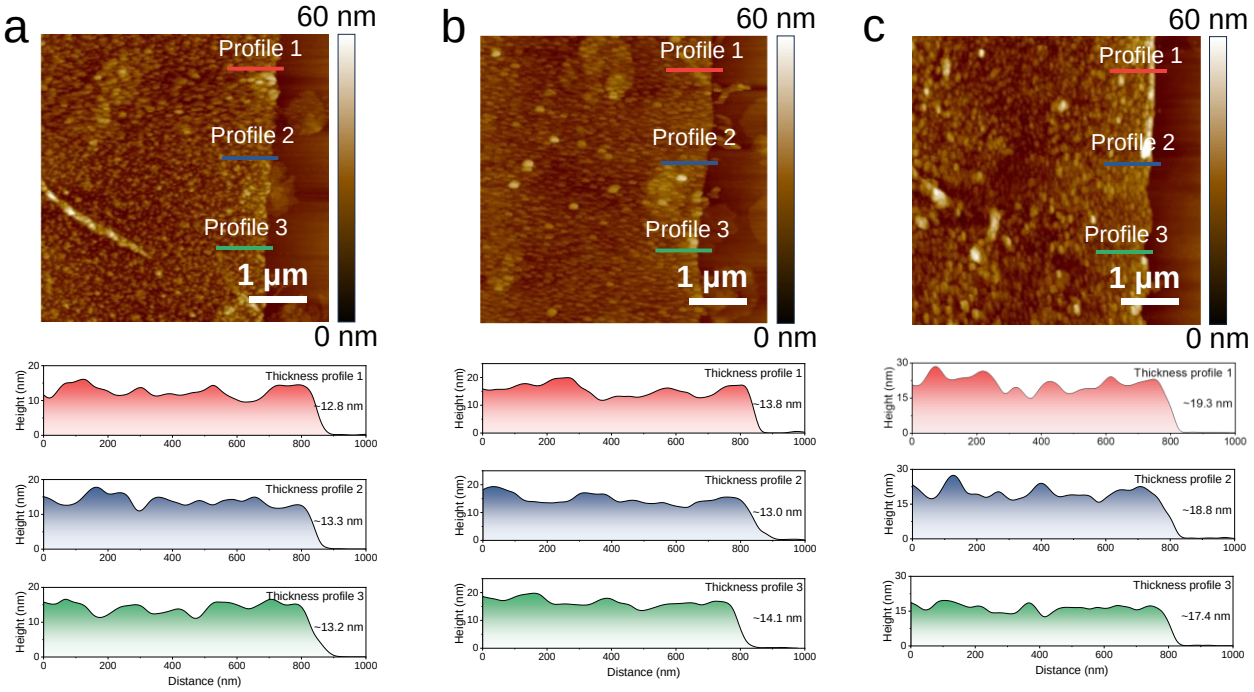


**Supplementary Fig. 14. Thickness characterization of free-standing polyamide nanofilms based on AFM.** AFM images of the **a** ODA-M, **b** 6FODA-M, and **c** PFMB-M polyamide nanofilms deposited onto a silicon wafer and the corresponding height profiles. The three polyamide TFC membranes were prepared with the same concentration of diamine monomer (1.0 wt/v%) and TMC (0.1 wt/v%). The IP reaction time for 6FODA-M and ODA-M was 2 min, while that for PFMB-M was 20 min.

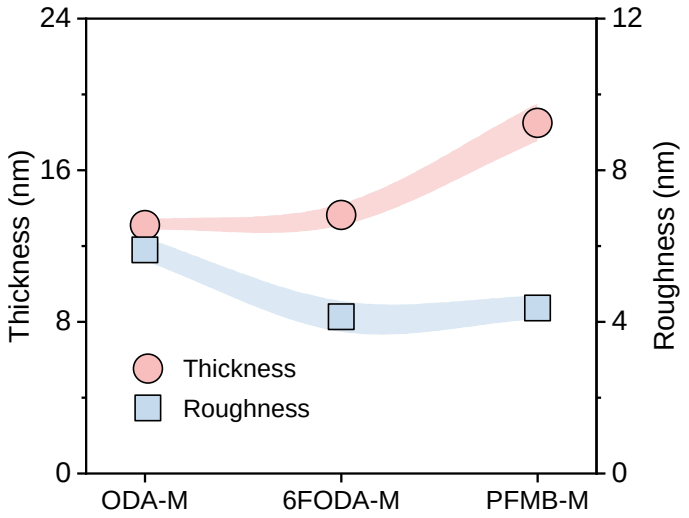


**Supplementary Fig. 15. Summary of the thickness and surface roughness of free-standing polyamide nanofilms of ODA-M, 6FODA-M, and PFMB-M membranes.** Error bars represent the standard deviation obtained from three independent measurements.

**Supplementary Note 20:** The AFM thickness and roughness test results reveal that the three free-standing polyamide nanofilms have an ultrathin thickness of less than 20 nm and ultra-low roughnesses of less than 6 nm. In general, the thin thickness of polyamide prepared by interfacial polymerization is mainly attributed to the slow diffusion rate and low reactivity of amine monomers. DFT calculations confirm that the molecular sizes of the three diamine monomers (e.g., ODA, 6FODA, and PFMB) are relatively larger and their reactivity with TMC is relatively lower than those of traditional diamine monomers such as piperazine (PIP) and m-phenylene diamine (MPD) that are widely used in the preparation of state-of-the-art desalination polyamide membranes. Furthermore, the IL component in the aqueous solution of the diamine monomers further slows down their diffusion toward the interface by increasing the solution viscosity[19]. Collectively, ultra-thin and smooth polyamide nanofilms were achieved by the diamines.

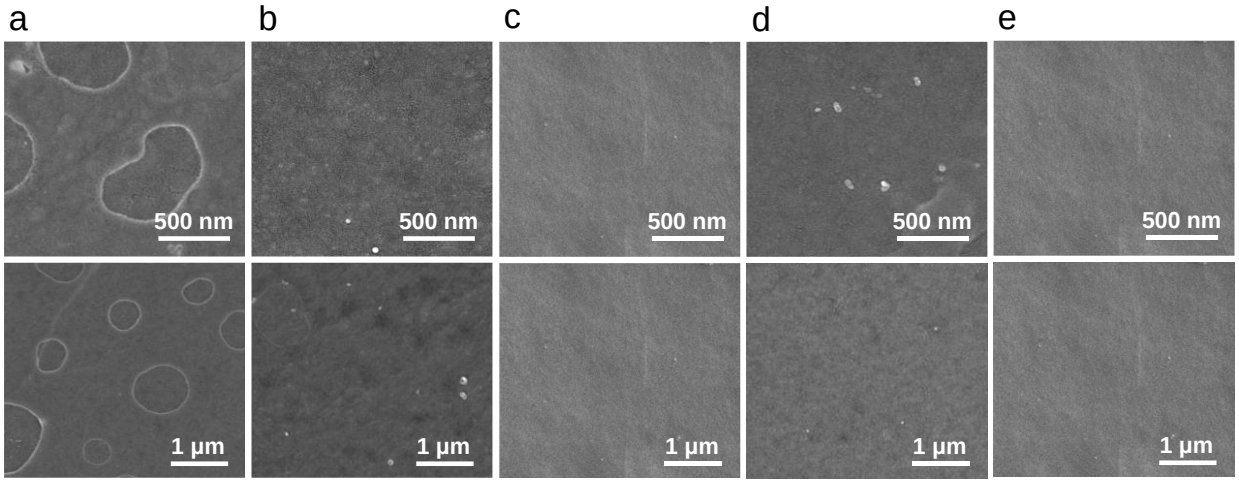


**Supplementary Fig. 16. Surface morphology inspection of 6FODA-M TFC membranes prepared with different IP reaction times.** SEM surface images of the 6FODA-M membranes prepared with an IP reaction time of **a** 15 s, **b** 30 s, **c** 120 s, **d** 300 s, and **e** 600 s. All polyamide TFC membranes were prepared with the same concentration of 6FODA (1.0 wt/v%) and TMC (0.1 wt/v%).

**Supplementary Note 21:** It was observed from the SEM images that the porous surface of the PAN substrate was gradually covered by the polyamide layer as the IP reaction time increased. In the short IP reaction time of 15 s, although most of the macropores on the substrate surface were covered, a large number of uncovered areas could still be observed, indicating that the reaction time of 15 s was not sufficient to form a contiguous polyamide layer on the substrate. As the polymerization time was extended to 30 s, the unclosed surface defective portions gradually closed, signifying the formation of a continuous polyamide layer. However, the macropores and rough features unique to the PAN substrate can still be seen in the SEM images, suggesting that the formed polyamide layer is still loose. When the reaction time was further prolonged to 120 s, the surface of the PAN substrate became completely smooth and flat, confirming that a dense and defect-free polyamide nanofilm was formed at this reaction time or longer.

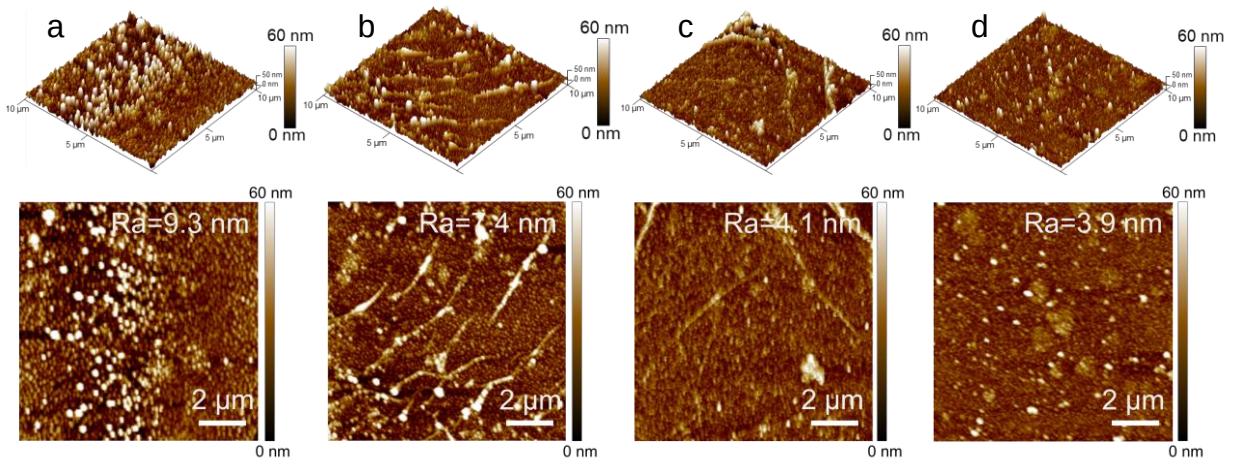


**Supplementary Fig. 17. Surface topology characterization of the 6FODA-M TFC membranes prepared with different IP reaction times.** 3D (top) and 2D (bottom) AFM surface images and the calculated surface roughness of the 6FODA-M membranes prepared with an IP reaction time of **a** 15 s, **b** 30 s, **c** 300 s, and **d** 600 s. All polyamide TFC membranes were prepared with the same concentration of 6FODA (1.0 wt/v%) and TMC (0.1 wt/v%).

**Supplementary Note 22:** AFM images show that the 6FODA-M membranes present very smooth surfaces with a surface roughness (Ra) of less than 10 nm. When the reaction time was extended from 15 to 600 s, Ra gradually decreased from 9.3 to 3.9 nm. The relatively rough surface of the 6FODA-M membrane prepared at a short IP reaction time (i.e., 15 s) can be attributed to the discontinuity of the polyamide layer and the partial exposure of the PAN substrate surface, which is consistent with the SEM characterization results.

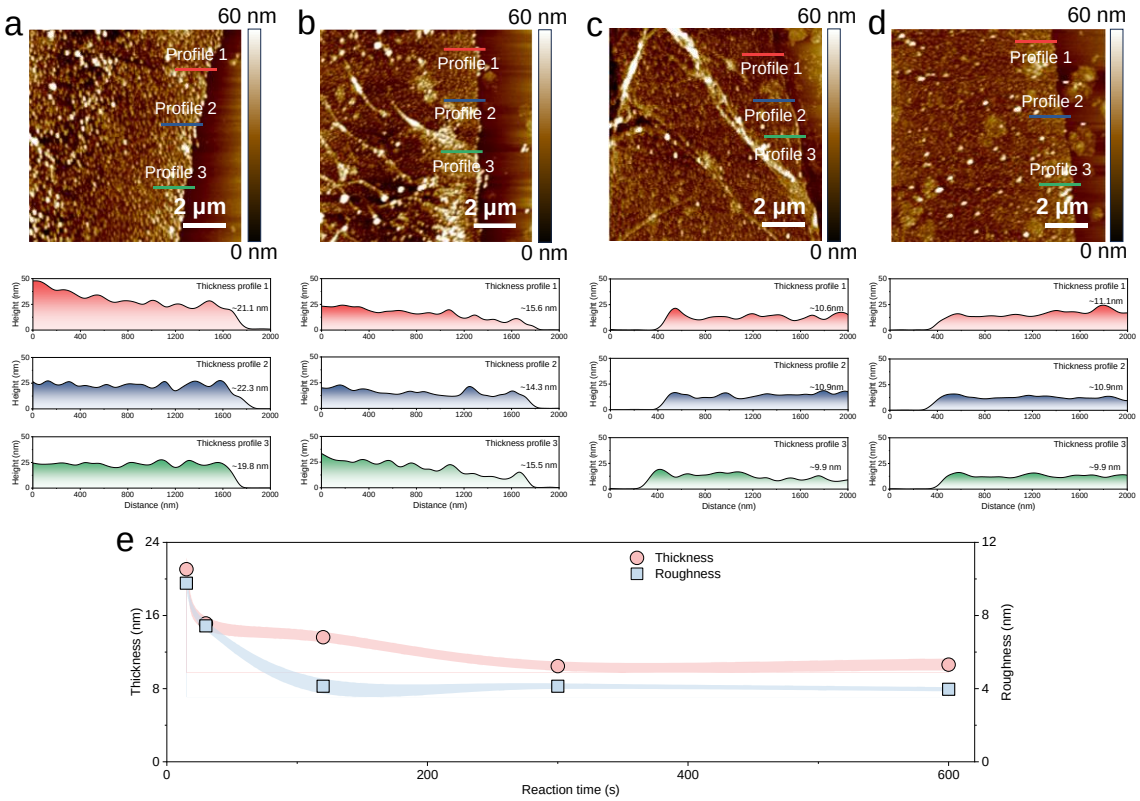


**Supplementary Fig. 18. Thickness and roughness characterization of the free-standing polyamide nanofilms of 6FODA-M TFC membranes prepared with different IP reaction times.** AFM surface images and corresponding height profiles of the polyamide nanofilms of 6FODA-M membrane prepared with an IP reaction time of **a** 15 s, **b** 30 s, **c** 300 s, and **d** 600 s. **e** Summary of the thickness and surface roughness of the polyamide nanofilms. All polyamide TFC membranes were prepared with the same concentration of 6FODA (1.0 wt/v%) and TMC (0.1 wt/v%). Error bars represent the standard deviation obtained from three independent measurements.

**Supplementary Note 23:** AFM thickness test results show that all the free-standing polyamide nanofilms have an ultrathin thickness of less than 20 nm. Surprisingly, as the IP reaction time increases from 15 to 600 s, the thickness of the polyamide nanofilm gradually decreases from about 21.1 to 10.6 nm, which is contrary to the acquiescent phenomenon that the thickness of the polyamide film increases with the reaction time in the traditional IP process. We speculate that this

may be related to the relatively larger molecular size and lower reactivity of 6FODA diamine relative to other reported monomers. Specifically, a rough, loose nascent polyamide layer was rapidly formed in the initial stage of the IP reaction, which suppresses the trans-film diffusion of 6FODA to further react with TMC due to its large molecular size. In addition, the incompletely reacted 6FODA molecules in the nascent polyamide layer further crosslinked with TMC as the reaction time increased, which densified the film and thus further retarded the growth of the polyamide layer. As a result, the thickness of the 6FODA polyamide nanofilms no longer increases with the extension of the IP reaction time. With the extension of IP reaction time, the surface morphology of the 6FODA-M polyamide membrane alters from loose and rough to dense and smooth, during which the thickness and surface roughness of the polyamide layer gradually decrease.

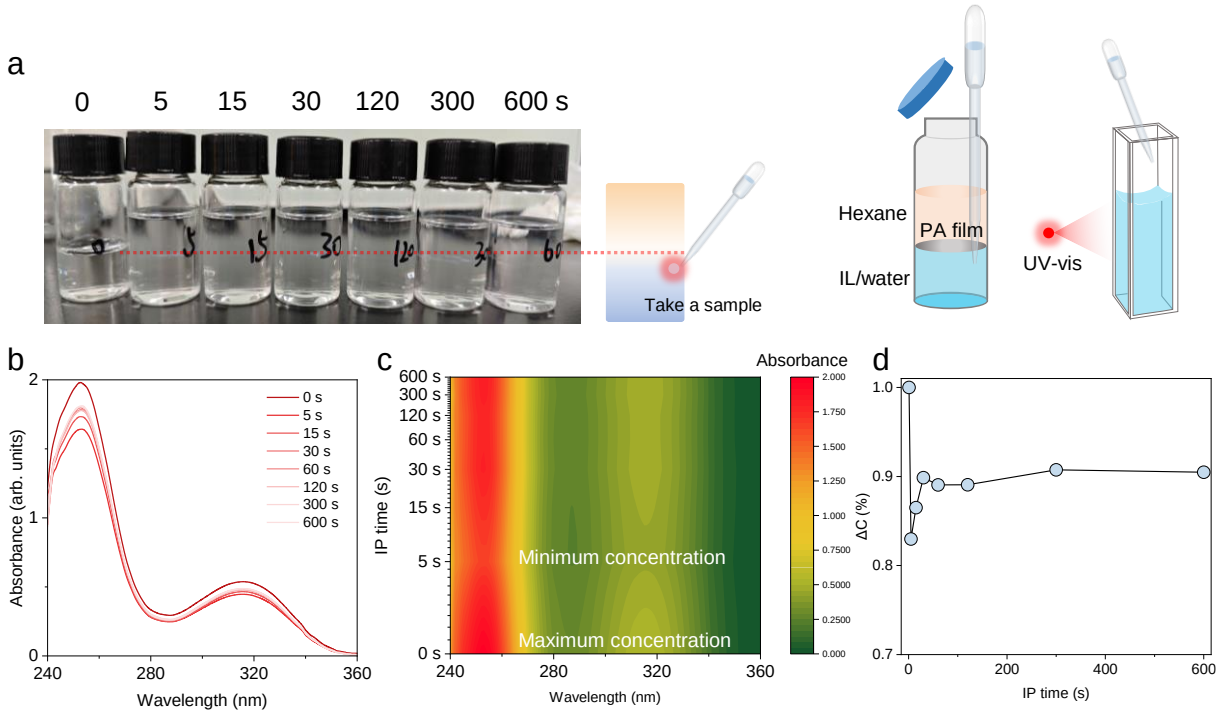


**Supplementary Fig. 19. Monitoring of diamine monomer consumption during the interfacial polymerization of 6FODA-M membrane. a** Digital photographs of the reaction interface at different polymerization times. At each specified time point, the reaction was quenched and the aqueous phase near the interface was sampled for analysis. **b**, **c** UV–vis spectra of the remaining aqueous phase solution after different IP reaction times. **d** Concentration evolution of the residual 6FODA monomer in the aqueous phase as a function of polymerization time. The concentrations of 6FODA and TMC monomers in the IP reaction were 1.0 wt/v% and 0.1 wt/v%, respectively.

**Supplementary Note 24:** To directly verify the proposed diffusion-limiting behavior, we conducted monomer depletion experiments by monitoring the concentration of 6FODA in the aqueous phase during the IP process. Independent sample vial experiments were terminated at different reaction times (5–600 s), and the residual 6FODA concentration was determined by UV–vis spectroscopy. A sharp decrease of approximately 17% in monomer concentration was observed within the first 5 s, after which the concentration remained essentially constant, indicating that the

nascent PA layer effectively hindered further diffusion of the amine monomers. This provides clear evidence for the self-limiting IP behavior in the 6FODA system.

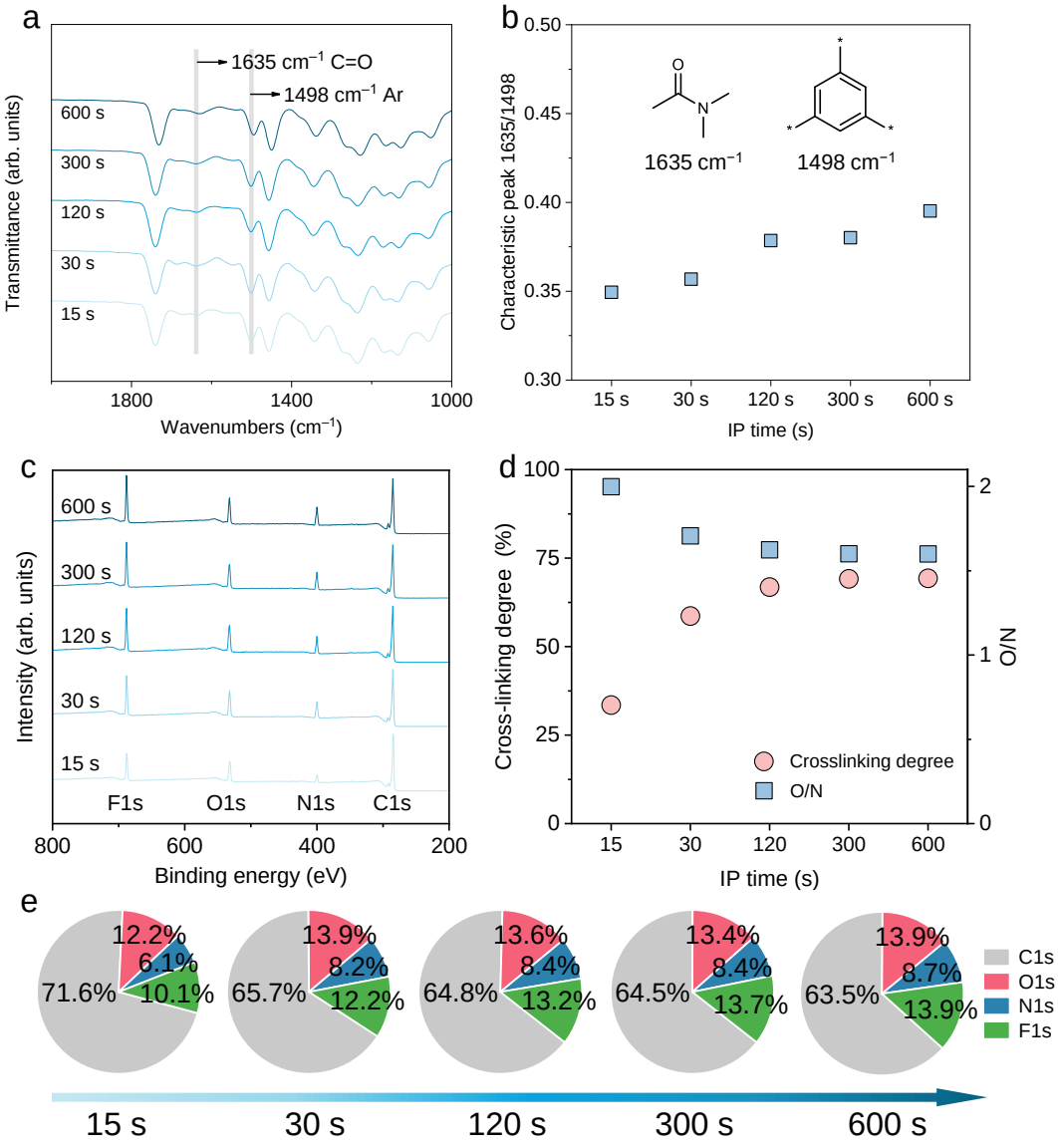


**Supplementary Fig. 20. Chemical structural characterization of 6FODA-M membranes prepared with different IP reaction times. a** FTIR spectra, **b** FTIR peak intensity ratio of amide bond/benzene ring (1635 $cm^{-1}$/1498 $cm^{-1}$). **c** XPS survey spectra, **d** corresponding elemental compositions, and **e** O/N atomic ratio and calculated crosslinking degree. The concentrations of 6FODA and TMC monomers in the IP reaction were 1.0 wt/v% and 0.1 wt/v%, respectively.

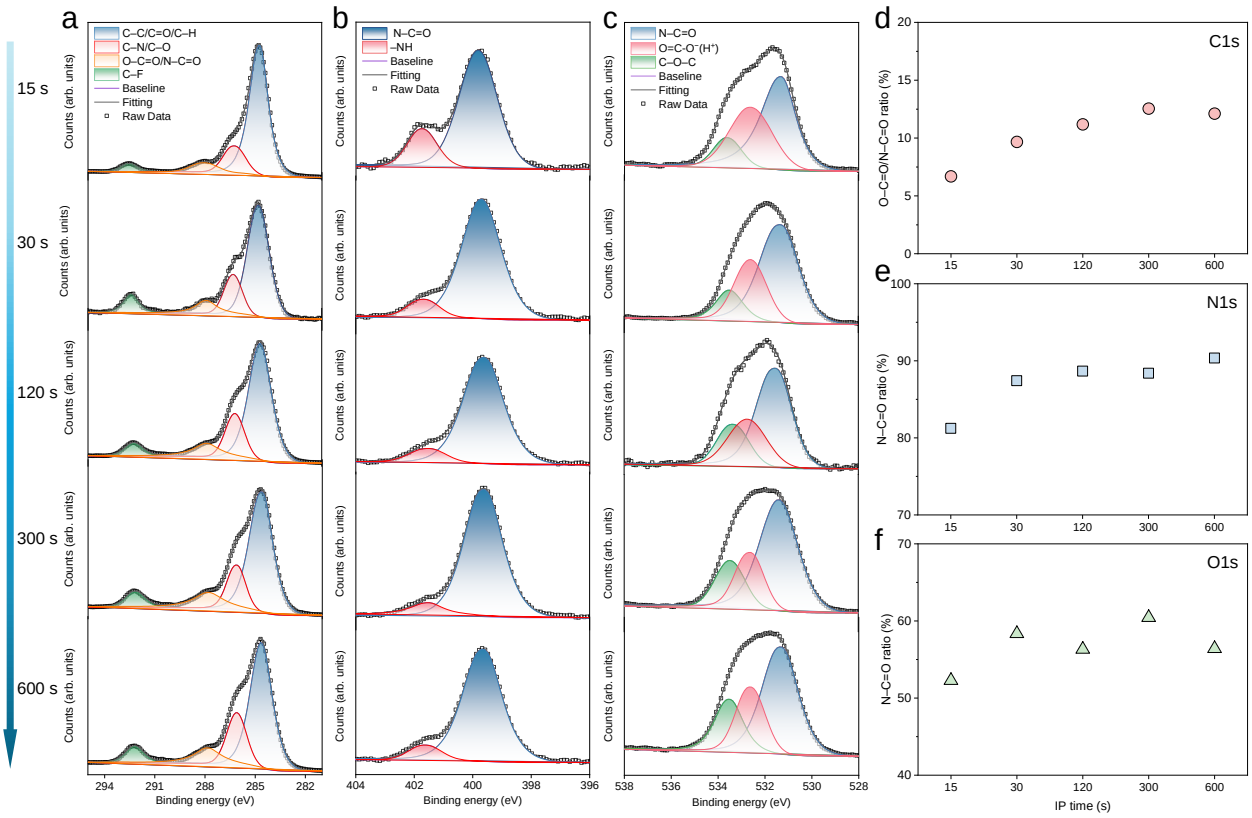


**Supplementary Fig. 21. Chemical structure analysis of 6FODA-M membranes prepared with different IP reaction times using XPS spectroscopy. a** C 1*s*, **b** N 1*s*, and **c** O 1*s* core-level spectra. **d** Fraction of O–C=O and N–C=O components in the C 1*s* spectrum. **e** Fraction of N–C=O component in the N 1*s* spectrum. **f** Fraction of N–C=O component in the O 1*s* spectrum. The concentrations of 6FODA and TMC monomers in the IP reaction were 1.0 wt/v% and 0.1 wt/v%, respectively.

**Supplementary Note 25:** To explain the unexpected decrease in polyamide film thickness with increasing interfacial polymerization (IP) time, we performed additional XPS and FTIR analyses. FTIR spectra show the characteristic C=O absorption peak of the amide bond at 1635 $cm^{-1}$ and the C–O (1230 $cm^{-1}$) and C–F (1125 $cm^{-1}$) absorption peaks of the 6FODA monomer, confirming the successful formation of polyamide via amination with TMC. XPS results reveal a gradual decrease in the O/N ratio with prolonging IP time, which signifies an increase in the crosslinking degree from ~33.5% at 15 s to ~66.8% at 120 s before stabilizing at ~69.3% after 600 s. High-resolution

C 1*s*, O 1*s*, and N 1*s* spectra consistently indicate an increase in the fraction of crosslinked N–C=O components, particularly in the N 1*s* region, where the crosslinking contribution increased from 81.3% (15 s) to 88.7% (120 s) and stabilized at 88.4–90.4% for 300–600 s. FTIR spectra also exhibit a gradual increase in the intensity ratio between the amide I band (1635 $cm^{-1}$) and the aromatic skeleton vibration (1495 $cm^{-1}$), which likewise plateaued at longer IP times. These results collectively indicate enhanced crosslinking and densification of the polyamide network, consistent with the observed thickness evolution.

In summary, the data in Supplementary Figs. 16–21 confirm the self-limiting growth mechanism of the 6FODA-M polyamide during the IP reaction. The initial polymerization of 6FODA with TMC generates a relatively loose nascent polyamide layer at the interface, and its formation is strongly influenced by the bulky $–CF_3$ substituents and contorted backbone of 6FODA. This steric hindrance restricts further diffusion of 6FODA monomers across the interface, while the residual amine and acyl chloride groups in the nascent polyamide layer undergo secondary condensation, leading to increased crosslinking density, enhanced compactness, and a slight decrease in apparent film thickness.

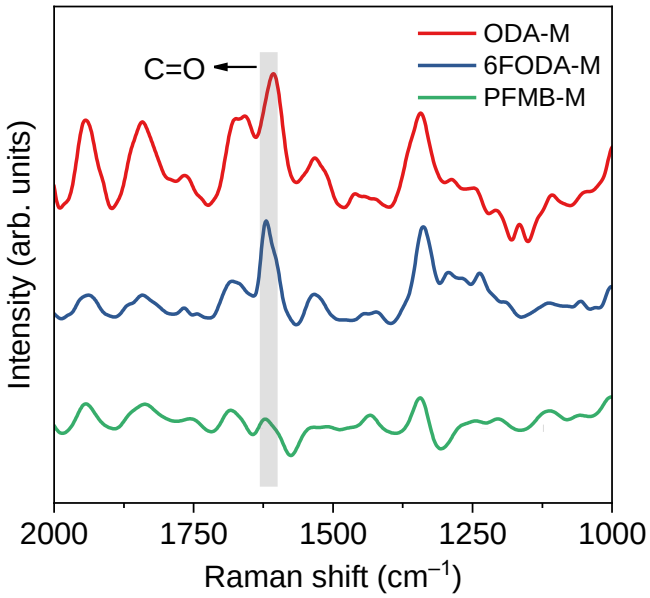


**Supplementary Fig. 22. Chemical structural characterization of the polyamide membranes using Raman spectroscopy.** Raman spectra of polyamide powders prepared by in situ IP of the three diamine monomers with TMC. The polyamides were prepared using the same concentration of diamine monomer (1.0 wt/v%) and TMC (0.1 wt/v%). The IP reaction time for 6FODA-M and ODA-M was 2 min, while that for PFMB-M was 20 min.

**Supplementary Note 26:** In line with the FTIR spectra of the polyamide membranes, the characteristic absorption peak at 1595 cm$^{-1}$ induced by the vibration of the amide bond was observed in the Raman spectra of three polyamide membranes, further verifying their chemical structure of aromatic polyamides. Among the three membranes, the C=O peak intensity of PFMB-M is relatively lower than that of ODA-M and 6FODA-M, which can be attributed to the relatively low crosslinking degree of polyamide caused by the weak reactivity of PFMB monomer with TMC.

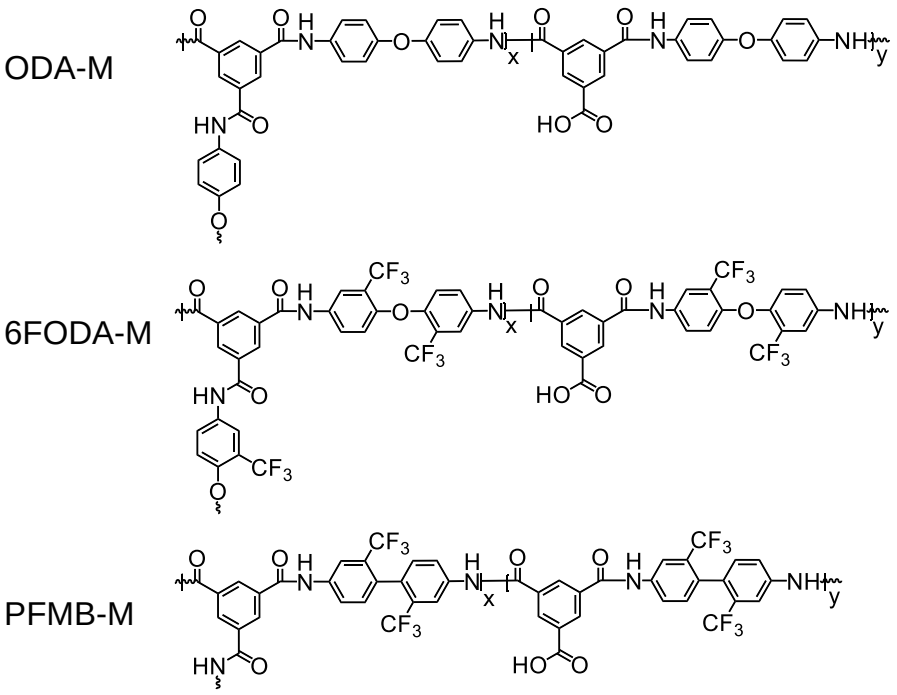


**Supplementary Fig. 23. Chemical structures of the three polyamide nanofilms.** Two extreme circumstances are considered in the IP reaction: Fully crosslinked (one diamine molecule reacts with three –COCl sites on TMC) and fully linear (one diamine molecule reacts with two –COCl sites on TMC) polyamide.

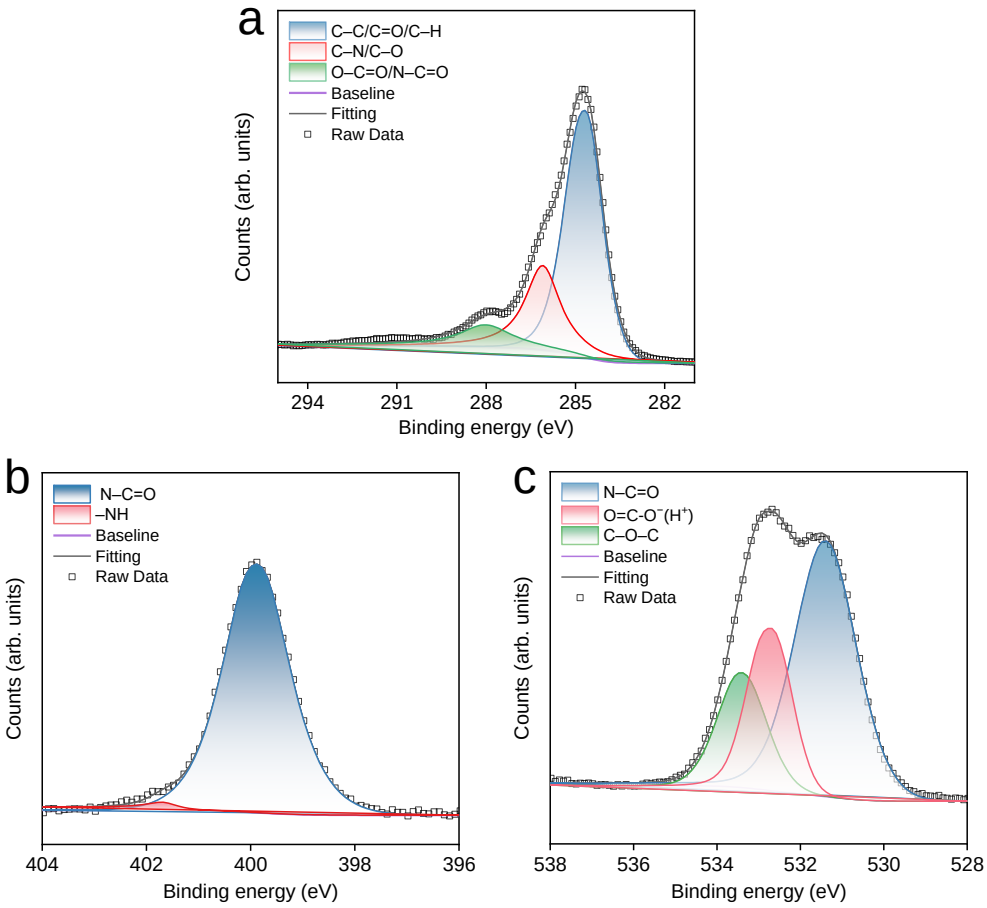


**Supplementary Fig. 24. Chemical structural characterization of ODA-M polyamide membrane using XPS spectroscopy.** High-resolution **a** C 1*s*, **b** N 1*s*, and **c** O 1*s* spectra. The concentrations of ODA and TMC monomers for the IP reaction were 1.0 wt/v% and 0.1 wt/v%, respectively. The IP reaction time was 2 min.

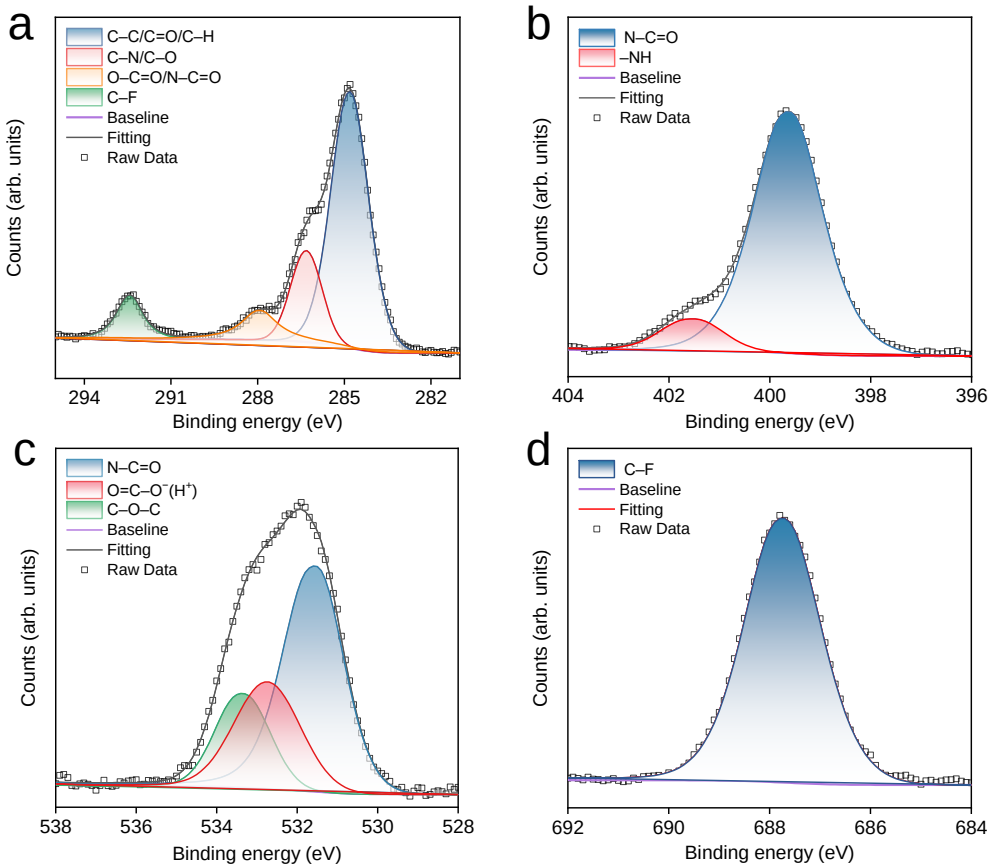


**Supplementary Fig. 25. Chemical structural characterization of 6FODA-M polyamide membrane using XPS spectroscopy.** High-resolution **a** C 1*s*, **b** N 1*s*, **c** O 1*s*, and **d** F 1*s* spectra. The concentrations of 6FODA and TMC monomers for the IP reaction were 1.0 wt/v% and 0.1 wt/v%, respectively. The IP reaction time was 2 min.

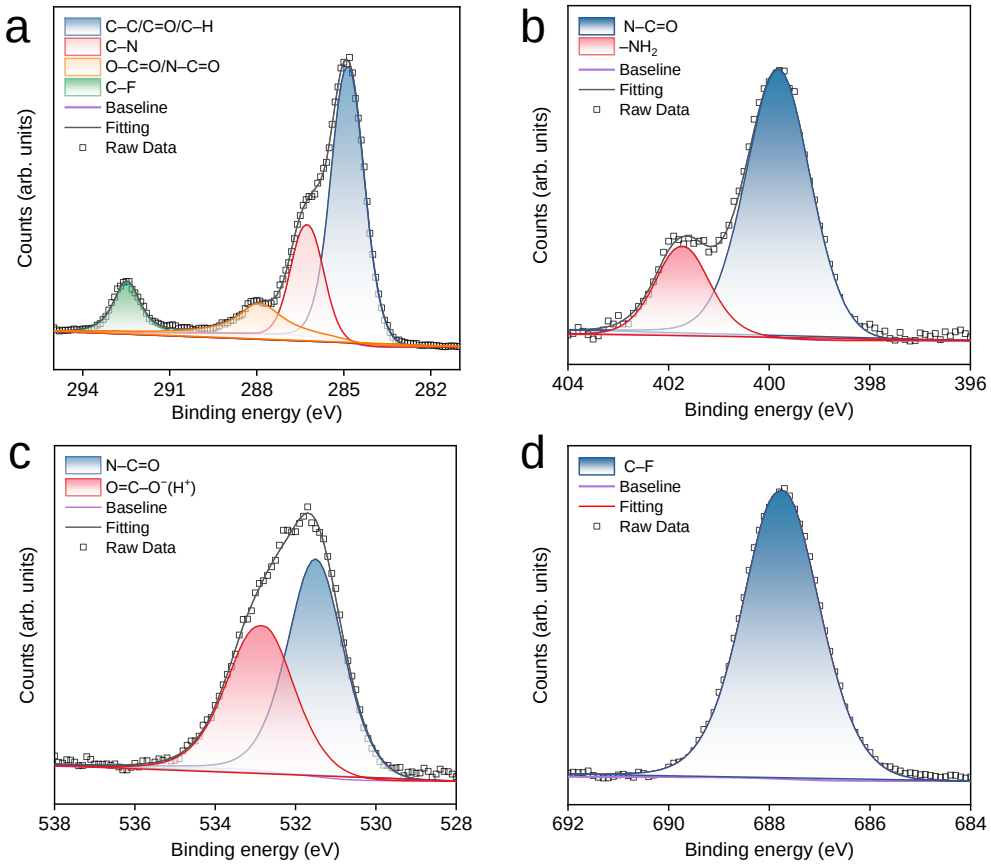


**Supplementary Fig. 26. Chemical structural characterization of PFMB-M polyamide membrane using XPS spectroscopy.** High-resolution **a** C 1*s*, **b** N 1*s*, **c** O 1*s*, and **d** F 1*s* spectra. The concentrations of PFMB and TMC monomers for the IP reaction were 1.0 wt/v% and 0.1 wt/v%, respectively. The IP reaction time was 20 min.

**Supplementary Note 27:** Since the PAN substrate contains only C and N, the appearance of O in the XPS spectrum of ODA-M and the presence of O and F in the spectra of 6FODA-M and PFMB-M confirm the formation of a polyamide layer through the polymerization of ODA, 6FODA, and PFMB diamine monomers with TMC, respectively. Notably, F was not detected on the surface of ODA-M, indicating that the IL in the aqueous monomer solution was not incorporated into the polyamide layer.

The C 1*s* XPS spectrum of ODA-M can be deconvoluted into three peaks corresponding to C–C/C=O/C–H, C–N/C–O, and O–C=O of carboxyl/N–C=O of amide, with binding energies of approximately 284.7, 286.1, and 288.0 eV, respectively. In addition to these three peaks, an additional deconvoluted peak at 292.4 eV attributed to the C–F bond was detected in the C 1*s* spectra of 6FODA-M and PFMB-M (Supplementary Table 2). Furthermore, 6FODA-M and PFMB-M show the F 1*s* peak at 687.8 eV, which is consistent with their fluorinated chemical structures. Two peaks at 399.8 and 401.7 eV were observed in the N 1*s* spectra of the three polyamide membranes, which are associated with the N–C=O amide bond and the unreacted $–NH_2$ on the diamine monomers, respectively. In accordance with the N 1*s* peaks, two deconvoluted peaks at 531.5 and 532.8 eV were detected in the O 1*s* spectrum of PFMB-M, which are attributed to the O=C–N amide bond and the hydrolyzed carboxyl groups ($O–C=O^{-}(H^{+})$), respectively. Besides these two peaks, a C–O–C peak at 533.5 eV appears in the O 1*s* spectra of ODA-M and 6FODA-M. In summary, the high-resolution XPS spectra confirm the formation of the polyamide nanofilms via the crosslinking reactions between the diamine monomers and TMC.

The crosslinking degree of the polyamide was obtained by analyzing the peak fitting results of the N 1*s* and O 1*s* spectra. According to the fitting results of the N 1*s* spectra, the proportion of unreacted amine groups ($–NH_2$) in PFMB-M is higher than that of ODA-M and 6FODA-M. The peak fitting results of O 1*s* spectra suggest that the percentage of $O–C=O^{-}(H^{+})$ generated by the hydrolysis of unreacted acyl chlorides in PFMB-M is higher, while the percentage of crosslinked amide linkages (O=C–N) is lower than those of the other two polyamide membranes. As a result, the magnitude of the O=C–N/$O–C=O^{-}(H^{+})$ ratios in the three polyamide membranes follows the trend of ODA-M > 6FODA-M > PFMB-M, implying that the ODA-M and 6FODA-M polyamides have higher crosslinking degrees than PFMB-M polyamide.

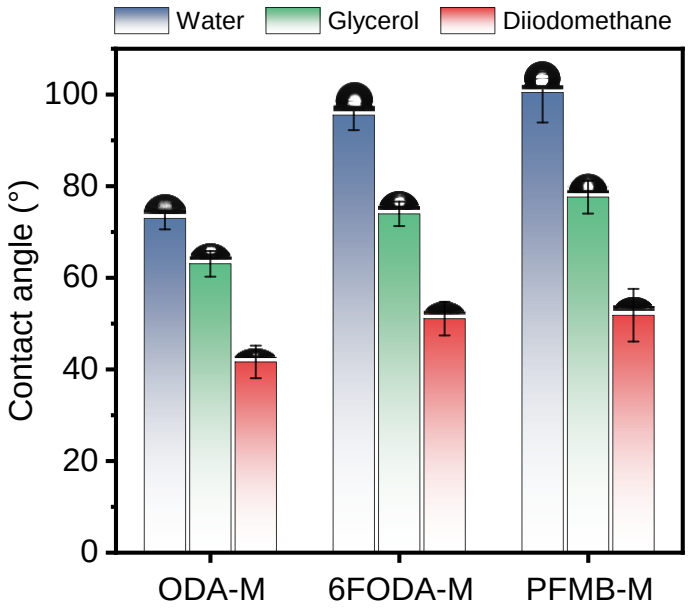


**Supplementary Fig. 27. Hydrophobicity analysis of polyamide membranes.** Surface contact angles with water, glycerol, and diiodomethane. Error bars represent the standard deviation obtained from three independent measurements.

**Supplementary Note 28:** The surface contact angles of three solvents were tested to evaluate the hydrophobicity of the polyamide TFC membranes. As shown in Supplementary Fig. 27 and Supplementary Table 3, the contact angles of 6FODA-M and PFMB-M for the three solvents are larger than those of ODA-M due to the fluorinated chemistry of the polyamide layer. Specifically, the water contact angle of the three polyamide TFC membranes follows the order of PFMB-M (100.4°) > 6FODA-M (95.5°) > ODA-M (72.9°). The slightly smaller water contact angle of 6FODA-M relative to PFMB-M is probably ascribed to the hydrophilic ether bonds in the polymer backbone of the former.

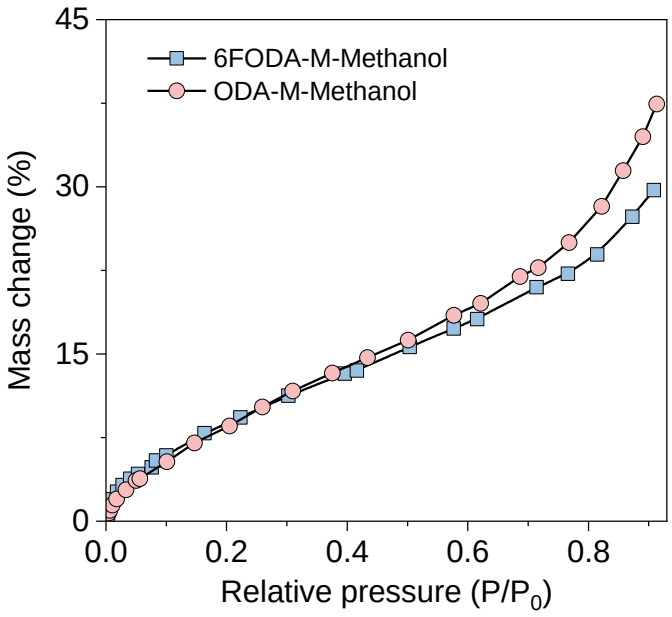


**Supplementary Fig. 28. Vapor sorption isotherms of ODA-M and 6FODA-M polyamide membrane in methanol (representative of polar solvents).**

**Supplementary Note 29:** To elucidate the effect of the $–CF_3$ substituents in 6FODA-M polyamide on solvent affinity, we conducted vapor sorption experiments on polar methanol and nonpolar hexane vapors using representative ODA-M and 6FODA-M membranes. As shown in Supplementary Fig. 28, the ODA-M membrane exhibits slightly higher methanol vapor uptake than the 6FODA-M membrane only at relatively high pressures, consistent with its stronger hydrophilicity.

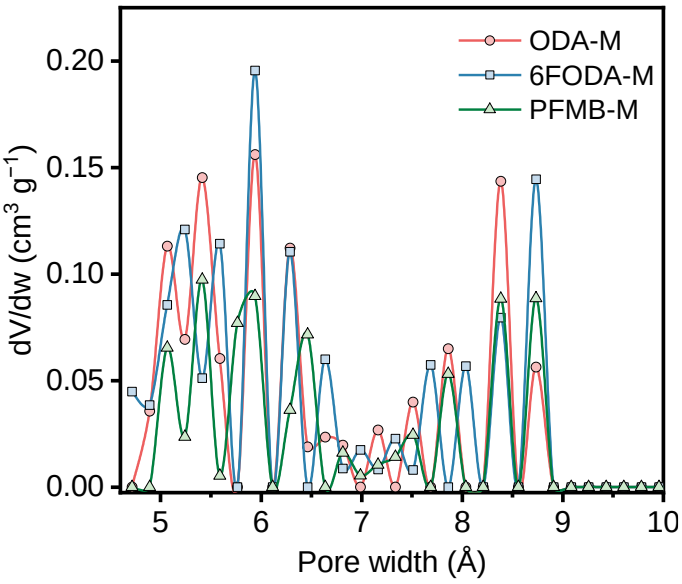


**Supplementary Fig. 29. Pore size analysis of polyamides based on $CO_2$ sorption isotherms.** Pore size distribution curves obtained from the nonlocal density functional theory (NLDFT).

**Supplementary Note 30:** Pore size analysis based on $CO_2$ sorption isotherms at 273 K shows that the pore sizes of the three polyamide membranes fall in the range of 5–9 Å in diameter. The subnanometer pores enable the polyamide membranes to exert precise molecular sieving in organic solvent filtration.

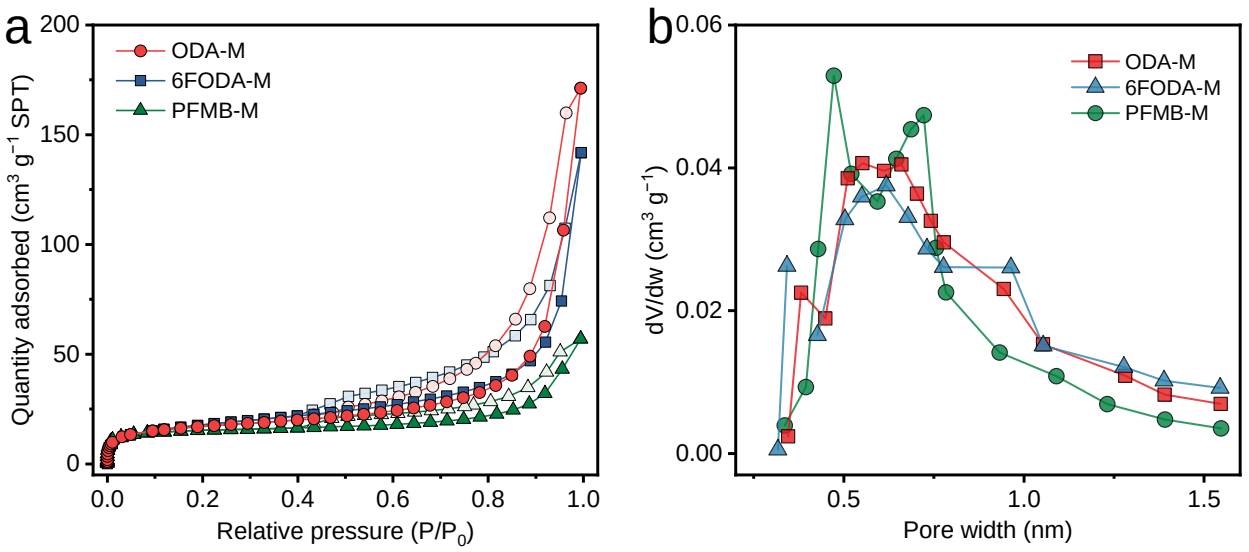


**Supplementary Fig. 30. Microporous structure analysis of polyamides based on $N_2$ sorption isotherms. a** $N_2$ adsorption-desorption isotherms at 77 K. **b** Pore size distribution curves obtained from the nonlocal density functional theory (NLDFT).

**Supplementary Note 31:** In line with the results derived from $CO_2$ sorption, the $N_2$ adsorption-desorption isotherms show that the Brunauer–Emmett–Teller (BET) surface area of the three polyamides follows a trend of ODA-M > 6FODA-M > PFMB-M, further corroborating the enhanced microporosity in ODA-M and 6FODA-M. The pore size distribution curves obtained reveal that the pore sizes of the three polyamides range from 5 to 12 Å, which are slightly larger than those calculated from the $CO_2$ sorption isotherms. This can be attributed to the relatively larger size of $N_2$ (0.36 nm) relative to $CO_2$ (0.33 nm), which makes it difficult to enter the small micropores within the polyamide. However, the average pore size obtained from the $N_2$ sorption data is approximately 6 Å, basically consistent with that determined from $CO_2$ sorption.

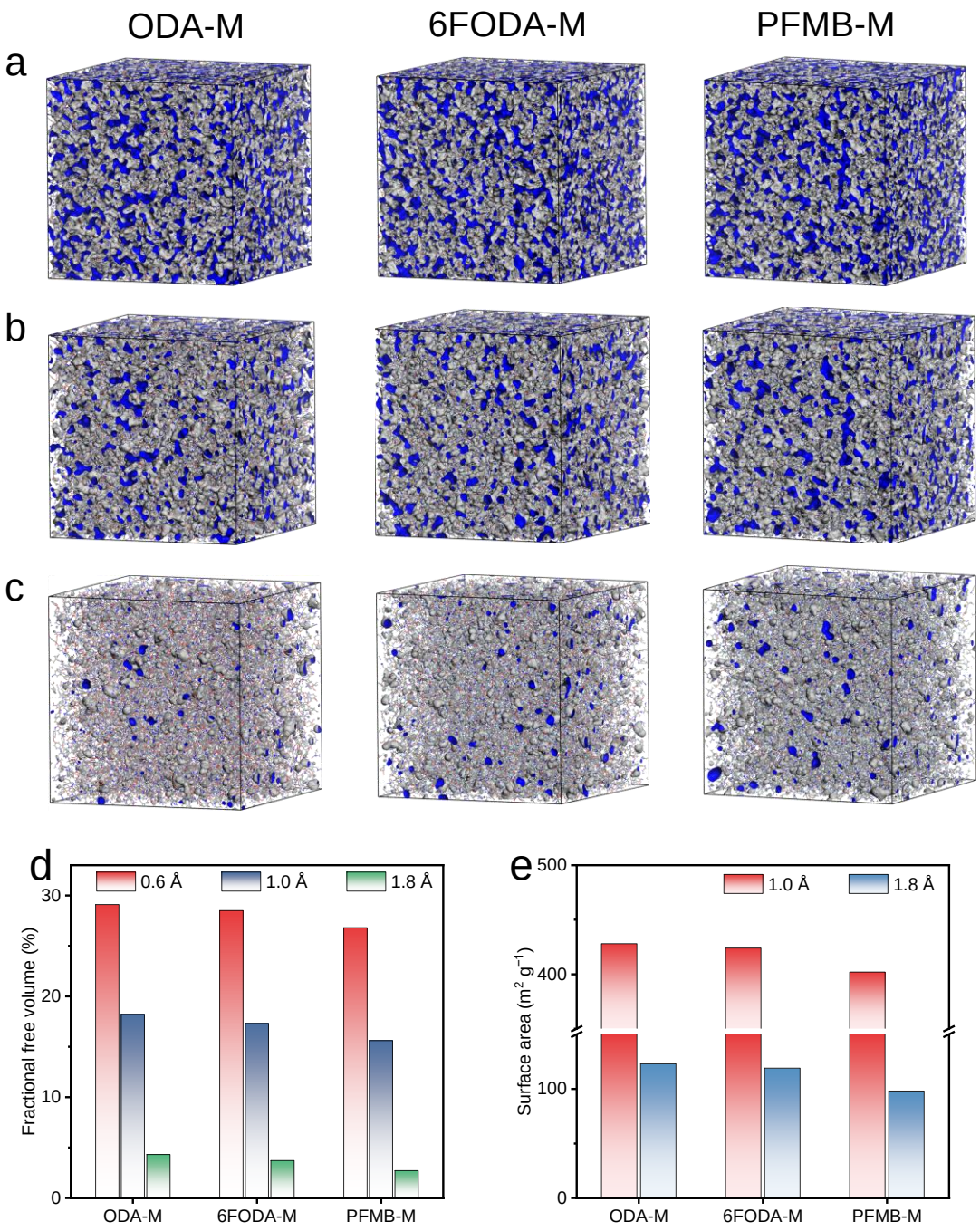


**Supplementary Fig. 31. Fractional free volume and surface area analysis of polyamides through MD simulations. a–c** Energy-minimized 3D cells and visualization of the accessible free volume with respect to different probes with a radius of 0.6 Å (**a**), 1.0 Å (**b**), and 1.8 Å (**c**). **d** Fractional free volume and **e** specific surface area derived from different probe sizes.

**Supplementary Note 32:** Based on the energy-minimized models of the three polymers constructed through MD simulations (Supplementary Fig. 3), realistic polymer structure models were constructed using probes of different sizes to analyze the microporous characteristics of the polyamide networks. Visualization of the energy-minimized 3D polymer cells with accessible free volumes shows that the microporosity of 6FODA-M and ODA-M polyamides was significantly higher than that of PFMB-M polyamide. Quantitative analysis of fractional free volume (FFV) and specific surface area (SSA) further confirms the consistent trend of ODA-M > 6FODA-M > PFMB-M across all probe sizes, which is in excellent agreement with the BET surface area measurements. In particular, the FFV values of ODA-M and 6FODA-M exceed 17.3%, and their specific surface areas surpass 424 $m^2 g^{-1}$ for a 1 Å probe, both substantially higher than PFMB-M. These results collectively demonstrate that the rotational flexibility of the phenyl rings around the ether linkages in the ODA and 6FODA monomers creates additional torsional space within the polyamide matrix, thereby reducing interchain packing density and promoting the formation of contorted non-coplanar conformations. This structural characteristic effectively enhances the intrinsic free volume and microporosity, which are crucial for the high solvent permeance observed in the corresponding polyamide membranes.

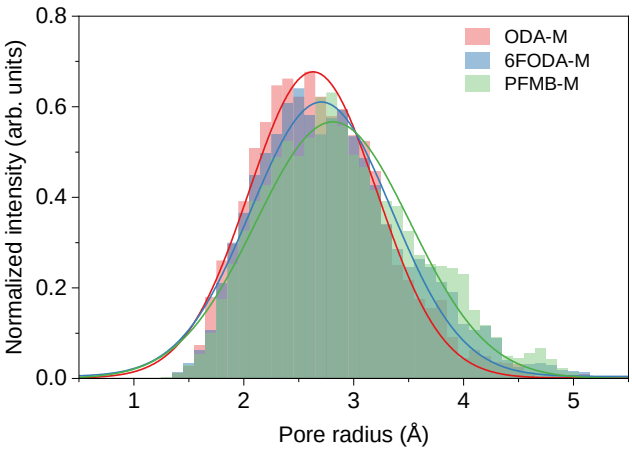


| | $r_p$ (Å) | $\sigma_p$ |
|---|---|---|
| ODA-M | 2.629 | 1.169 |
| 6FODA-M | 2.704 | 1.282 |
| 6FODA-M | 2.811 | 1.409 |

**Supplementary Fig. 32. Pore size distribution of the polyamides derived from MD simulations.** The table shows the average pore size and standard deviation of the pore size distribution curve determined by fitting a normal distribution.

**Supplementary Note 33:** To further confirm the explanation for the micropore uniformity of the polyamide membrane, the pore size distribution obtained from MD simulations was quantitatively analyzed. The distribution data were fitted using a normal function to derive the mean pore size and standard deviation (σ), which serve as indicators of pore size uniformity. The results suggest that the average pore sizes of ODA-M, 6FODA-M, and PFMB-M are 2.629, 2.704, and 2.811 Å, respectively, with corresponding σ values of 1.169, 1.282, and 1.409. These results clearly demonstrate that ODA-M and 6FODA-M possess narrower and more uniform pore size distributions than PFMB-M, which features a broader spread and slightly larger average pore size. This trend is consistent with their molecular architectures: the flexible ether linkages in the ODA and 6FODA monomers allow for local torsional motion, forming a highly interconnected and uniform microporous network. The contorted but spatially ordered packing of 6FODA-M and ODA-M facilitates the formation of well-defined microporous domains that are favorable for precise molecular sieving and rapid solvent permeation.

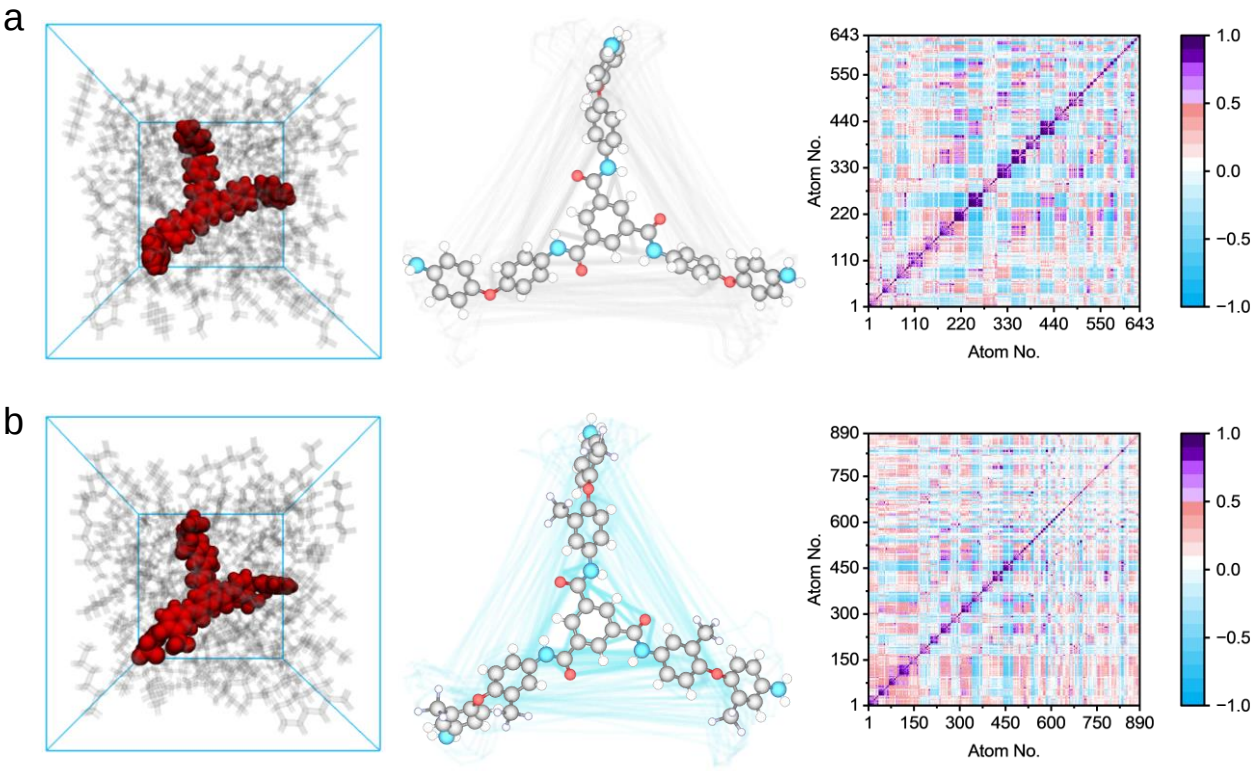


**Supplementary Fig. 33. a, b Polymer chain dynamics of ODA-M (a) and 6FODA-M (b) polyamides in the high-affinity solvent hexane.** The left figures exhibit the simulation box containing the hexane molecules and the polyamide fragments. The middle figures show the superimposed trajectories of ODA-M and 6FODA-M polyamides in hexane within 20 ns. Atoms color code: C, gray; O, red; N, blue; F, violet. The right figures display the dynamical cross-correlation matrix (DCCM) analysis of the polymer chain motions of the ODA-M and 6FODA-M polyamide fragments. For ODA-M and 6FODA-M, atoms numbered 1–509 and 510–645 are the atoms in the polyamide backbone linked by amide and ether bonds, respectively. Atoms with numbers 646–893 represent the segments containing $–CF_3$ groups in the polymer backbone of the 6FODA-M polyamide.

**Supplementary Note 34:** To evaluate the polymer chain dynamics of polyamides in the presence of high-affinity solvents, MD simulations at a 20 ns scale were performed in a representative nonpolar solvent environment. Specifically, representative polymer chain fragments of ODA-M

and 6FODA-M polyamides were placed in two simulation boxes filled with hexane molecules, and the superimposed motion trajectories of atoms in different regions of the polymer backbone in hexane were counted. Overall, the results show that 6FODA-M polyamide exhibits significantly suppressed chain dynamics in the presence of hexane compared with ODA-M, confirming the exceptional swelling resistance of the former in organic solvents. Further analysis of the trajectories and dynamical cross-correlation matrix (DCCM) of different regions in the two polyamide systems reveals that the atomic motions in different regions of ODA-M polyamide exhibit stronger positive/negative correlations relative to 6FODA-M. This reflects that the displacement tendency of atoms in ODA-M polyamide is greater than that of 6FODA-M in the hexane-solvated state, implying that ODA-M is more conformationally unstable in organic solvents.

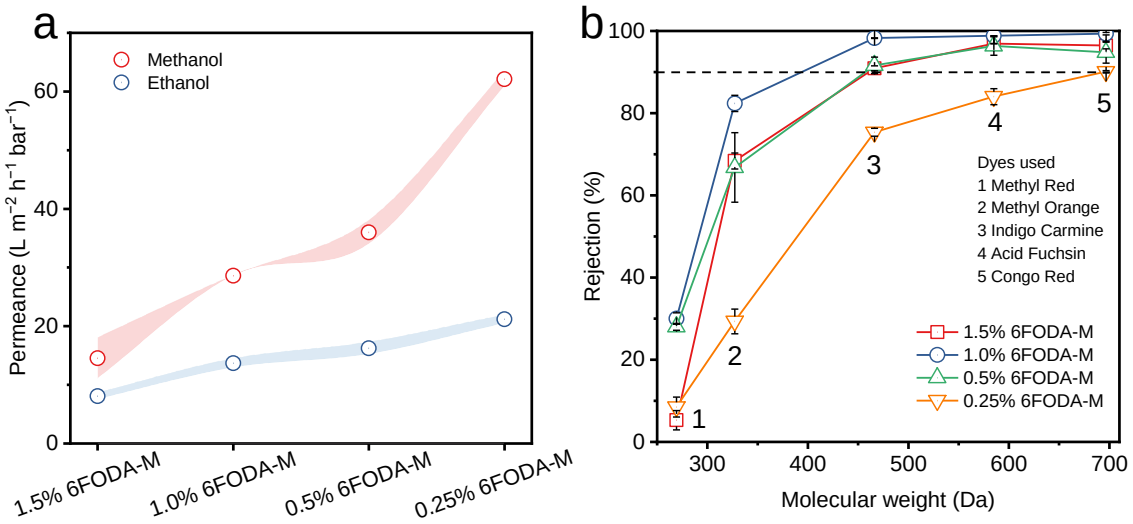


**Supplementary Fig. 34. Separation performance of 6FODA-M membranes prepared with different concentrations of 6FODA diamine monomer during IP. a** Methanol and ethanol permeance and **b** rejection profiles against model dye molecules with different molecular weights. The TMC concentration was kept at 0.1 wt/v% and the IP reaction time was 2 min. The 6FODA concentration was in the range of 0.25–1.5 wt/v%. Error bars represent the standard deviation obtained from three independent measurements.

**Supplementary Note 35:** During the in situ IP preparation of 6FODA-M polyamide TFC membranes, the solvent permeance significantly decreased with the increase in the concentration of 6FODA monomer, which is mainly due to the increased thickness of the polyamide dense layer. Concretely, when 6FODA concentration was raised from 0.25% to 1.0%, the methanol and ethanol permeance decreased from 62.1 and 21.2 L $m^{-2}$ $h^{-1}$ $bar^{-1}$ to 28.6 and 13.7 L $m^{-2}$ $h^{-1}$ $bar^{-1}$, respectively. Meanwhile, the MWCO of the membrane for model dye molecules decreased from nearly 700 Da to below 400 Da. Further increasing the monomer concentration led to a further drop in solvent permeance, but membrane rejections for small molecules remained essentially unchanged. As a result, the 6FODA monomer concentration was fixed at 1.0 wt/v% for the fabrication of the optimal 6FODA-M polyamide membrane.

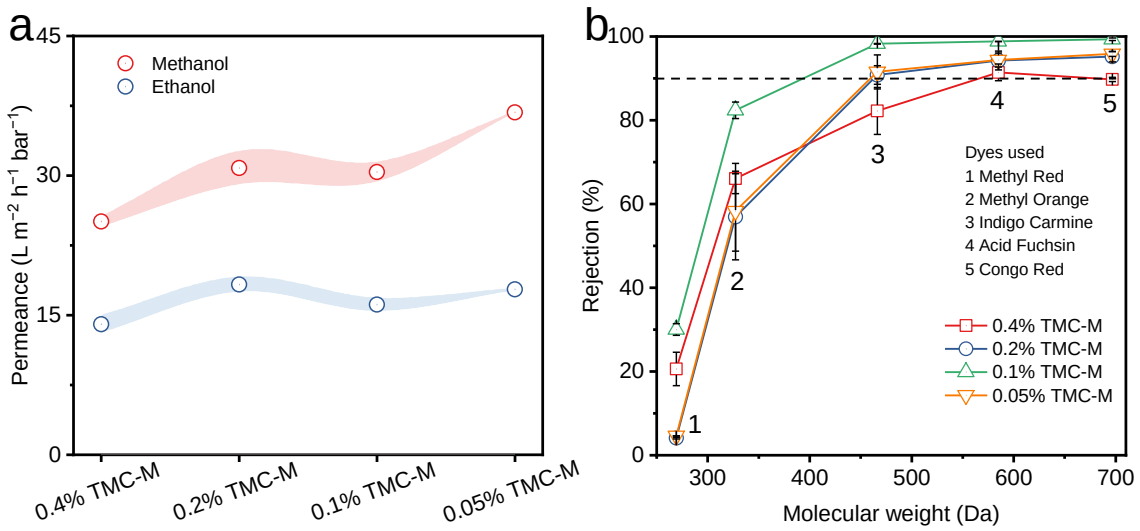


**Supplementary Fig. 35. Separation performance of 6FODA-M membranes prepared with different concentrations of TMC monomer during IP. a** Methanol and ethanol permeance and **b** rejection profiles against model dye molecules with different molecular weights. The 6FODA concentration was kept at 1.0 wt/v% and the IP reaction time was 2 min. The TMC concentration was in the range of 0.05–0.4 wt/v%. Error bars represent the standard deviation obtained from three independent measurements.

**Supplementary Note 36:** During the in situ IP preparation of 6FODA-M polyamide TFC membranes, the solvent permeance gently decreased with the increase of TMC monomer concentration, but the decline was not as significant as that of increasing 6FODA diamine monomer concentration, implying that the thickness of the polyamide layer is mainly affected by the concentration and diffusion of 6FODA monomer. For example, a 4-fold decrease in TMC concentration (from 0.4 to 0.1 wt/v%) only resulted in an approximately 10% increase in the permeance of methanol and ethanol. At the same time, the MWCO of the membrane decreased from nearly 600 Da to less than 400 Da. Nevertheless, further increases in TMC concentration led to a decline in molecule rejections and thus an increase in membrane MWCO. Therefore, the concentration of TMC monomer was fixed at 0.1 wt/v% for the fabrication of the optimal 6FODA-M polyamide membrane.

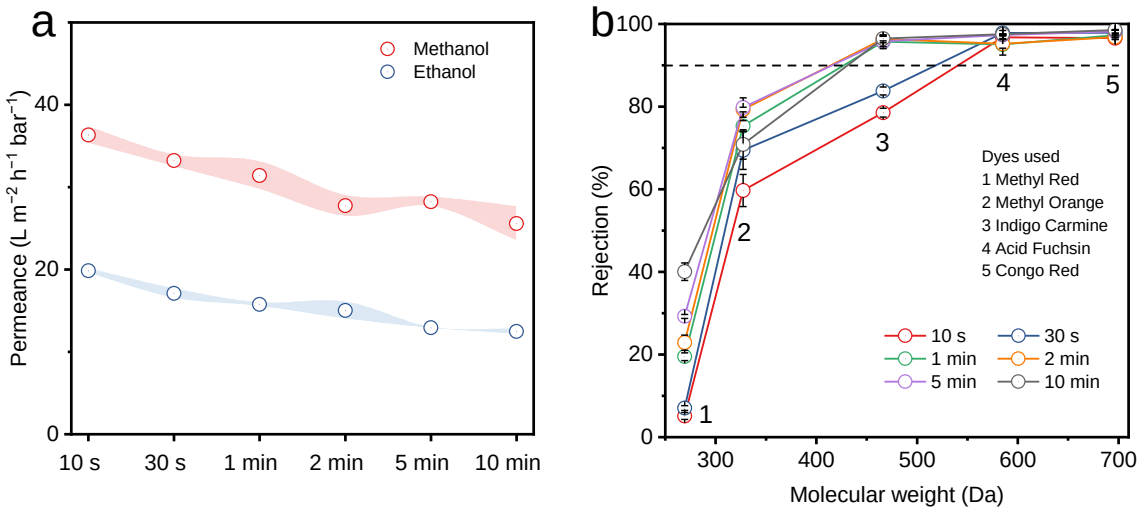


**Supplementary Fig. 36. Separation performance of 6FODA-M membranes prepared with different IP reaction times. a** Methanol and ethanol permeance and **b** rejection profiles against model dye molecules with different molecular weights. The 6FODA and TMC concentrations were 1.0 wt/v% and 0.1 wt/v%, respectively. The IP reaction time was in the range of 10 s to 20 min. Error bars represent the standard deviation obtained from three independent measurements.

**Supplementary Note 37:** When the IP reaction time was extended from 10 s to 20 min, the methanol and ethanol permeance of the 6FODA-M membrane decreased by about 30%, while the membrane MWCO for model dye molecules dropped from 542 to 413 Da. This time change corresponds to the transition of the polyamide layer from a thick and loose structure to a thin and dense structure during IP. Considering the tradeoff between solvent permeance and solute selectivity, the IP reaction time was fixed at 2 min to prepare the optimal 6FODA-M polyamide membrane.

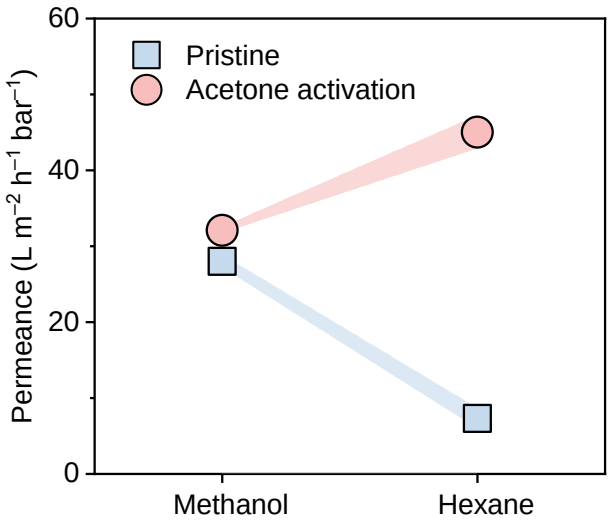


**Supplementary Fig. 37. Activation effect of acetone on 6FODA-M membrane.** Changes in solvent permeance of 6FODA-M membrane to polar solvent methanol and nonpolar solvent hexane before and after acetone activation. Error bars represent the standard deviation obtained from three independent measurements.

**Supplementary Note 38:** Before acetone activation, the permeance of the 6FODA-M membrane to nonpolar solvents such as hexane was relatively low. After filtering 50 mL of acetone, the hexane permeance significantly improved by an order of magnitude. This is because acetone stimulates the exposure of hydrophobic functional groups on polyamides[20], thereby enhancing the affinity of the 6FODA-M membrane to nonpolar solvents. It is noteworthy that the effect of such activation treatment is stable, where 6FODA-M maintained a high hexane permeance of larger than 40 L m$^{-2}$ h$^{-1}$ bar$^{-1}$ over a 3-day prolonged test after acetone activation. In contrast, acetone activation showed negligible changes in the permeance of polar solvents such as methanol.

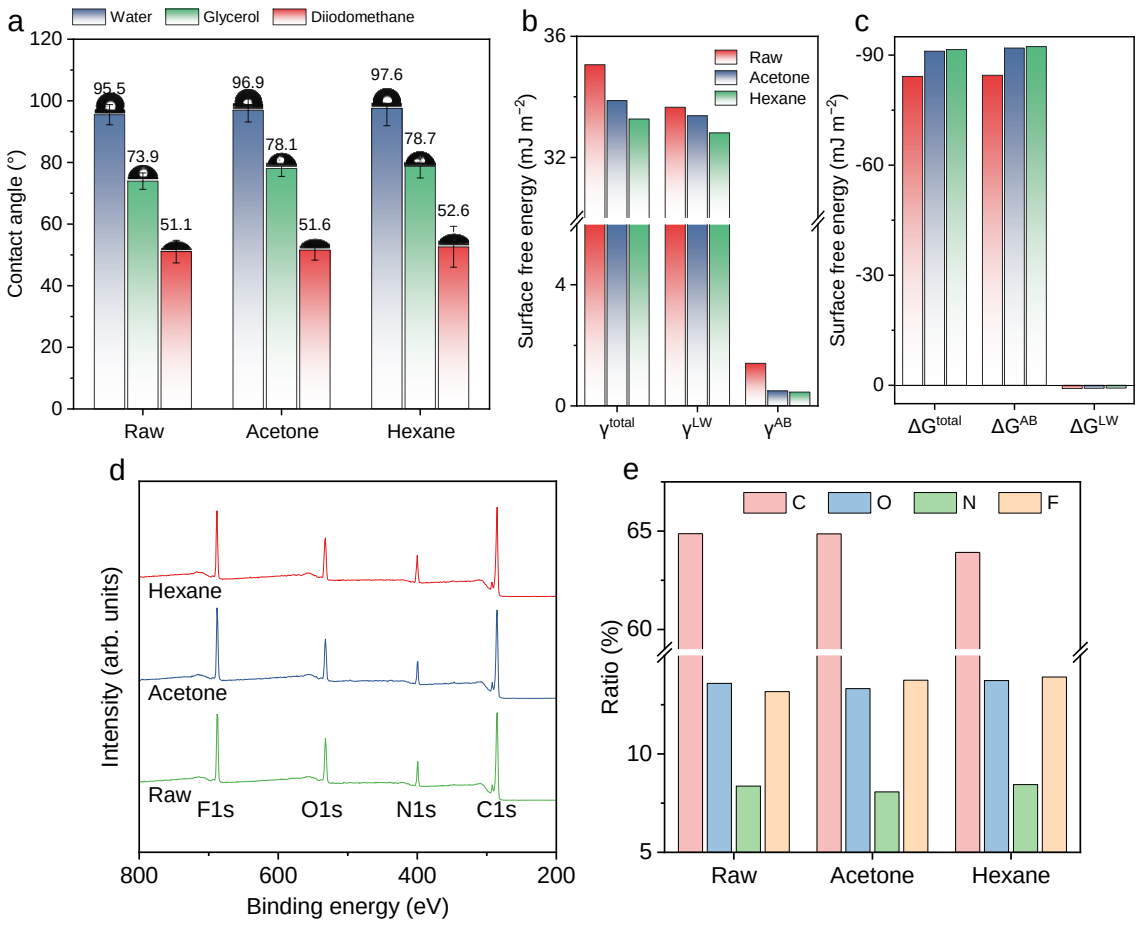


**Supplementary Fig. 38. Changes in the surface characteristics of 6FODA-M membrane before and after solvent activation. a** Surface contact angles of the raw (water-washed), acetone-activated, and acetone-activated plus hexane-soaked membranes with water, glycerol, and diiodomethane. Error bars represent the standard deviation obtained from three independent measurements. **b** Surface free energy parameters of the membranes. **c** Gibbs free energy parameters of hexane adhesion to the membranes. Surface free energy and Gibbs free energy were calculated from the surface contact angles (Supplementary Table 3) and the surface tension of the probe liquids (Supplementary Table 5). The subscript "total" indicates the total energy, while "LW" and "AB" refer to the components of the total energy caused by the Lifshitz–van der Waals and acid-base interactions, respectively. **d** XPS survey spectra and **e** surface elemental compositions of the membranes. Acetone activation and hexane soaking time were both 12 h.

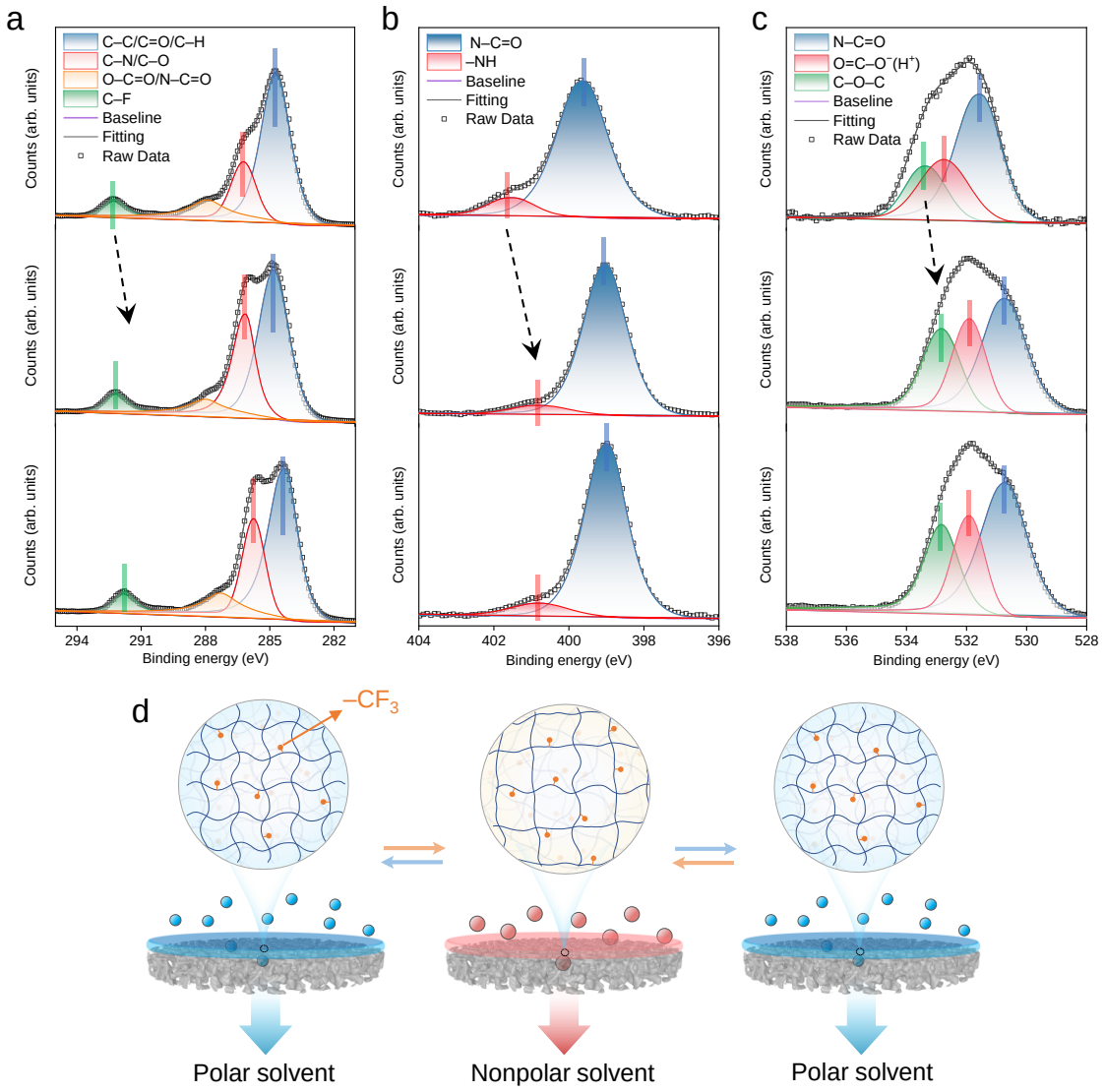


**Supplementary Fig. 39. Chemical structural characterization of the 6FODA-M membrane before and after solvent activation.** Core-level XPS spectra of **a** C 1*s*, **b** N 1*s*, and **c** O 1*s*. Both acetone activation and hexane immersion times are 12 h. Acetone activation and hexane soaking time were both 12 h. **d** Schematic illustration of the effects of solvent activation on polyamide.

**Supplementary Note 39:** To elucidate the changes in the physicochemical characteristics of the 6FODA-M membrane during acetone activation, we performed a set of complementary characterizations, including contact angle, surface energy, and XPS measurements. As shown in Supplementary Fig. 38, the water contact angle increases from 95.5° to 97.6° after acetone

treatment and hexane immersion, indicating enhanced surface hydrophobicity. Correspondingly, the total surface energy decreases from 35.1 to 33.3 mN $m^{-1}$, while the interaction energy with hexane significantly increases. These changes suggest that acetone exposure promotes the rearrangement and enrichment of hydrophobic $–CF_3$ moieties on the membrane surface, thereby improving the interfacial compatibility of the membrane with nonpolar solvents. XPS spectra further confirm the solvent-induced rearrangement of surface dipoles and chemical composition. After treatment with acetone and hexane, the C 1*s*, O 1*s*, and N 1*s* peaks shift towards lower binding energies by approximately 0.6–1.0 eV, indicating a decrease in surface dipole moment and an enhanced electron shielding effect. The N 1*s* peak shifts from 399.7 to 399.0 eV, consistent with the reorientation of surface amide dipoles. Simultaneously, the relative intensity of C–F species increases, and the contribution of N–H decreases, while the total percentage of F becomes higher. The combined evidence demonstrates that acetone activation induces reversible rearrangement of polyamide chain segments and surface dipole reorganization at the membrane interface, which enhances the affinity of 6FODA-M for nonpolar solvents such as hexane, leading to increased solvent permeance.

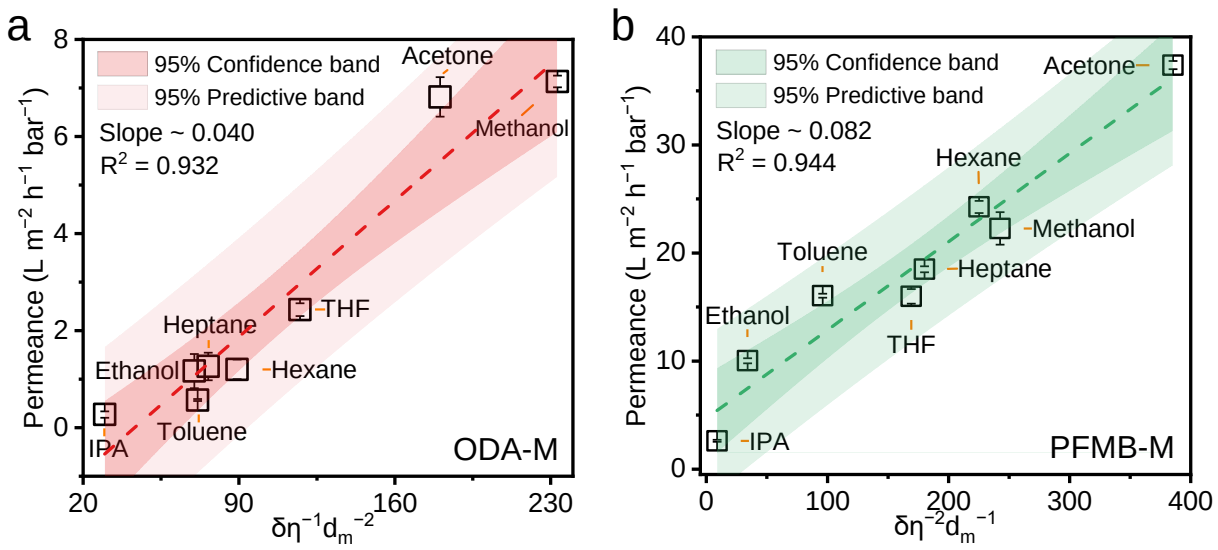


**Supplementary Fig. 40. Solvent permeance of ODA-M and PFMB-M membranes. a**, **b** Pure solvent permeance of methanol, ethanol, isopropanol (IPA), acetone, tetrahydrofuran (THF), toluene, hexane, and heptane through (**a**) ODA-M and (**b**) PFMB-M membranes against the combined characteristic parameters of the solvents. $d_m$, η, and δ represent the molar diameter, viscosity, and solubility parameter of the solvent, respectively. The dashed line in each figure fits a linear regression model. Error bars represent the standard deviation obtained from three independent measurements.

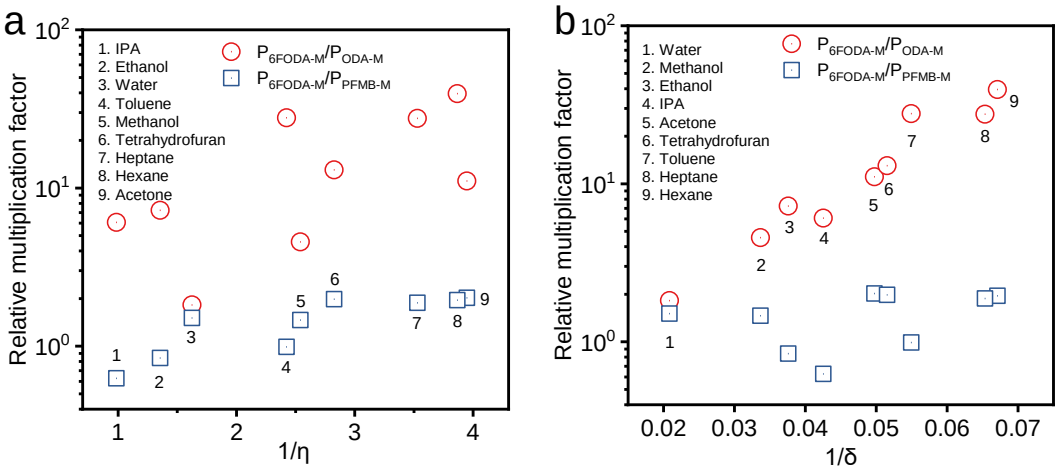


**Supplementary Fig. 41. Permeance enhancement of 6FODA-M relative to ODA-M and PFMB-M. a**, **b** Relative multiplication factor (e.g., $P_{6FODA\text{-}M}/P_{ODA\text{-}M}$ and $P_{6FODA\text{-}M}/P_{PFMB\text{-}M}$) as a function of the inverse of (**a**) viscosity (η) and (**b**) Hansen solubility parameter (δ) of the solvents.

**Supplementary Note 40:** The solvent permeance enhancement of 6FODA-M relative to ODA-M is more correlated with the molar diameter and the inverse of δ than with the inverse of η of the solvents, mainly due to the enhanced hydrophobicity of 6FODA-M polyamide imparted by the fluorinated polymer skeleton. In contrast, the advanced solvent permeance of 6FODA-M with respect to PFMB-M is highly correlated with the inverse of solvent viscosity (η), which indicates that the two membranes have similar affinities to the solvents, demonstrating that the significant enhancement of solvent permeance in 6FODA-M mainly stems from the increased microporosity. We also observed that the permeance improvement of 6FODA-M to nonpolar solvents relative to ODA-M was more pronounced than that to polar solvents. For example, although toluene, heptane, and hexane have greater inverse viscosities than acetone, their solvent permeance increases are much higher than that of acetone. In addition, the permeance enhancement of 6FODA-M relative to ODA-M for the three solvents with similar molar diameters follows the order of tetrahydrofuran > acetone > isopropanol, suggesting that the lower the solvent polarity, the more significant the solvent permeance improvement of 6FODA-M relative to ODA-M, which can be attributed to the

stronger affinity between the hydrophobic 6FODA-M polyamide and low-polarity and nonpolar solvents.

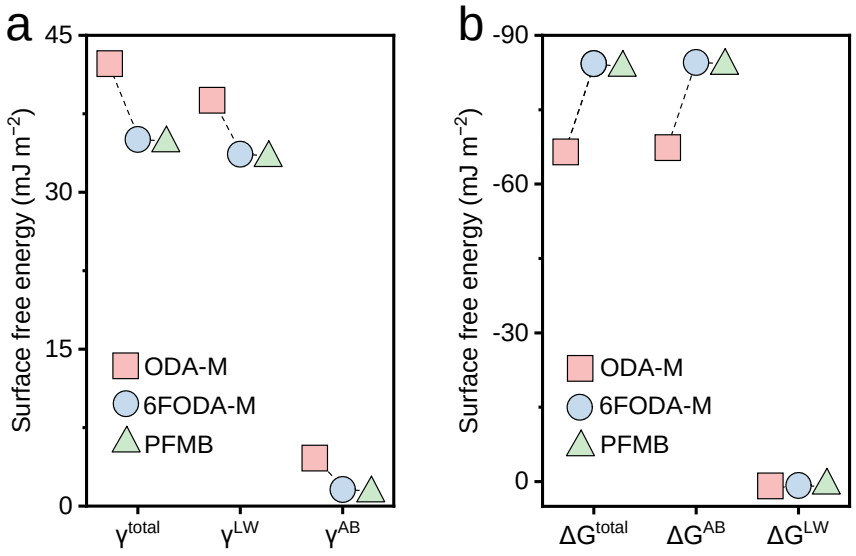


**Supplementary Fig. 42. a** Surface free energy parameters of the polyamide membranes. **b** Gibbs free energy parameters of hexane adhesion to the membranes. Surface free energy and Gibbs free energy were calculated from the surface contact angles (Supplementary Table 3) and the surface tension of the probe liquids (Supplementary Table 5). The subscript "total" indicates the total energy, while "LW" and "AB" refer to the components of the total energy caused by Lifshitz–van der Waals and acid-base interactions, respectively.

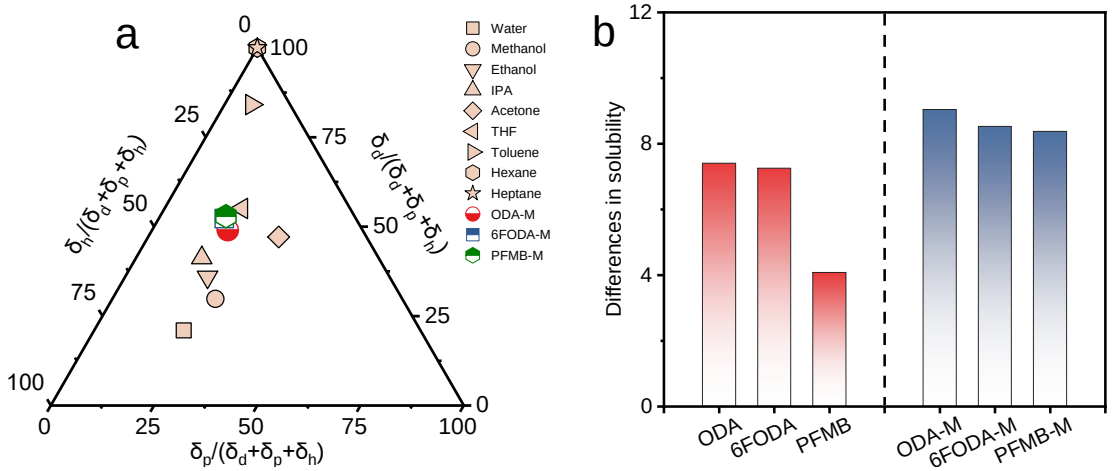


**Supplementary Fig. 43. Affinity analysis of polyamides with organic solvents of different polarities. a** Comparison of the Hansen solubility parameters (HSP) between nine solvents and three polyamides (estimated by the group contribution method) in the HSP diagram. **b** Relative distances of the HSP components of the diamine monomers and polyamides to the nonpolar solvent hexane.

**Supplementary Note 41:** The relative distance between the membrane and solvent in the Hansen solubility parameters (HSP) diagram (the modulus of the vector between solvent and membrane) reflects the relative affinity between them, wherein the closer the data point of the membrane is to the solvent, the stronger the mutual interaction. Specifically, the HSP diagram reveals that the relative distances between the 6FODA/PFMB monomers and nonpolar solvents (e.g., toluene, hexane, and heptane) are smaller than those of ODA. Further analysis of the HSP component distances of the polyamides relative to hexane suggests that the hydrophobic 6FODA-M and PFMB-M polyamides are closer to hexane in the diagram, indicating that they have stronger affinities to nonpolar solvents than ODA-M, mainly due to the presence of $–CF_3$ functional moieties in the former. We anticipate that the enhanced membrane-solvent affinity would promote solvent sorption on the membrane surface, which, in turn, facilitates the transmembrane permeation of solvents. Therefore, the broad-spectrum solvent compatibility of the 6FODA-M

membrane makes it more suitable for organic solvent nanofiltration applications than conventional polar polyamide membranes.

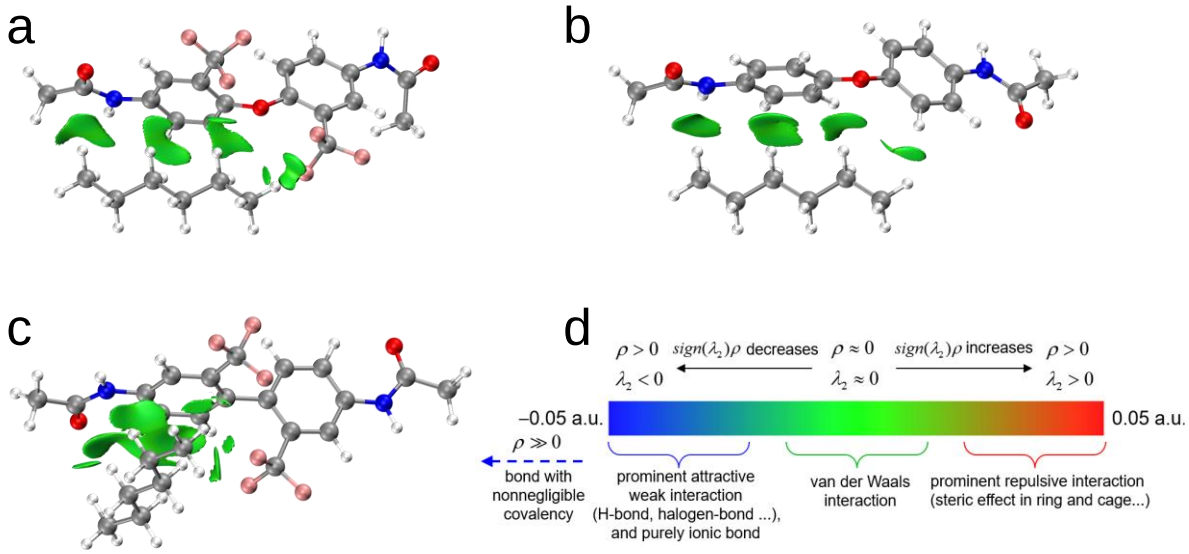


**Supplementary Fig. 44. a–c Molecular-level analysis of the interactions between polyamide membrane and hexane.** Independent gradient model based on Hirshfeld partition (IGMH) visualization of the interaction between hexane molecules and representative polyamide fragments of (**a**) 6FODA-M, (**b**) ODA-M, and (**c**) PFMB-M. **d** Interaction decomposition analysis of the binding configurations of polyamide fragments with hexane (blue, green, and red areas represent prominent attractive weak interaction, van der Waals interaction, and prominent repulsive interaction, respectively). Atoms color code: C, gray; O, red; N, blue; F, pink.

**Supplementary Note 42:** DFT calculations show that the mutual interaction between hexane and the representative polyamide fragments of PFMB-M and 6FODA-M is much greater than that of ODA-M. IGMH visualization further reveals that the introduction of $–CF_3$ pendants to the polymer significantly enhances the van der Waals interactions between polyamide and hexane molecules. These data demonstrate the strong affinity of PFMB-M and 6FODA-M to nonpolar solvents, which corresponds to their nonpolar solvent permeance being one order of magnitude higher than that of ODA-M.

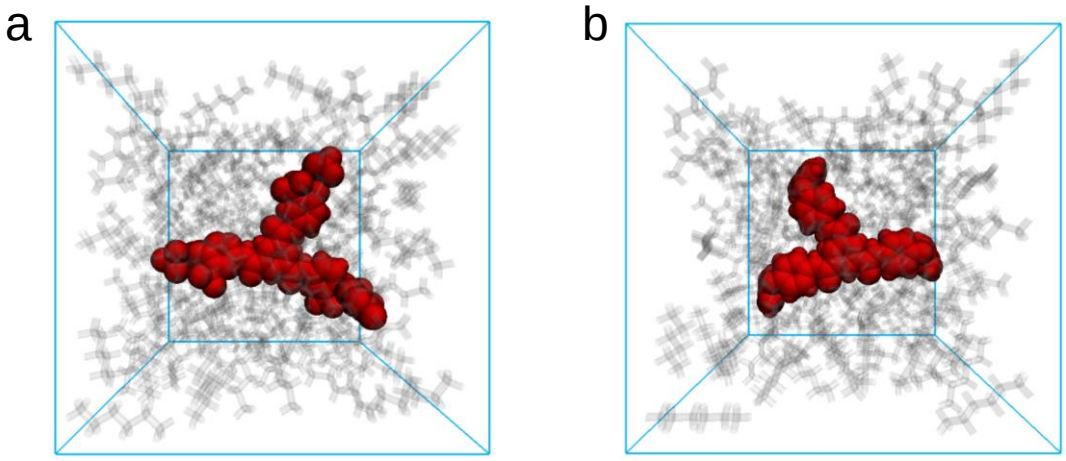


**Supplementary Fig. 45. a, b Simulation boxes of representative polyamide fragments of 6FODA-M (a) and ODA-M (b) in a hexane environment constructed by MD simulations.**

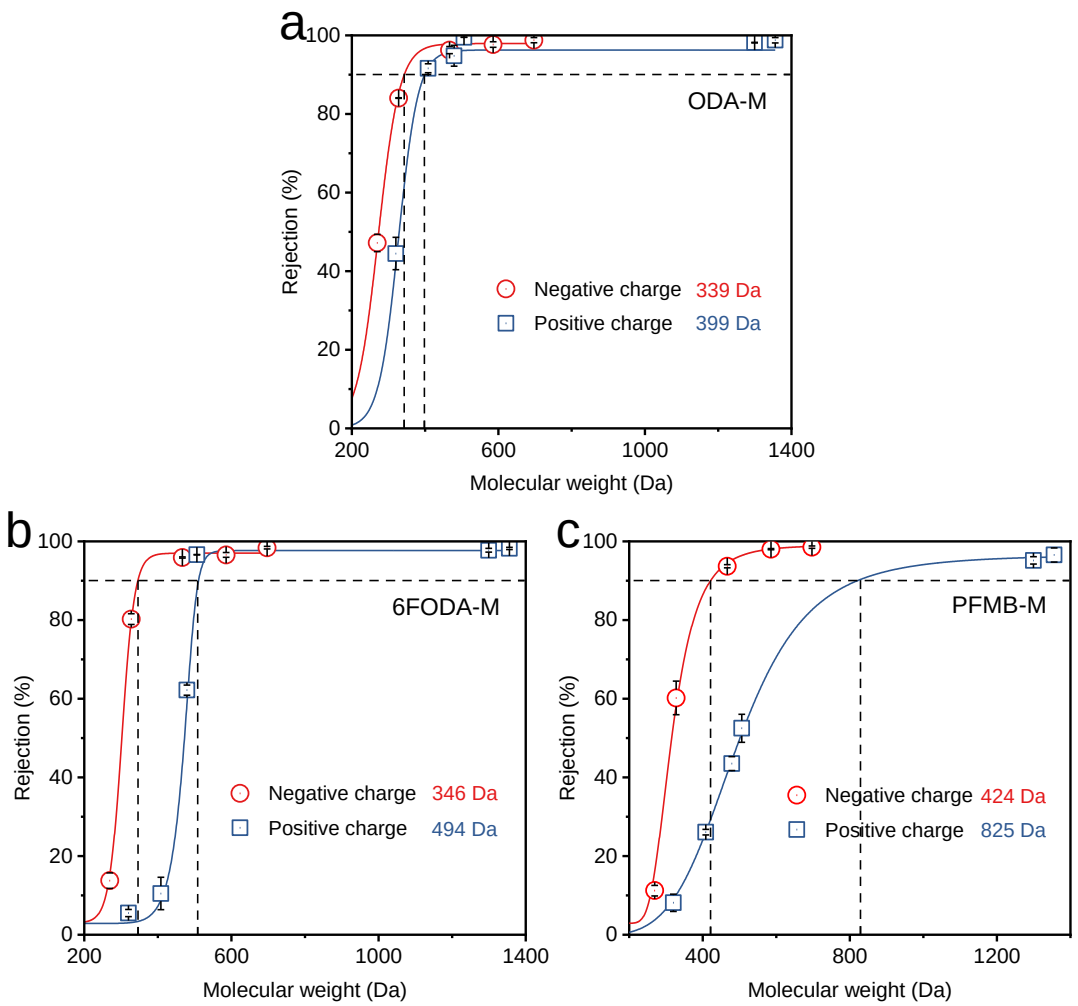


**Supplementary Fig. 46. Rejection profiles of polyamide membranes for negatively and positively charged dye molecules of different molecular weights in the polar solvent methanol.** **a** ODA-M, **b** 6FODA-M, and **c** 6PFMB-M. The filtration tests were performed at 3 bar, and the solute concentration in each feed was 50 ppm. Error bars represent the standard deviation obtained from three independent measurements.

**Supplementary Note 43:** In general, the retention rates of the three polyamide TFC membranes for model dye molecules increased with the increase of solute molecular weight, reflecting that size sieving plays a dominant role in solute retention. For the same solute, the rejection follows the order of ODA-M > 6FODA-M > PFMB-M, which corresponds to the crosslinking degree and pore size of the TFC membranes. Furthermore, the polyamide TFC membranes show significant

differences in the interception behavior of dye molecules with different charge properties in the polar solvent methanol, among which the rejections of negatively charged molecules are substantially higher than those of positively charged ones with similar molecular weights. This can be attributed to the partial dissociation of charged dye molecules in methanol, which allows the negative charges on the membrane surface to reject negatively charged solutes through electrostatic repulsion. Ultimately, the 6FODA-M membrane achieves a MWCO of 346 Da and 494 Da for positively and negatively charged small molecules, respectively, suggesting its great potential for precise molecular sieving in polar solvents.

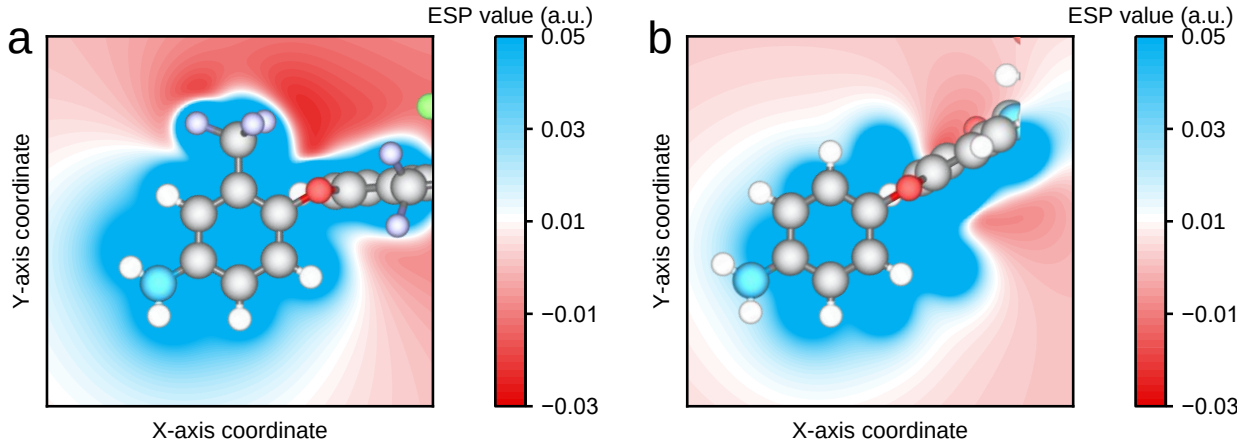


**Supplementary Fig. 47. a, b 2D projection of the electrostatic potential of 6FODA (a) and ODA (b) diamine monomers on the X-Y plane.** Atoms color code: C, gray; O, red; N, blue; F, violet.

**Supplementary Note 44:** 2D projection of the electrostatic potential of 6FODA and ODA diamine molecules derived from DFT calculations shows that 6FODA displays a strong negative electrostatic potential at the $–CF_3$ groups, which is attributed to the superior polarity and electronegativity of the three F atoms[21]. This can enhance the repulsive interaction between the 6FODA-M and the negatively charged molecules, thereby prompting membrane rejection.

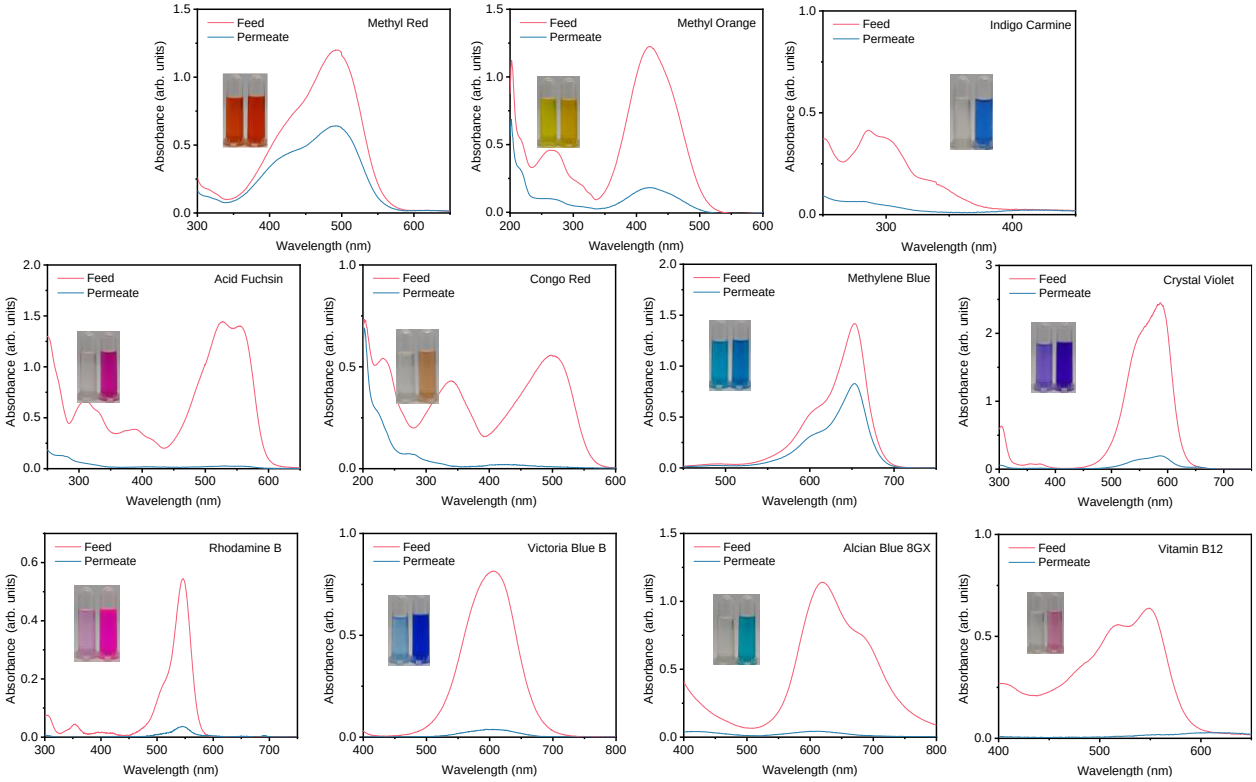


**Supplementary Fig. 48. UV-vis absorption spectra of the feed and permeate filtrated through the ODA-M membrane for dye molecules in methanol.** Inserts show photographs of the feed and permeate solutions. The filtration tests were performed at 3 bar using 50 ppm single-dye solutions in methanol as the feed.

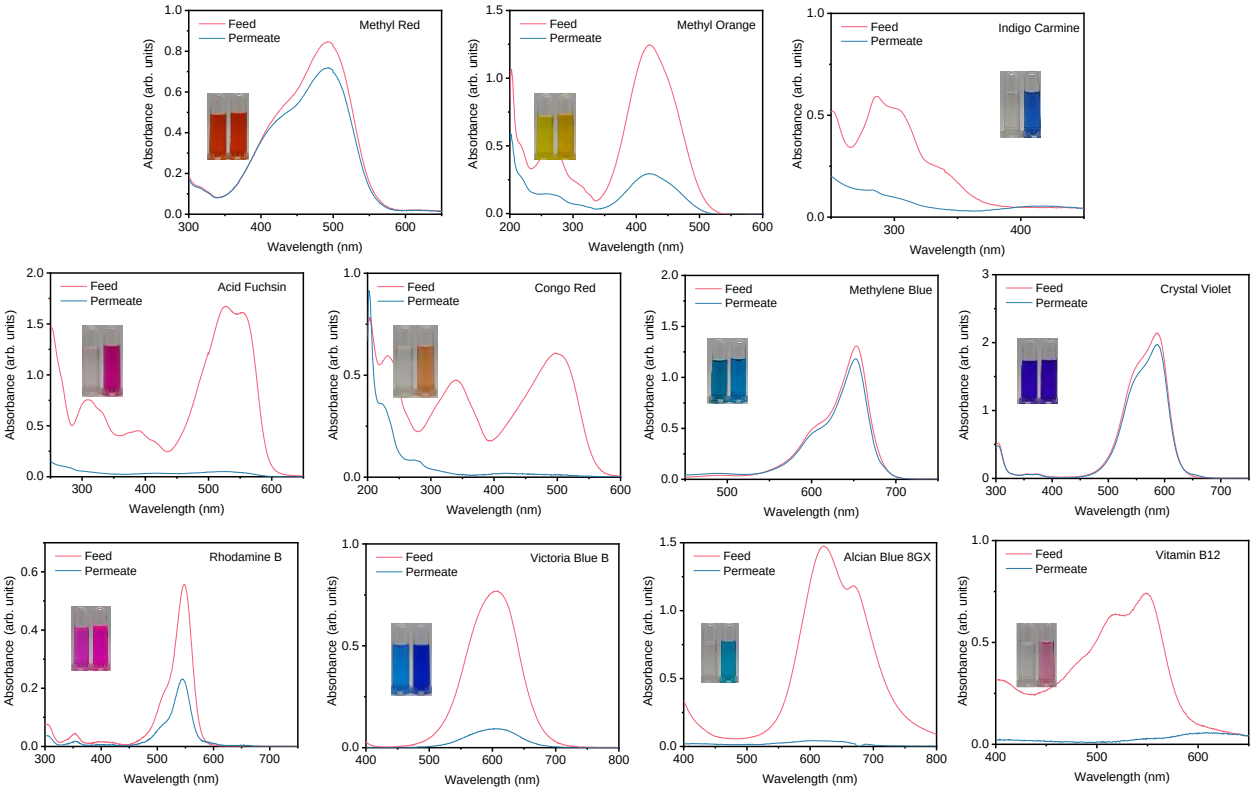


**Supplementary Fig. 49. UV-vis absorption spectra of the feed and permeate filtrated through the 6FODA-M membrane for dye molecules in methanol.** Inserts show photographs of the feed and permeate solutions. The filtration tests were performed at 3 bar using 50 ppm single-dye solutions in methanol as the feed.

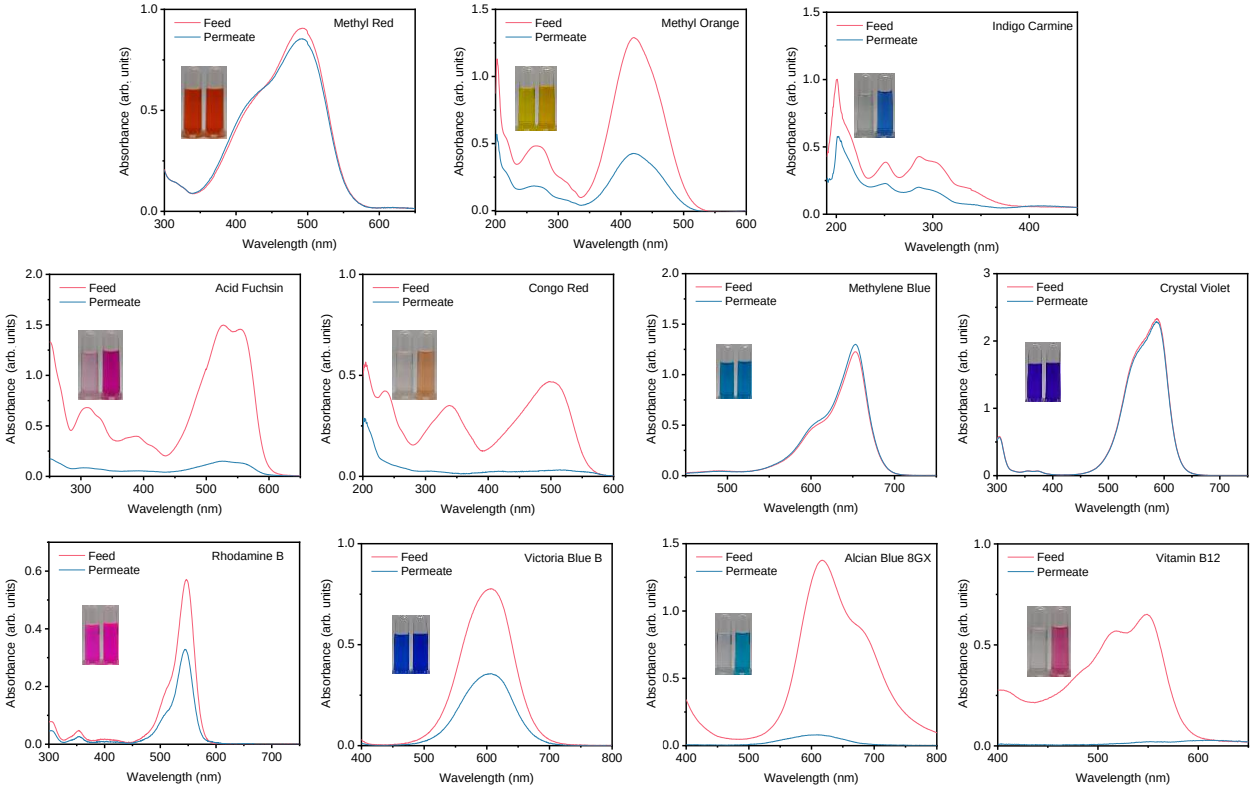


**Supplementary Fig. 50. UV-vis absorption spectra of the feed and permeate filtrated through the PFMB-M membrane for dye molecules in methanol.** Inserts show photographs of the feed and permeate solutions. The filtration tests were performed at 3 bar using 50 ppm single-dye solutions in methanol as the feed.

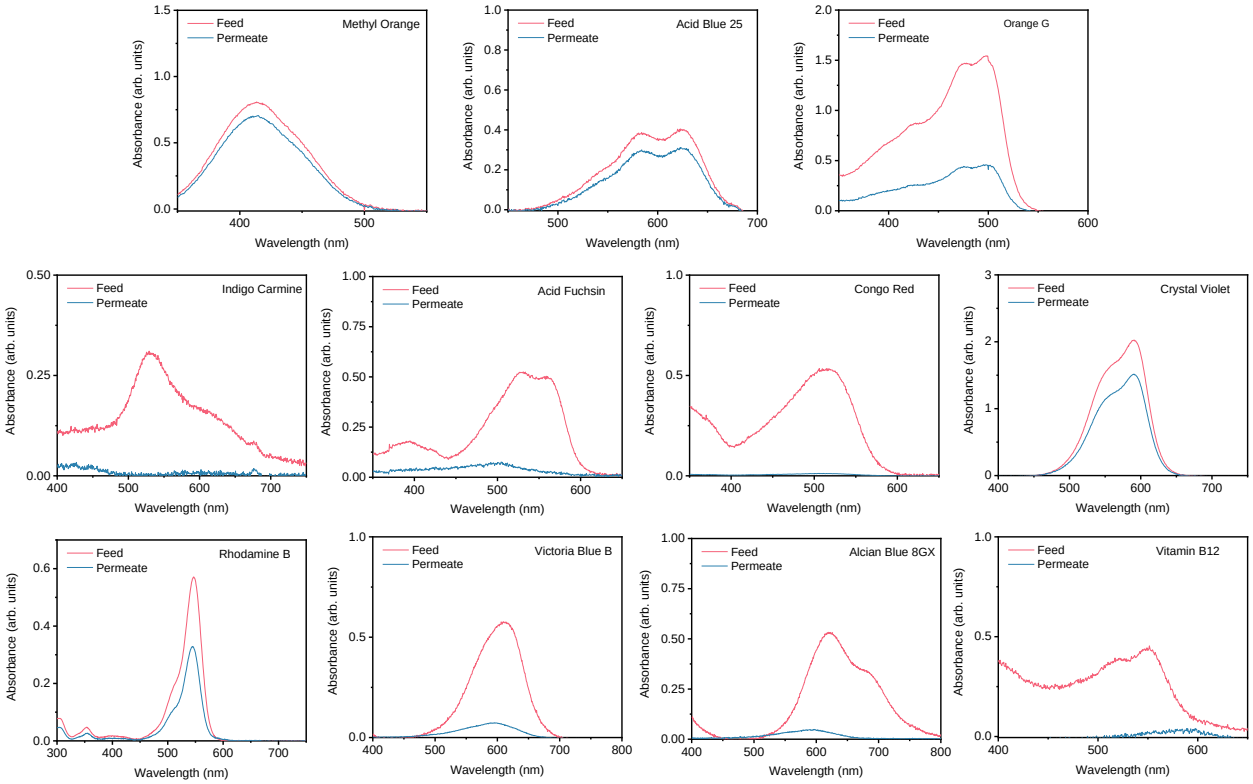


**Supplementary Fig. 51. UV-vis absorption spectra of the feed and permeate filtrated through the 6FODA-M membrane for dye molecules in acetone.** The filtration tests were performed at 3 bar using 20 ppm single-dye solutions in acetone as the feed.

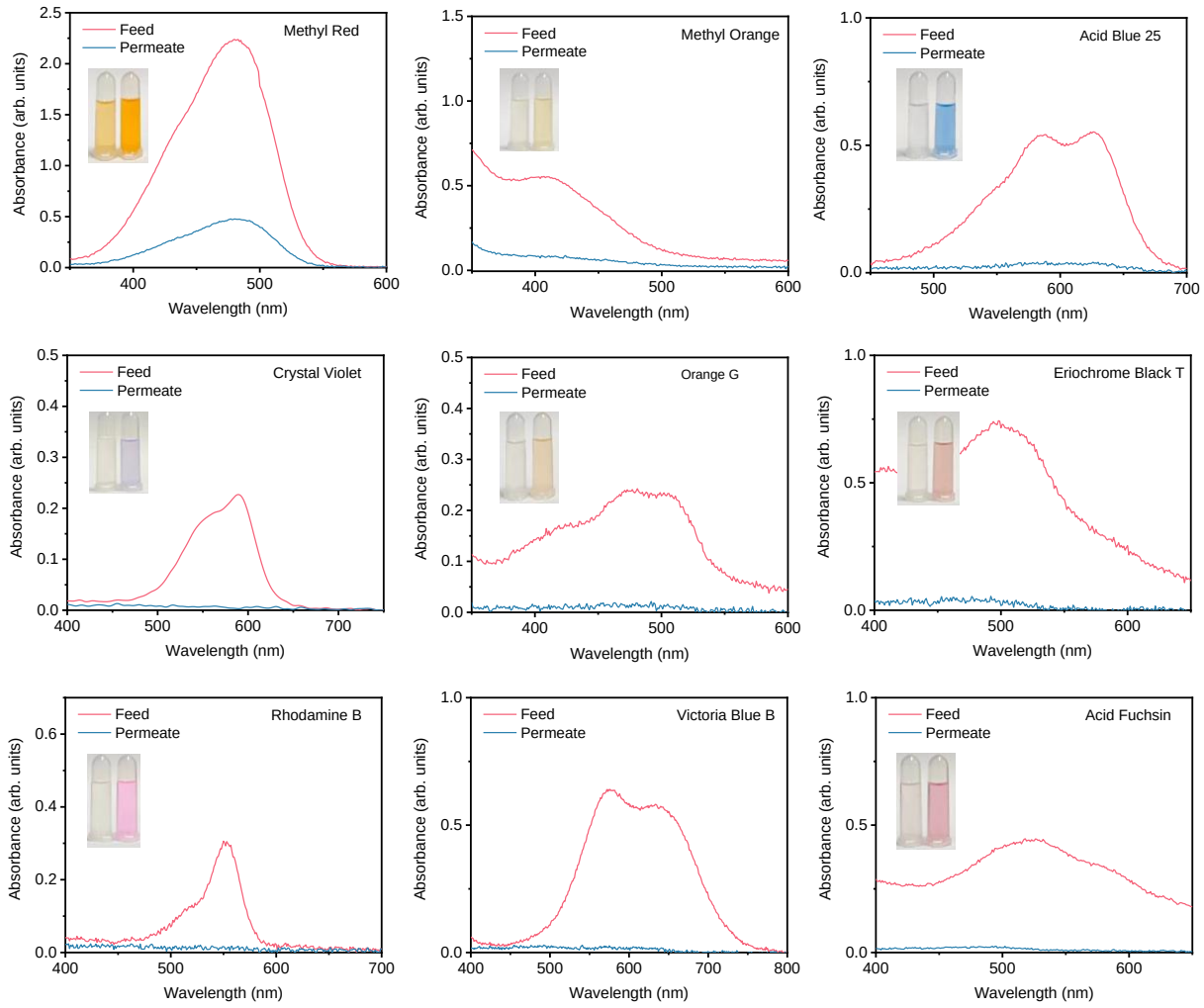


**Supplementary Fig. 52. UV-vis absorption spectra of the feed and permeate filtrated through the 6FODA-M membrane for dye molecules in hexane.** Inserts show photographs of the feed and permeate solutions. The filtration tests were performed at 3 bar using 10 ppm single-dye solutions in hexane as the feed.

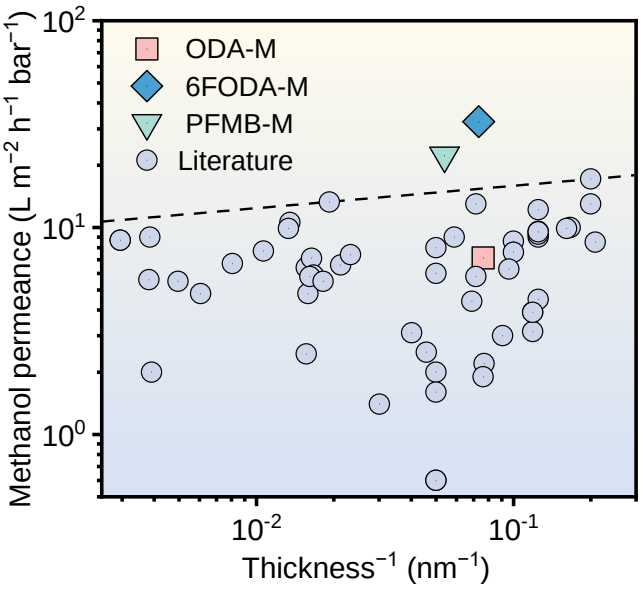


**Supplementary Fig. 53. Upper bound correlation of methanol permeance versus the reciprocal of selective layer thickness for the OSN membranes developed in this study and recently reported in the literature.** The detailed data points are summarized in Supplementary Table 13. The dashed line is an arbitrary trade-off line to guide the eye.

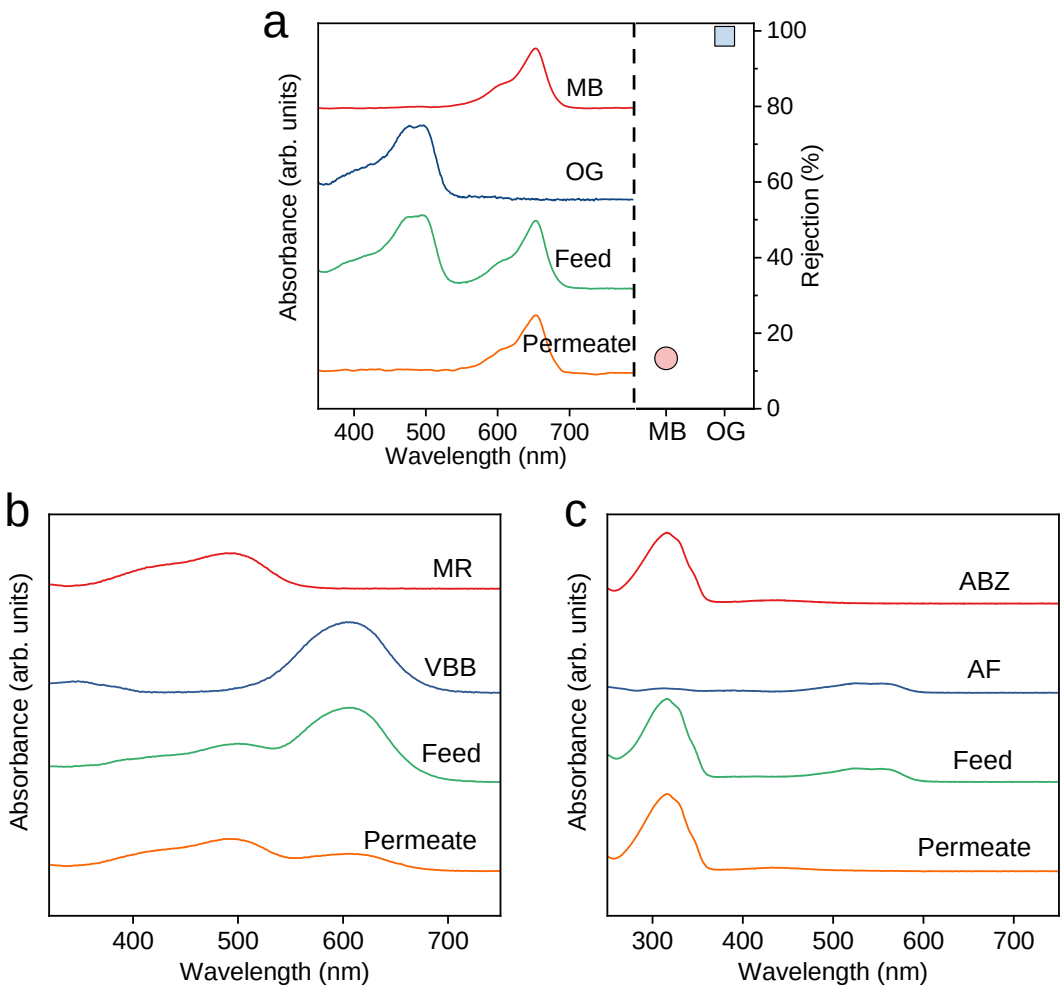


**Supplementary Fig. 54. UV-vis absorption spectra of the single-dye solutions, feed, and permeate for molecular sieving of binary dye mixtures in methanol using 6FODA-M membrane. a** MB (319.9 Da)/OG (452.4 Da), **b** MR (269.3 Da)/VBB (506.1 Da), and **c** ABZ (182.2 Da)/AF (585.5 Da). The filtration tests were performed at 3 bar, and the concentration of each component in the binary mixture was 25 ppm.

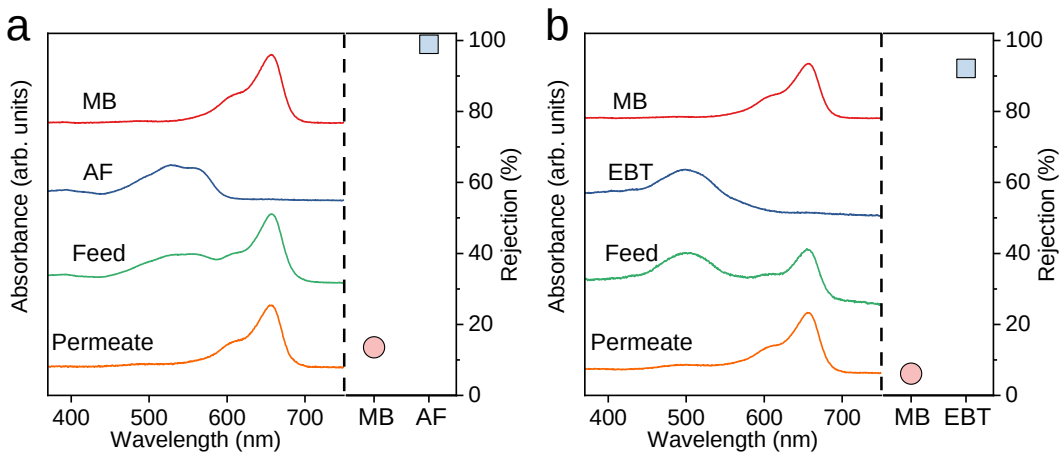


**Supplementary Fig. 55. UV-vis absorption spectra of the single-dye solutions, feed, and permeate for molecular sieving of binary dye mixtures in acetone using 6FODA-M membrane. a** MB (319.9 Da)/AF (585.5 Da) and **b** MB (319.9 Da)/EBT (461.4 Da) binary mixture in acetone. The solute rejections were included in the figures. The concentration of each solute was 10 ppm for the binary components.

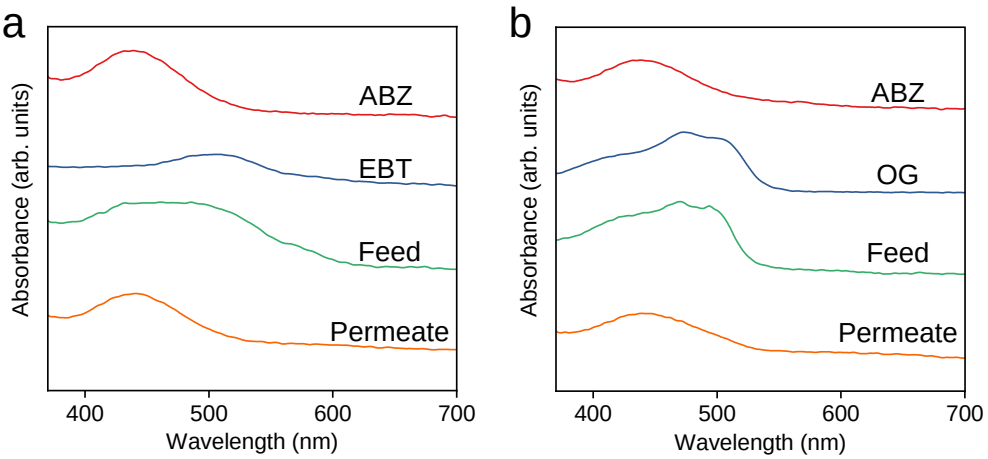


**Supplementary Fig. 56. UV-vis absorption spectra of the single-dye solutions, feed, and permeate for molecular sieving of binary dye mixtures in hexane using 6FODA-M membrane.** **a** ABZ (182.2 Da)/EBT (461.4 Da) and **b** ABZ (182.2 Da)/OG (452.4 Da). The filtration tests were performed at 3 bar, and the concentration of each component in the mixture was 5 ppm.

**Supplementary Note 45:** In the polar solvent methanol, binary mixtures of small and large dye molecules of (1) negatively charged MR (269.3 Da) and INCA (466.4 Da), (2) positively charged MB (319.9 Da) and negatively charged OG (452.4 Da), (3) negatively charged MR (269.3 Da) and positively charged VBB (506.1 Da), and (4) uncharged ABZ (182.2 Da) and negatively charged AF (585.5 Da) were used as the solutes for the filtration tests. Since some dye molecules are poorly soluble in the moderately polar solvent acetone and the nonpolar solvent hexane, the number of dyes used for the filtration was diminished. For the filtration tests in acetone, binary mixtures of (1) positively charged MB (319.9 Da) and negatively charged AF (585.5 Da), and (2) positively charged MB (319.9 Da) and negatively charged EBT (461.4 Da) were employed as the solutes. For the filtration tests in hexane, binary mixtures of (1) uncharged ABZ (182.2 Da) and negatively charged EBT (461.4 Da), and (2) uncharged ABZ (182.2 Da) and negatively charged OG (452.4 Da) were used as the solutes. UV-vis spectroscopy data indicate that 6FODA-M can precisely separate two dye molecules of different sizes and charges in binary mixtures with high solvent permeance over a wide range of solvent polarity.

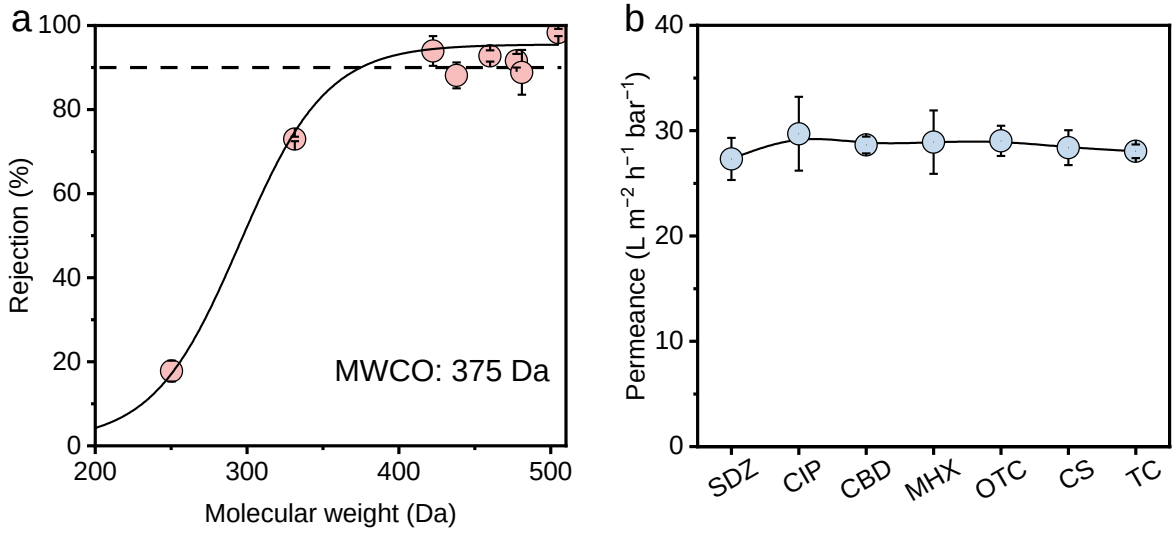


**Supplementary Fig. 57. Separation of small pharmaceutical molecules in methanol by 6FODA-M membrane. a** Rejection profile for pharmaceutical molecules of different molecular weights. **b** Methanol permeance during the separation of different pharmaceutical molecules. The filtration tests were performed at 3 bar, and the solute concentration of each molecule in methanol was 5 ppm. Error bars represent the standard deviation obtained from three independent measurements.

**Supplementary Note 46:** The 6FODA-M membrane shows high rejections for small pharmaceutical molecules, with a low MWCO of 375 Da in methanol. Simultaneously, the membrane still maintained ultrahigh methanol permeance of about 30 L m$^{-2}$ h$^{-1}$ bar$^{-1}$, which is almost the same as the permeance of pure methanol, further demonstrating the great potential of the 6FODA-M membrane for precise molecular separation in organic solvents.

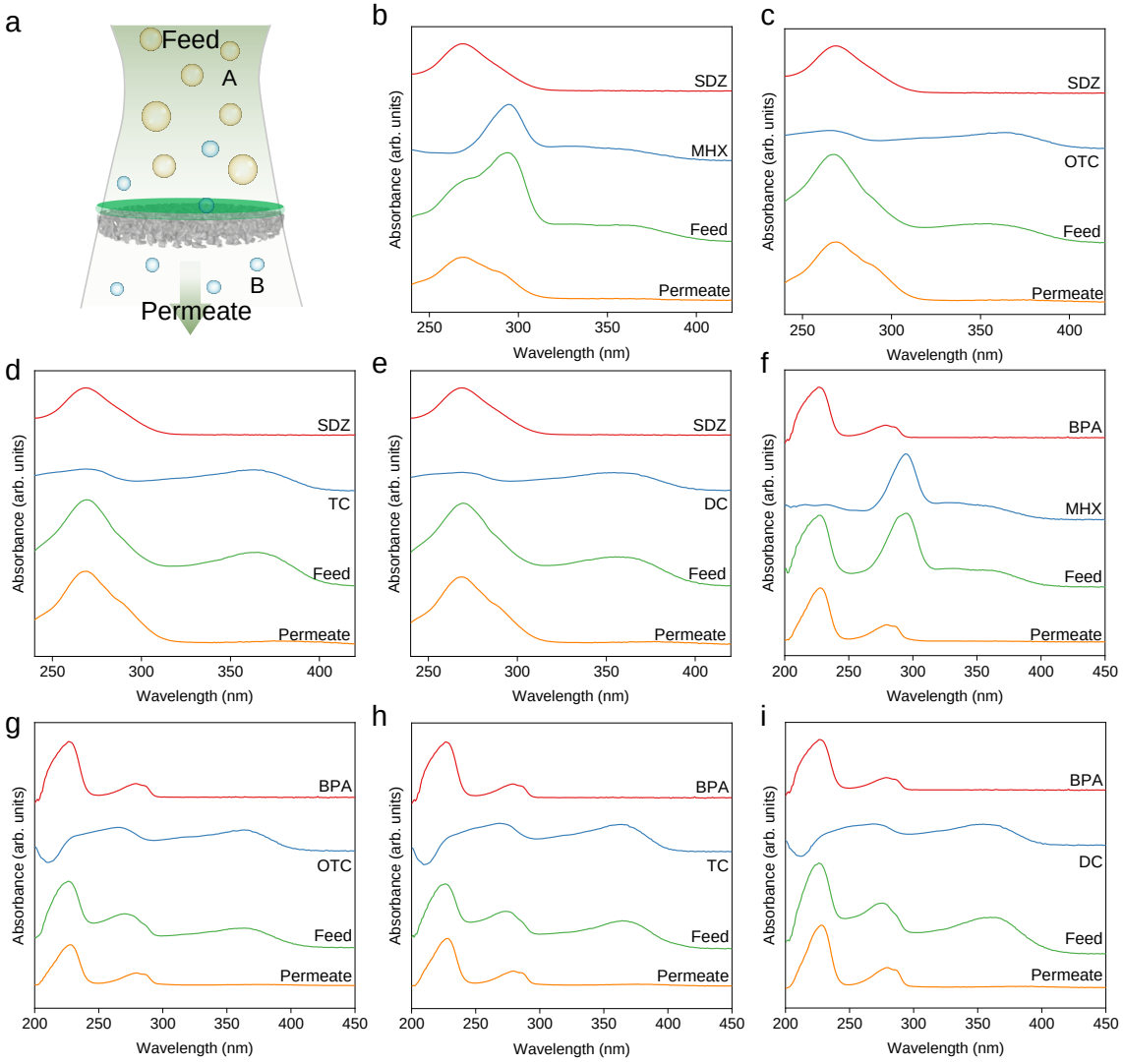


**Supplementary Fig. 58. Separation of pharmaceutical/industrial compound binary mixtures in methanol using 6FODA-M membrane. a** Schematic illustration of the selective separation of solutes with different sizes. **b**–**i** UV–vis absorption spectra of single-compound solutions, mixed solute feed solutions, and permeate of binary pharmaceutical mixtures: **b** sulfadiazine (SDZ, 319.9 Da)/moxifloxacin hydrochloride (MHX, 437.9 Da), **c** SDZ/oxytetracycline (OTC, 460.4 Da), **d** SDZ/tetracycline hydrochloride (TC, 480.8 Da), **e** SDZ/doxycycline hydrochloride (DC, 444.4 Da), **f** Bisphenol A (BPA, 228.3 Da)/MHX, **g** BPA/OTC, **h** BPA/TC, and **i** BPA/DC. The filtration tests were performed at 3 bar, and the concentration of each component in the binary mixture was 5 ppm.

**Supplementary Note 47:** Additional tests were conducted to investigate the practical application potential of the 6FODA-M membrane in separating pharmaceutical mixtures. In a representative SDZ/MHX binary system, the absorption peak intensity of SDZ in the UV-vis spectrum of the permeate decreases slightly compared to the feed, while a pronounced attenuation of MHX absorption peak intensity was observed in the permeate, indicating that the 6FODA-M membrane effectively retains larger solutes while allowing smaller molecules to permeate freely, even under competitive diffusion conditions. The separation performance for a series of mixed solute systems containing low molecular weight solutes (SDZ and BPA) and high molecular weight pharmaceuticals (MHX, OTC, TC, and DC (doxycycline hydrochloride, 480.9 Da)) was further examined. As shown in the Supplementary Fig. 58, the 6FODA-M membrane consistently maintains high selectivity, with a rejection of less than 30% for small molecule solutes and a high retention rate of 85–95% for large molecule solutes. These results confirm that the 6FODA-M membrane retains its superior molecular sieving capability even in multi-component feeds. Combined with its high permeance and excellent solute selectivity, the 6FODA-M membrane demonstrates great potential in organic solvent nanofiltration for drug purification and solvent recovery.

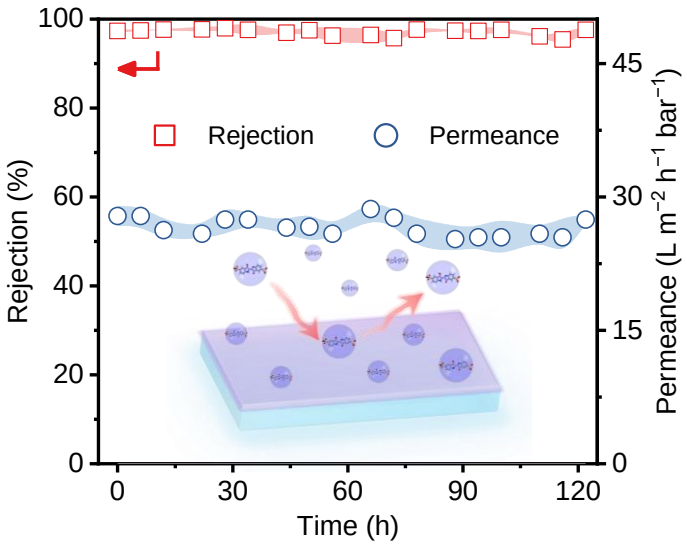


**Supplementary Fig. 59. Long-term performance stability of the 6FODA-M membrane.** Methanol permeance and INCA rejection during a long-term continuous filtration test of 120 h. The filtration tests were performed at 3 bar, and the INCA concentration in methanol was 50 ppm. Error bars represent the standard deviation obtained from three independent measurements.

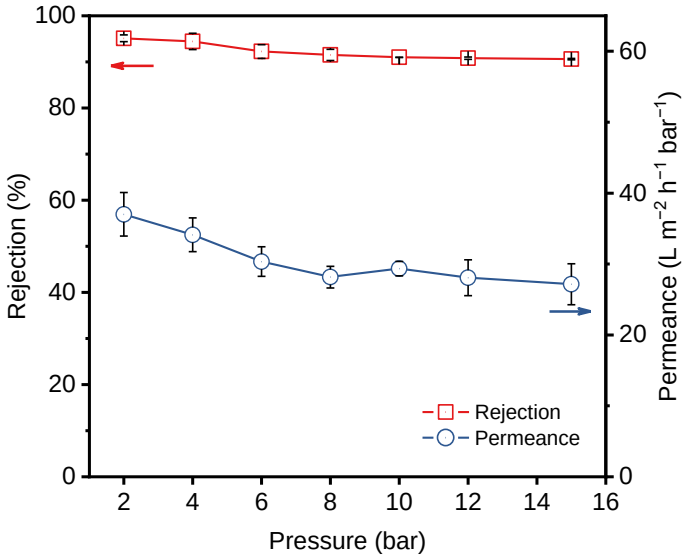


**Supplementary Fig. 60. Pressure stability of 6FODA-M membrane.** Methanol permeance and INCA rejection at different operating pressures using a 50 ppm INCA solution in methanol as the feed. Error bars represent the standard deviation obtained from three independent measurements.

**Supplementary Note 48:** The 6FODA-M membrane maintained relatively stable methanol permeance and INCA rejection at operating pressures from 2 to 15 bar. Although the methanol permeance decreased slightly with increasing test pressure, probably due to membrane compaction, the INCA rejection remained stable. The 6FODA-M membrane exhibited high methanol permeance (> 27 L m$^{-2}$ h$^{-1}$ bar$^{-1}$) and INCA rejection (> 90%) even at a high pressure of 15 bar, signifying the outstanding structural robustness of the developed polyamide membranes.

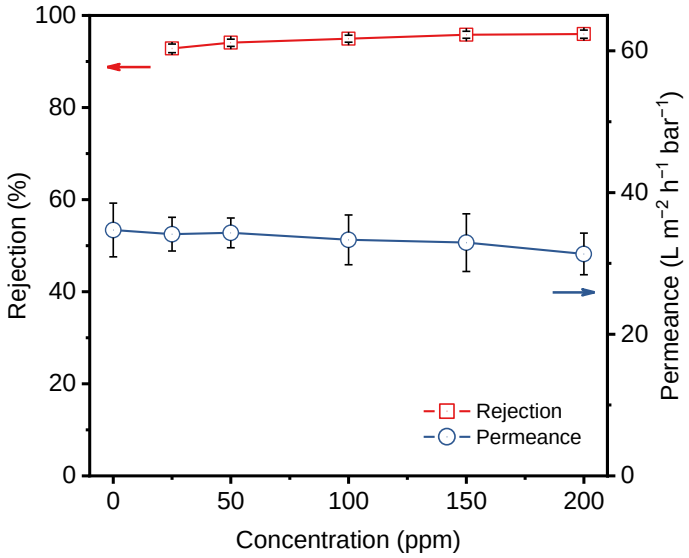


**Supplementary Fig. 61. Performance stability of 6FODA-M membrane against dye concentration.** Methanol permeance and INCA rejection for feed solutions with different INCA concentrations. The filtration tests were performed at 3 bar. Error bars represent the standard deviation obtained from three independent measurements.

**Supplementary Note 49:** The 6FODA membrane consistently shows stable methanol permeance and INCA rejection over a wide range of INCA concentrations in the feed solution, demonstrating stable size-sieving capacity for small molecules at different contents in organic solvents.

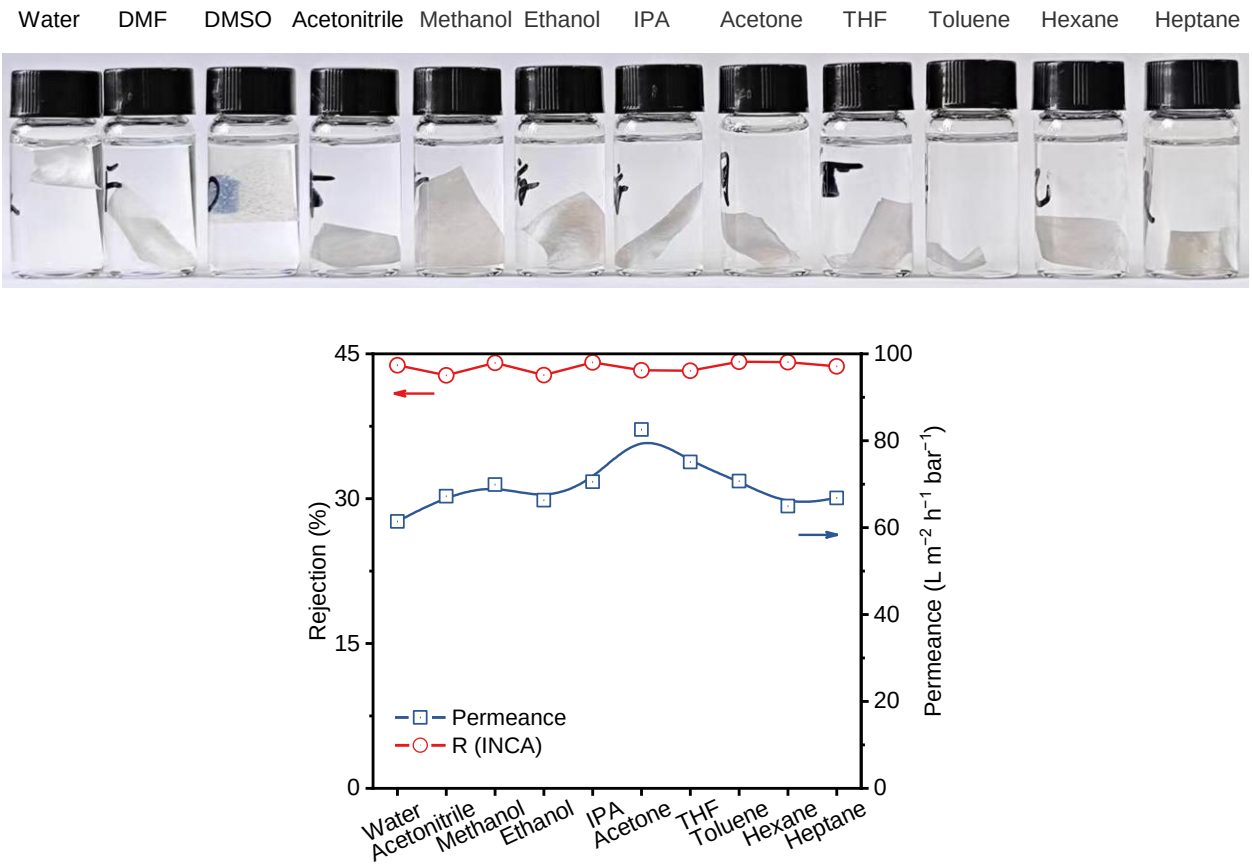


**Supplementary Fig. 62. Solvent stability of 6FODA-M membrane.** Membrane photographs after immersion in different solvents for 7 days (top). Methanol permeance and INCA rejection after immersion in different solvents for 7 days (bottom). The filtration tests were performed at 3 bar, and the INCA concentration in the feed was 50 ppm.

**Supplementary Note 50:** After the polyamide nanofilm of the 6FODA-M membrane was immersed in different solvents for 7 days, the film structure remained intact, corroborating its excellent structural stability in organic solvents of different polarities. The methanol permeance and INCA rejection of the 6FODA-M membrane after immersion in each solvent were tested, and the results show that the methanol permeance remained stable at 30 L $m^{-2}$ $h^{-1}$ $bar^{-1}$, while the INCA rejection was > 95%, demonstrating the excellent applicability of 6FODA-M in different solvent systems.

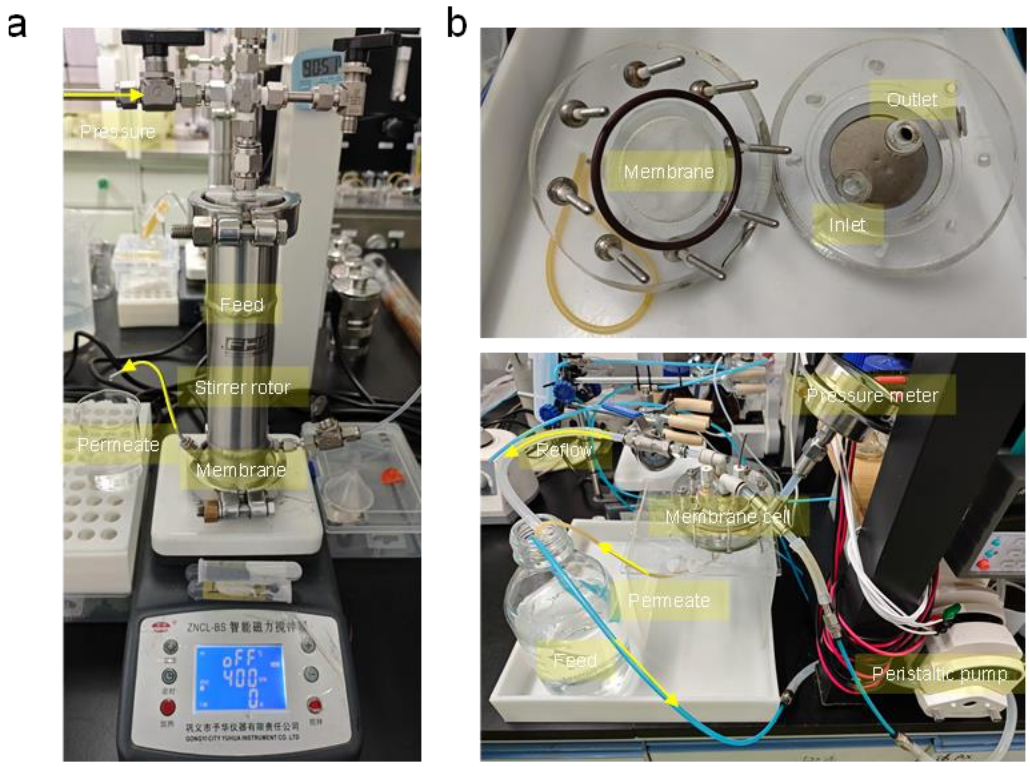


**Supplementary Fig. 63. Photographs of the filtration setups used for OSN testing. a** Laboratory-fabricated stirred dead-end filtration cell. **b** Homemade crossflow filtration system.

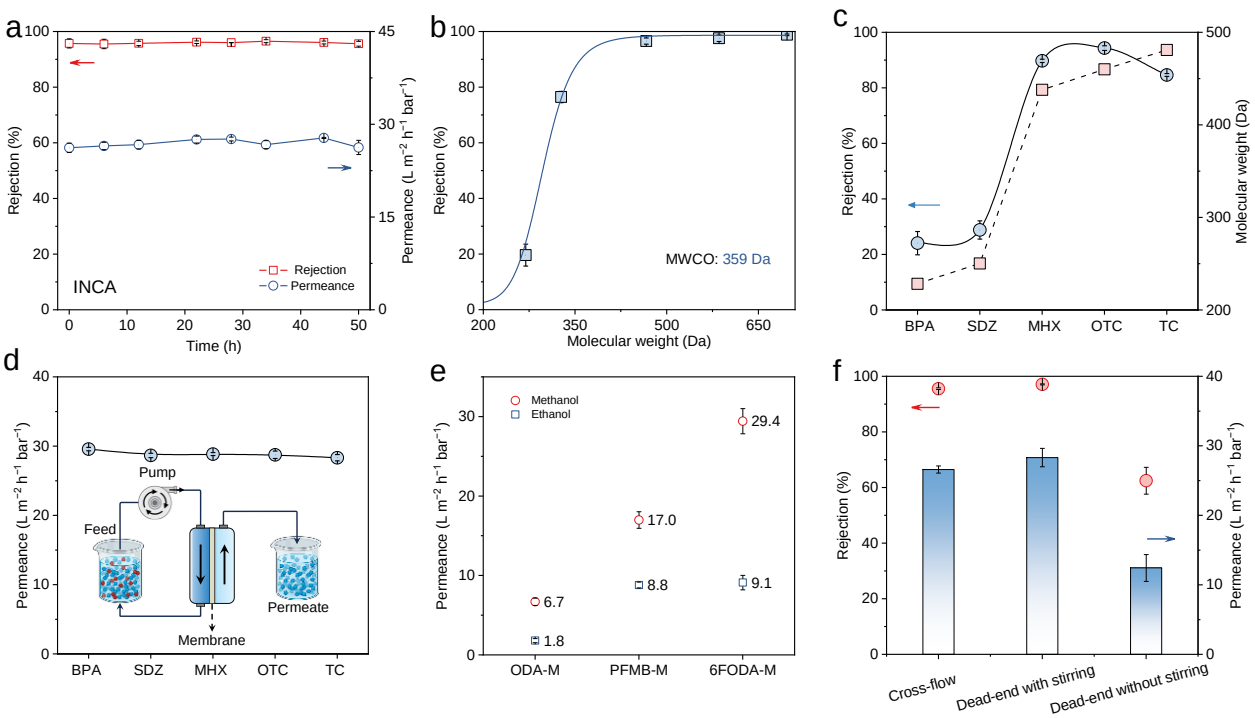


**Supplementary Fig. 64. Organic solvent nanofiltration performance of the polyamide membranes measured under crossflow mode. a** Methanol permeance and INCA rejection of the 6FODA-M membrane during a long-term continuous filtration test of 50 h. **b** Rejection profile of the 6FODA-M membrane as a function of the molecular weight of negatively charged solutes in methanol. **c** Rejection performance of the 6FODA-M membrane for representative pharmaceutical molecules with different molecular weights in methanol. **d** Methanol permeance of the 6FODA-M during the separation of various pharmaceutical molecules. **e** Methanol and ethanol permeance of ODA-M, 6FODA-M, and PFMB-M membranes. **f** Methanol permeance and INCA rejection of the 6FODA-M membrane under three models (crossflow, stirred dead-end, and unstirred dead-end). All filtration tests were conducted at 3 bar. The concentrations of dye and pharmaceutical molecules in methanol were 50 ppm and 5 ppm, respectively. Error bars represent the standard deviation obtained from three independent measurements.

**Supplementary Note 51:** The 6FODA-M membrane exhibits nearly identical separation performance under both stirred dead-end and crossflow filtration modes. The rejection of indigo

carmine (INCA) in methanol consistently exceeds 95.5%, while the permeance remains stable above 26.2 L $m^{-2}$ $h^{-1}$ $bar^{-1}$, with no decrease observed after 50 h of continuous operation. The molecular weight cut-off (MWCO) obtained from the crossflow tests is almost identical to that obtained from the dead-end tests (359 vs. 346 Da). Similarly, for representative small pharmaceuticals and model compounds, the 6FODA-M membrane maintains excellent gradient selectivity and stable high permeance, with low rejections of < 28.8% for bisphenol A (BPA, 228.3 Da) and sulfadiazine (SDZ, 250.3 Da) and high retention rates of 84.6–94.3% for higher molecular weight antibiotics, such as moxifloxacin hydrochloride (MHX, 437.9 Da), oxytetracycline (OTC, 460.4 Da), and tetracycline hydrochloride (TC, 480.8 Da). Furthermore, the methanol and ethanol permeance of ODA-M, 6FODA-M, and PFMB-M membranes measured under crossflow mode are consistent with those obtained in the stirred dead-end system, confirming the reliability of our previously reported data. Conversely, when the 6FODA-M membrane was tested in a non-stirred dead-end mode, a significant decrease in permeance and solute rejection was observed, directly demonstrating the crucial role of strong stirring in minimizing concentration polarization. In our dead-end tests, a high stirring speed of 500 rpm was employed to effectively suppress concentration polarization effects.

**Supplementary Table 1.** Elemental analysis and crosslinking degree calculation of polyamide TFC membranes based on XPS spectra. Each membrane was tested in triplicate.

| Membranes | C (%) | N (%) | O (%) | F (%) | O/N | Crosslinking degree (%) |
|---|---|---|---|---|---|---|
| ODA-M-1 | 75.32 | 9.74 | 14.94 | – | 1.53 | 76.7 |
| ODA-M-2 | 74.15 | 10.08 | 15.77 | – | 1.56 | 72.9 |
| ODA-M-3 | 76.11 | 9.53 | 14.36 | | 1.507 | 79.1 |
| 6FODA-M-1 | 62.02 | 8.94 | 14.42 | 14.62 | 1.61 | 68.2 |
| 6FODA-M-2 | 64.87 | 8.37 | 13.59 | 13.17 | 1.62 | 66.8 |
| 6FODA-M-3 | 63.25 | 8.73 | 14.00 | 14.02 | 1.604 | 69.2 |
| PFMB-M-1 | 64.81 | 7.65 | 12.05 | 15.49 | 1.58 | 32.6 |
| PFMB-M-2 | 63.81 | 7.61 | 12.22 | 16.36 | 1.61 | 30.3 |
| PFMB-M-3 | 63.76 | 7.47 | 12.25 | 16.52 | 1.64 | 27.3 |

**Supplementary Table 2.** Summary of the high-resolution C 1*s*, N 1*s*, and O 1*s* XPS spectra data of polyamide TFC membranes.

| Polyamide | C 1*s* | | | N 1*s* | | | O 1*s* | | |
|---|---|---|---|---|---|---|---|---|---|
| | **Energy (eV)** | **Species** | **(%)** | **Energy (eV)** | **Species** | **(%)** | **Energy (eV)** | **Species** | **(%)** |
| ODA-M | 284.7 | C–H<br>C–C/C=C | 62.47 | | | | | | |
| | | C–N | | 399.9 | N–C=O | 93.45 | 531.4 | N–C=O | 56.57 |
| | 286.1 | C–O | 26.32 | | | | 532.6 | O=C–O$^-$<br>(H$^+$) | 24.43 |
| | 288.0 | O–C=O<br>N–C=O | 11.21 | 401.9 | N$^+$/–<br>NH$_2$ | 6.55 | 533.5 | C–O–C | 19.00 |
| 6FODA-M | 284.7 | C–H<br>C–C/C=C | 57.86 | | | | | | |
| | | C–N | | 399.7 | N–C=O | 88.66 | 531.5 | N–C=O | 54.32 |
| | 286.2 | C–O | 23.21 | | | | 532.6 | O=C–O$^-$<br>(H$^+$) | 27.07 |
| | 288.0 | O–C=O<br>N–C=O | 9.73 | 401.7 | N$^+$/–<br>NH$_2$ | 11.34 | 533.4 | C–O–C | 18.61 |
| | 292.4 | C–F | 9.20 | | | | | | |
| PFMB-M | 284.83 | C–H<br>C–C/C=C | 57.48 | | | | | | |
| | 286.24 | C–N | 22.08 | 399.8 | N–C=O | 79.58 | 531.5 | N–C=O | 56.53 |
| | 287.9 | O–C=O<br>N–C=O | 11.42 | 401.5 | N$^+$/–<br>NH$_2$ | 20.42 | 532.8 | O=C–O$^-$<br>H$^+$) | 43.47 |
| | 292.45 | C–F | 9.02 | | | | | | |

**Supplementary Table 3.** Surface contact angles of polyamide TFC membranes with different probe solvents (in °).

| Membranes | Water | Glycerol | Diiodomethane |
|---|---|---|---|
| ODA-M | 72.9 | 63.0 | 41.6 |
| 6FODA-M | 95.5 | 73.9 | 51.1 |
| PFMB-M | 100.4 | 77.6 | 51.8 |
| 6FODA-M-Acetone | 96.9 | 78.1 | 51.6 |
| 6FODA-M-Hexane | 97.6 | 78.7 | 52.6 |

6FODA-M-Acetone and 6FODA-M-Hexane refer to 6FODA-M membrane treated with acetone for 12 h and 6FODA-M membrane treated with acetone for 12 h and then soaked in hexane for 12 h, respectively.

**Supplementary Table 4.** Summary of the key physicochemical properties of the solvents used in this study.

| Solvents | Molecular weight (Da) | Hansen solubility parameter ($MPa^{1/2}$) | | | | Molar diameter (nm) | Viscosity ($\eta$, $10^{-3}$ Pa·s) |
|---|---|---|---|---|---|---|---|
| | | $\delta_d$ | $\delta_p$ | $\delta_h$ | $\delta$ | | |
| Water | 18.02 | 15.5 | 16 | 42.3 | 48 | 0.38 | 0.89 |
| Methanol | 32.04 | 14.7 | 12.3 | 22.3 | 29.7 | 0.51 | 0.49 |
| Ethanol | 46.07 | 15.8 | 8.8 | 19.4 | 26.6 | 0.57 | 1.17 |
| Acetone | 58.08 | 15.5 | 10.4 | 7 | 20.1 | 0.62 | 0.29 |
| THF | 72.11 | 16.8 | 5.7 | 8 | 19.4 | 0.62 | 0.43 |
| Toluene | 92.13 | 18 | 1.4 | 2 | 18.2 | 0.70 | 0.52 |
| Hexane | 86.18 | 14.9 | 0 | 0 | 14.9 | 0.75 | 0.297 |
| Heptane | 100.21 | 15.3 | 0 | 0 | 15.3 | 0.78 | 0.33 |
| IPA | 60.10 | 15.8 | 6.1 | 16.4 | 23.5 | 0.62 | 2.06 |

**Supplementary Table 5.** Surface tension properties of the probe liquids at 20 °C (in mJ $m^{-2}$)[2].

| Liquid | $\gamma^{LW}$ | $\gamma^{+}$ | $\gamma^{-}$ | $\gamma^{AB}$ | $\gamma^{total}$ |
|---|---|---|---|---|---|
| Water | 21.8 | 25.5 | 25.5 | 51 | 72.8 |
| Glycerol | 34 | 3.92 | 57.4 | 30 | 64 |
| Diiodomethane | 50.8 | 0 | 0 | 0 | 50.8 |
| Hexane | 18.49 | 0 | 0 | 0 | 18.49 |

**Supplementary Table 6.** Surface free energy parameters of the polyamide membranes (in mJ $m^{-2}$).

| Membrane | $\gamma^{LW}$ | $\gamma^{+}$ | $\gamma^{-}$ | $\gamma^{AB}$ | $\gamma^{total}$ |
|---|---|---|---|---|---|
| ODA-M | 38.7966 | 0.3863 | 7.7200 | 3.4537 | 42.2503 |
| 6FODA-M | 33.6580 | 0.4194 | 1.1765 | 1.4049 | 35.0629 |
| PFMB-M | 33.2645 | 0.4500 | 1.1912 | 1.4643 | 34.7288 |
| 6FODA-M-Acetone | 33.3771 | 0.2742 | 0.2275 | 0.4995 | 33.8766 |
| 6FODA-M-Hexane | 32.8124 | 0.2819 | 0.1829 | 0.4541 | 33.2665 |

**Supplementary Table 7.** Gibbs free energy of hexane adhesion to polyamide membranes (in mJ $m^{-2}$).

| Membrane | $\Delta G^{LW}$ | $\Delta G^{AB}$ | $\Delta G^{total}$ |
|---|---|---|---|
| ODA-M | 1.15116 | −67.66149 | −66.51033 |
| 6FODA-M | 0.83592 | −84.50486 | −83.66894 |
| PFMB-M | 0.81079 | −84.20223 | −83.39144 |
| 6FODA-M-Acetone | 0.81799 | −91.89433 | −91.07634 |
| 6FODA-M-Hexane | 0.78176 | −92.31851 | −91.53674 |

**Supplementary Table 8.** Summary of the Hansen solubility parameters (HSP) of the diamine monomers and the corresponding polyamide membranes (estimated by the group contribution method)[3].

| Name | Hansen solubility parameter ($MPa^{1/2}$) | | | |
|---|---|---|---|---|
| | $\delta_d$ | $\delta_p$ | $\delta_h$ | $\delta$ |
| ODA | 8.717 | 1.832 | 3.638 | 13.061 |
| 6FODA | 8.425 | 1.264 | 3.022 | 11.956 |
| PFMB | 12.679 | 1.491 | 3.080 | 11.897 |
| ODA-M | 9.213 | 3.446 | 6.131 | 11.591 |
| 6FODA-M | 8.902 | 2.702 | 5.428 | 10.771 |
| PFMB-M | 9.022 | 2.720 | 5.311 | 10.817 |

**Supplementary Table 9.** Summary of the key physicochemical properties of the model dye molecules used in this study.

| Compound | Dimension | Mw (Da) | van der Waals radius (nm) | Charge (pH=7) |
|---|---|---|---|---|
| Azobenzene (ABZ) | 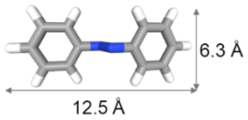 | 182.2 | 0.625 | – |
| Methyl red (MR) | 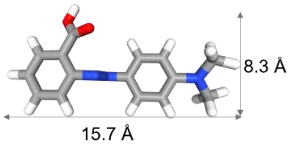 | 269.3 | 0.786 | Negative |
| Methyl orange (MO) | 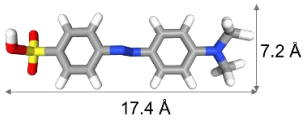 | 327.3 | 0.869 | Negative |
| Orange G (OG) | 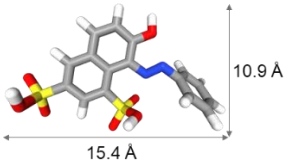 | 452.4 | 0.770 | Negative |
| Eriochrome black T (EBT) | 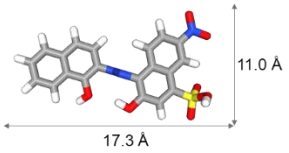 | 461.4 | 0.865 | Negative |
| Indigo carmine (INCA) | 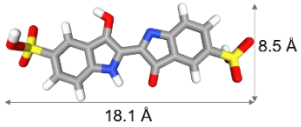 | 466.4 | 0.905 | Negative |
| Acid fuchsin (AF) | 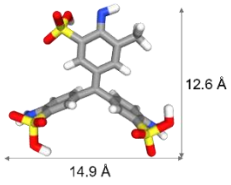 | 585.5 | 0.745 | Negative |
| Congo red (CR) | 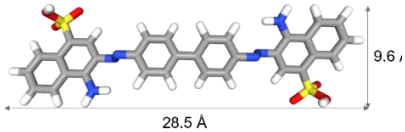 | 696.7 | 1.426 | Negative |

| | | | | |
|---|---|---|---|---|
| Methylene blue (MB) | 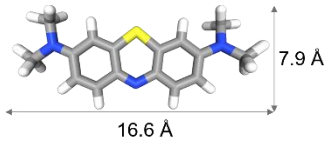 | 319.9 | 0.828 | Positive |
| Crystal violet (CV) | 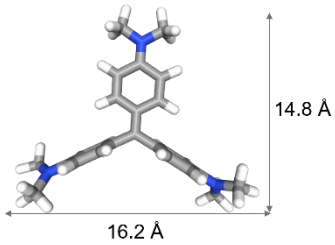 | 408.0 | 0.810 | Positive |
| Rhodamine B (RB) | 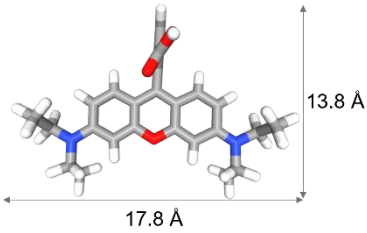 | 479.0 | 0.892 | Positive |
| Victoria blue B | 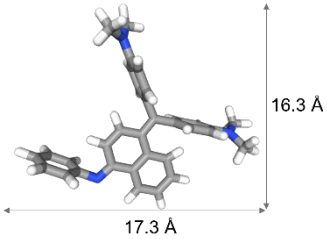 | 506.1 | 0.866 | Positive |
| Alcian blue 8GX (AB) | – | 1298.9 | – | Positive |
| Vitamin B12 (VB12) | – | 1355.4 | – | Positive |

**Supplementary Table 10.** Summary of solvent permeance and MWCO in methanol for the polyamide TFC membranes developed in this study and previously reported OSN membranes.

| Membrane information | Methanol permeance ($L\ m^{-2}\ h^{-1}\ bar^{-1}$) | MWCO (Da) | Reference |
|---|---|---|---|
| PA (smooth) | 8.6 | 246 | [22] |
| PA (crumpled) | 52.2 | 246 | [22] |
| PAR-BHPF | 8 | 314 | [23] |
| PAR-TTSBI | 6 | 314 | [23] |
| PAR-BINOL | 9.2 | 380 | [24] |
| β-CDA-TMC | 4.9 | 400 | [25] |
| CNT-EP-PC | 28 | 540 | [26] |
| Polyamide-CD | 17.6 | 354 | [27] |
| MPCM | 21.8 | 410 | [28] |
| MPDTrip-20 | 8.7 | 200 | [29] |
| MPD-Trip20/PAN | 9.1 | 216 | [29] |
| PA/MOF | 3.9 | 236 | [30] |
| Noria-TPC | 18 | 810 | [31] |
| p-CMP | 22.5 | 562 | [32] |
| m-CMP | 16.4 | 562 | [32] |
| TTB-CMP | 32 | 800 | [33] |
| TTB-CMPO | 21 | 500 | [33] |
| amino-BIPOL | 13 | 233 | [34] |
| Hydroxyl-BIPOL | 17.2 | 314 | [34] |
| α-CDA/TPC | 7.64 | 313 | [35] |
| β-CDA/TPC | 9.84 | 351 | [35] |
| γ-CDA/TPC | 9.87 | 464 | [35] |

| | | | |
|---|---|---|---|
| Polycage/Tren | 20.7 | 486 | [36] |
| Polycage/RCC3 | 23.3 | 620 | [36] |
| TPC-N4 | 6.2 | 825 | [37] |
| IPC-N4 | 5.5 | 808 | [37] |
| DHBIPDA/TPC | 16.4 | 283 | [38] |
| DHBIPDA/TMC | 15.1 | 306 | [38] |
| PEI-TMC/ANF hydrogel | 3.4 | 327 | [39] |
| PEI/TMC after DMF activation/ANF hydrogel | 11 | 506 | [39] |
| PEA/PPD-diphenol | 11.9 | 268 | [3] |
| PEA/APH-diphenol | 14.3 | 296 | [3] |
| PA/MPD | 3 | 281 | [3] |
| ZIF-8, ZIF-93, and UiO-66/Polyimide P84 | 8.5 | 452 | [40] |
| GO Ceramic hollow fiber | 4 | 327 | [41] |
| MPD/TMC/ZIF-8@PI | 3.6 | 452 | [42] |
| ODA-M | 7.1 | 339 | |
| 6FODA-M | 32.5 | 346 | This study |
| PFMB-M | 22.3 | 424 | |

**Supplementary Table 11.** Summary of solvent permeance and MWCO in acetone for the polyamide TFC membranes developed in this study and previously reported OSN membranes.

| Membrane information | Acetone permeance ($L\ m^{-2}\ h^{-1}\ bar^{-1}$) | MWCO (Da) | Reference |
|---|---|---|---|
| PTMSP | 17.3 | 627 | [43] |
| Solsep-NF030306 | 4 | 1000 | [44] |
| Solsep-169 | 40.3 | 880 | [45] |
| MPF-50 | 2.2 | 700 | [45] |
| HITK-T1 | 0.4 | 208 | [45] |
| FSTi-128 | 3 | 624 | [45] |
| Pebax | 14 | 885 | [46] |
| MPD-TMC | 6 | 282 | [47] |
| m-XDA-TMC | 21.4 | 327 | [48] |
| Plant-based monomer polyamide | 13.7 | 235 | [49] |
| PEI | 2.7 | 1500 | [50] |
| PEI | 96.3 | 1111 | [51] |
| PANI | 1.5 | 380 | [52] |
| PANI | 0.5 | 250 | [53] |
| PANI | 1.1 | 236 | [54] |
| PANI | 0.46 | 300 | [55] |
| Polyimide | 6.5 | 520 | [56] |
| Polyimide | 1.8 | 260 | [57] |
| Polyimide | 2.4 | 236 | [58] |
| AF2400 | 1.4 | 150 | [59] |
| Pebax | 0.04 | 370 | [60] |

| | | | |
|---|---|---|---|
| PIM-1 | 5 | 535 | [61] |
| PIM-1 | 46.7 | 521 | [62] |
| PEI/PIP | 11.6 | 585 | [63] |
| Polyarylate | 8.4 | 236 | [23] |
| MPD-TMC | 1.7 | 260 | [1] |
| MPD-SBF | 6.7 | 310 | [1] |
| PPD-TMC | 6.4 | 525 | [1] |
| PPD-SBF | 18.2 | 320 | [1] |
| PIP-TMC | 6.4 | 455 | [1] |
| PIP-SBF | 5.7 | 315 | [1] |
| TBD-TMC | 22.8 | 450 | [1] |
| TBD-SBF | 101 | 639 | [1] |
| 6FODA-M | 78.7 | 498 | This study |

**Supplementary Table 12.** Summary of solvent permeance and MWCO in hexane/heptane for the polyamide TFC membranes developed in this study and previously reported OSN membranes.

| Membrane information | Hexane/heptane permeance ($L\ m^{-2}\ h^{-1}\ bar^{-1}$) | MWCO (Da) | Reference |
|---|---|---|---|
| Priamine-TA | 2.5 | 235 | [49] |
| PIM-1 | 16.4 | 535 | [64] |
| PIM-1 | 4.2 | 240 | [61] |
| PIM-1 | 5.5 | 795 | [65] |
| Epoxysilicones | 6 | 650 | [66] |
| PuraMem 600S | 1 | 595 | [20] |
| ONf-2 | 6 | 695 | [20] |
| $F_5N_6F_5$ | 47.6 | 395 | [20] |
| $F_9N_6F_9$ | 25.4 | 450 | [20] |
| $F_{13}N_6F_{13}$ | 17.5 | 420 | [20] |
| $C_3N_6C_3$ | 18.1 | 395 | [20] |
| $C_6N_6C_6$ | 24.1 | 395 | [20] |
| $C_{10}N_6C_{10}$ | 39 | 395 | [20] |
| 6FODA-M | 47.4 | 338 | This study |

**Supplementary Table 13.** Summary of methanol permeance and membrane thickness of the polyamide TFC membranes developed in this study and previously reported OSN membranes.

| Membrane information | Methanol permeance ($L\ m^{-2}\ h^{-1}\ bar^{-1}$) | Thickness (nm) | Reference |
|---|---|---|---|
| MPD-TMC | 4.8 | 63 | [22] |
| MPD-TMC | 13.3 | 52 | [22] |
| MPD-TMC | 7.7 | 94 | [22] |
| MPD-TMC | 3.9 | 8.4 | [22] |
| MPD-TMC | 9.6 | 8 | [22] |
| PIP-TMC | 1.4 | 33.2 | [22] |
| AMP-TMC | 4.4 | 14.5 | [22] |
| PAR-BHF | 8 | 20 | [23] |
| PAR-TTSBI | 6 | 20 | [23] |
| PAR-DHAQ | 0.6 | 20 | [23] |
| PAR-RES | 0.6 | 20 | [23] |
| Cyclo | 8.6 | 10 | [28] |
| BIPOL | 13 | 5 | [67] |
| BIPOL | 17.2 | 5 | [67] |
| MPD-TMC | 4.8 | 165 | [29] |
| MPD-Trip | 8.7 | 339 | [29] |
| PAR-BINOL | 9 | 17 | [24] |
| v-CDA-TPC | 2 | 20 | [35] |
| v-CDA-TPC | 2.2 | 13 | [35] |
| v-CDA-TPC | 9 | 8 | [35] |
| v-CDA-TPC | 10 | 6 | [35] |
| P[5]a | 4.5 | 8 | [68] |

| | | | |
|---|---|---|---|
| P[6]a | 8.5 | 4.8 | [68] |
| CC3 | 180 | 80 | [69] |
| MPD-TMC | 2 | 256 | [1] |
| MPD-SBF | 5.6 | 262 | [1] |
| PPD-TMC | 5.5 | 202 | [1] |
| PPD-SBF | 9 | 260 | [1] |
| PIP-TMC | 6.4 | 64 | [1] |
| PIP-SBF | 6.7 | 124 | [1] |
| TBD-TMC | 10.6 | 74 | [1] |
| α-CDA-TPC-0.05 | 7.6 | 10 | [35] |
| α-CDA-TPC-0.1 | 5.8 | 14 | [35] |
| β-CDA-TPC-0.05 | 6.3 | 10.4 | [35] |
| β-CDA-TMC-0.1 | 3 | 11 | [35] |
| γ-CDA-TPC-0.05 | 9.9 | 6.2 | [35] |
| γ-CDA-TPC-0.1 | 9.3 | 8 | [35] |
| γ-CDA-TPC-0.2 | 1.9 | 13.1 | [35] |
| γ-CDA-TPC-2 | 1.6 | 20 | [35] |
| SC[4]AA-TPC-0.1 | 3.1 | 24.9 | [35] |
| SC[4]AA-TMC-0.1 | 2.5 | 21.8 | [35] |
| MPD-10%-1 min | 2.45 | 64 | [70] |
| MPD-10%-1min-ACT | 6.6 | 47 | [70] |
| MPD-0.1%-10 min | 3.14 | 8.4 | [70] |
| MPD-0.1%-10 min-ACT | 12.21 | 8 | [70] |
| MPD-0.1%-10 min | 3.89 | 8.4 | [70] |
| MPD-0.1%-10 min-ACT | 9.55 | 8 | [70] |
| MPDTrip-20 | 8.7 | 339 | [29] |

| | | | |
|---|---|---|---|
| hydroxyl-BIPOL | 13 | 14 | [34] |
| PAR/TMC-0.05-PN-0.2 | 7.1 | 61 | [71] |
| PAR/TMC-0.05-TN-0.2 | 7.4 | 43 | [71] |
| PAR/TMC-0.05-PXN-0.2 | 5.9 | 60 | [71] |
| PAR/TMC-0.1-PN-0.2 | 9.9 | 75 | [71] |
| PAR/TMC-0.1-PXN-0.2 | 5.8 | 62 | [71] |
| PAR/TMC-0.2-PXN-0.2 | 5.5 | 55 | [71] |
| ODA-M | 7.1 | 13.1 | |
| 6FODA-M | 32.5 | 13.6 | This study |
| PFMB-M | 22.3 | 18.5 | |

**Supplementary Table 14.** Summary of the key physicochemical properties of the model pharmaceutical and industrial compound molecules used for membrane performance testing in this study.

| Compound | Dimension | Molecular weight (Da) | van der Waals radius (nm) | Charge (pH=7) |
|---|---|---|---|---|
| Bisphenol A (BPA) | 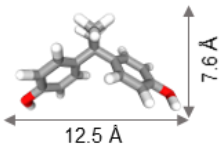 | 228.3 | 0.63 | – |
| Sulfadiazine (SDZ) | 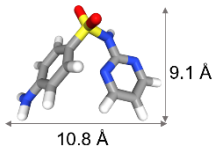 | 250.3 | 0.54 | Negative |
| Ciprofloxacin (CIP) | 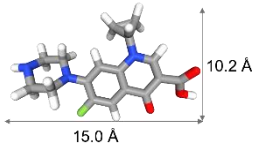 | 331.3 | 0.75 | – |
| Carbenicillin disodium (CBD) | 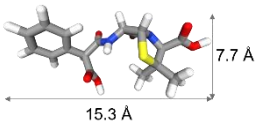 | 422.4 | 0.77 | Negative |
| Moxifloxacin hydrochloride (MHX) | 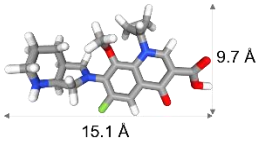 | 437.9 | 0.76 | Negative |
| Doxycycline (DC) | 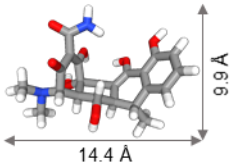 | 444.4 | 0.72 | – |
| Oxytetracycline (OTC) | 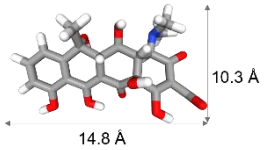 | 460.4 | 0.74 | – |

| | | | | |
|---|---|---|---|---|
| Cefotaxime sodium salt (CS) | 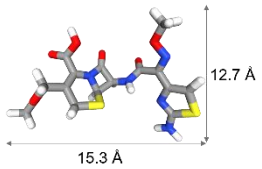 | 477.5 | 0.77 | Negative |
| Tetracycline hydrochloride (TC) | 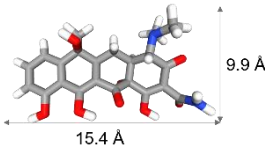 | 480.8 | 0.77 | Negative |
| Clindamycin phosphate (CLP) | 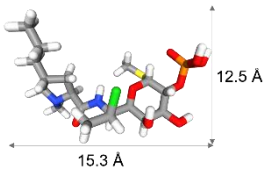 | 505.0 | 0.76 | Positive |

**Supplementary References**


1. Lee TH, Balcik M, Wu W-N, Pinnau I, Smith ZP. Dual-phase microporous polymer nanofilms by interfacial polymerization for ultrafast molecular separation. *Sci. Adv.* **10**, eadp6666 (2024).
2. Chen M*, et al.* Enhanced Antifouling Capability of In Situ-Grown Hydrophilic–Hydrophobic Nanodomains on Membrane Surface in the Ultralow Pressurized Ultrafiltration Process. *Environ. Sci. Technol.* **58**, 16204-16214 (2024).
3. Liu Z, Sun Y, Han H, Zhang Q, Li S, Zhang S. Microporous and functional group Co-designed polyesteramide membranes for efficient and broad-spectrum organic solvent nanofiltration. *Adv. Membr.* **4**, 100098 (2024).
4. Neese F, Wennmohs F, Becker U, Riplinger C. The ORCA quantum chemistry program package. *J. Chem. Phys.* **152**, 224108 (2020).
5. Lee C, Yang W, Parr RG. Development of the Colle-Salvetti correlation-energy formula into a functional of the electron density. *Phys. Rev. B* **37**, 785-789 (1988).
6. Grimme S, Antony J, Ehrlich S, Krieg H. A consistent and accurate ab initio parametrization of density functional dispersion correction (DFT-D) for the 94 elements H-Pu. *J. Chem. Phys.* **132**, 154104 (2010).
7. Stoychev GL, Auer AA, Neese F. Automatic Generation of Auxiliary Basis Sets. *J. Chem. Theory Comput.* **13**, 554-562 (2017).
8. Lu T, Manzetti S. Wavefunction and reactivity study of benzo[a]pyrene diol epoxide and its enantiomeric forms. *Struct. Chem.* **25**, 1521-1533 (2014).
9. Zhang J, Lu T. Efficient evaluation of electrostatic potential with computerized optimized code. *Phys. Chem. Chem. Phys.* **23**, 20323-20328 (2021).
10. Lu T, Chen F. Multiwfn: A multifunctional wavefunction analyzer. *J. Comput. Chem.* **33**, 580-592 (2012).
11. Momma K, Izumi F. VESTA 3 for three-dimensional visualization of crystal, volumetric

and morphology data. *J. Appl. Crystallogr.* **44**, 1272-1276 (2011).

12. Wang J, Wolf RM, Caldwell JW, Kollman PA, Case DA. Development and testing of a general amber force field. *J. Comput. Chem.* **25**, 1157-1174 (2004).
13. Hess B, Kutzner C, van der Spoel D, Lindahl E. GROMACS 4: Algorithms for Highly Efficient, Load-Balanced, and Scalable Molecular Simulation. *J. Chem. Theory Comput.* **4**, 435-447 (2008).
14. Willems TF, Rycroft CH, Kazi M, Meza JC, Haranczyk M. Algorithms and tools for high-throughput geometry-based analysis of crystalline porous materials. *Microporous Mesoporous Mater.* **149**, 134-141 (2012).
15. Berendsen HJC, Postma JPM, van Gunsteren WF, DiNola A, Haak JR. Molecular dynamics with coupling to an external bath. *J. Chem. Phys.* **81**, 3684-3690 (1984).
16. Essmann U, Perera L, Berkowitz ML, Darden T, Lee H, Pedersen LG. A smooth particle mesh Ewald method. *J. Chem. Phys.* **103**, 8577-8593 (1995).
17. Hess B, Bekker H, Berendsen HJC, Fraaije JGEM. LINCS: A linear constraint solver for molecular simulations. *J. Comput. Chem.* **18**, 1463-1472 (1997).
18. Van Gunsteren WF, and Berendsen HJC. A Leap-frog Algorithm for Stochastic Dynamics. *Mol. Simul.* **1**, 173-185 (1988).
19. Guo B-B*, et al.* Double charge flips of polyamide membrane by ionic liquid-decoupled bulk and interfacial diffusion for on-demand nanofiltration. *Nat. Commun.* **15**, 2282 (2024).
20. Li S*, et al.* Hydrophobic polyamide nanofilms provide rapid transport for crude oil separation. *Science* **377**, 1555-1561 (2022).
21. Itoh Y*, et al.* Ultrafast water permeation through nanochannels with a densely fluorous interior surface. *Science* **376**, 738-743 (2022).
22. Karan S, Jiang Z, Livingston AG. Sub–10 nm polyamide nanofilms with ultrafast solvent transport for molecular separation. *Science* **348**, 1347-1351 (2015).
23. Jimenez-Solomon MF, Song Q, Jelfs KE, Munoz-Ibanez M, Livingston AG. Polymer

nanofilms with enhanced microporosity by interfacial polymerization. *Nat. Mater.* **15**, 760-767 (2016).

24. Fu W, Zhang W, Chen H, Li S-L, Shi W, Hu Y. A high-flux organic solvent nanofiltration membrane with binaphthol-based rigid-flexible microporous structures. *J. Mater. Chem. A* **9**, 7180-7189 (2021).
25. Liu J, Hua D, Zhang Y, Japip S, Chung T-S. Precise Molecular Sieving Architectures with Janus Pathways for Both Polar and Nonpolar Molecules. *Adv. Mater.* **30**, 1705933 (2018).
26. Zhou Z*, et al.* Electropolymerization of robust conjugated microporous polymer membranes for rapid solvent transport and narrow molecular sieving. *Nat. Commun.* **11**, 5323 (2020).
27. Huang T, Puspasari T, Nunes SP, Peinemann K-V. Ultrathin 2D-Layered Cyclodextrin Membranes for High-Performance Organic Solvent Nanofiltration. *Adv. Funct. Mater.* **30**, 1906797 (2020).
28. Huang T*, et al.* Molecularly-porous ultrathin membranes for highly selective organic solvent nanofiltration. *Nat. Commun.* **11**, 5882 (2020).
29. Ali Z*, et al.* Finely Tuned Submicroporous Thin-Film Molecular Sieve Membranes for Highly Efficient Fluid Separations. *Adv. Mater.* **32**, 2001132 (2020).
30. Sorribas S, Gorgojo P, Téllez C, Coronas J, Livingston AG. High Flux Thin Film Nanocomposite Membranes Based on Metal–Organic Frameworks for Organic Solvent Nanofiltration. *J. Am. Chem. Soc.* **135**, 15201-15208 (2013).
31. Zhai Z*, et al.* Polyarylate membrane constructed from porous organic cage for high-performance organic solvent nanofiltration. *J. Membr. Sci.* **595**, 117505 (2020).
32. Liang B*, et al.* Microporous membranes comprising conjugated polymers with rigid backbones enable ultrafast organic-solvent nanofiltration. *Nat. Chem.* **10**, 961-967 (2018).
33. He X*, et al.* Controlling the Selectivity of Conjugated Microporous Polymer Membrane for Efficient Organic Solvent Nanofiltration. *Adv. Funct. Mater.* **29**, 1900134 (2019).

34. Li S-L*, et al.* 2,2′-Biphenol-based Ultrathin Microporous Nanofilms for Highly Efficient Molecular Sieving Separation. *Angew. Chem. Int. Ed.* **61**, e202212816 (2022).

35. Jiang Z*, et al.* Aligned macrocycle pores in ultrathin films for accurate molecular sieving. *Nature* **609**, 58-64 (2022).

36. Li X*, et al.* Polycage membranes for precise molecular separation and catalysis. *Nat. Commun.* **14**, 3112 (2023).

37. Yao A*, et al.* Flexible Covalent Organic Network with Ordered Honeycomb Nanoarchitecture for Molecular Separations. *ACS Nano* **17**, 22916-22927 (2023).

38. Chen Y*, et al.* Rapid and Precise Molecular Nanofiltration Using Ultra-Thin-Film Membranes Derived from 6,6′-Dihydroxy-2,2′-biphenyldiamine. *Adv. Funct. Mater.* **34**, 2406430 (2024).

39. Li Y, Zhu J, Li S, Guo Z, Van der Bruggen B. Flexible Aliphatic–Aromatic Polyamide Thin Film Composite Membrane for Highly Efficient Organic Solvent Nanofiltration. *ACS Appl. Mater. Interfaces* **12**, 31962-31974 (2020).

40. Yang H, Wang N, Wang L, Liu H-X, An Q-F, Ji S. Vacuum-assisted assembly of ZIF-8@GO composite membranes on ceramic tube with enhanced organic solvent nanofiltration performance. *J. Membr. Sci.* **545**, 158-166 (2018).

41. Aba NFD, Chong JY, Wang B, Mattevi C, Li K. Graphene oxide membranes on ceramic hollow fibers – Microstructural stability and nanofiltration performance. *J. Membr. Sci.* **484**, 87-94 (2015).

42. Sarango L, Paseta L, Navarro M, Zornoza B, Coronas J. Controlled deposition of MOFs by dip-coating in thin film nanocomposite membranes for organic solvent nanofiltration. *J. Ind. Eng. Chem.* **59**, 8-16 (2018).

43. Volkov AV, Parashchuk VV, Stamatialis DF, Khotimsky VS, Volkov VV, Wessling M. High permeable PTMSP/PAN composite membranes for solvent nanofiltration. *J. Membr. Sci.* **333**, 88-93 (2009).

44. Darvishmanesh S, Robberecht T, Luis P, Degrève J, Van der Bruggen B. Performance of Nanofiltration Membranes for Solvent Purification in the Oil Industry. *J. Am. Oil Chem. Soc.* **88**, 1255-1261 (2011).

45. Geens J, Boussu K, Vandecasteele C, Van der Bruggen B. Modelling of solute transport in non-aqueous nanofiltration. *J. Membr. Sci.* **281**, 139-148 (2006).

46. Zwijnenberg HJ, Krosse AM, Ebert K, Peinemann KV, Cuperus FP. Acetone-stable nanofiltration membranes in deacidifying vegetable oil. *J. Am. Oil Chem. Soc.* **76**, 83-87 (1999).

47. Kim I-C, Jegal J, Lee K-H. Effect of aqueous and organic solutions on the performance of polyamide thin-film-composite nanofiltration membranes. *J. Polym. Sci., Part B: Polym. Phys.* **40**, 2151-2163 (2002).

48. Li Y, Li S, Zhu J, Volodine A, Van der Bruggen B. Controllable synthesis of a chemically stable molecular sieving nanofilm for highly efficient organic solvent nanofiltration. *Chem. Sci.* **11**, 4263-4271 (2020).

49. Park S-H, Alammar A, Fulop Z, Pulido BA, Nunes SP, Szekely G. Hydrophobic thin film composite nanofiltration membranes derived solely from sustainable sources. *Green Chem.* **23**, 1175-1184 (2021).

50. Ding R*, et al.* Graphene oxide-embedded nanocomposite membrane for solvent resistant nanofiltration with enhanced rejection ability. *Chem. Eng. Sci.* **138**, 227-238 (2015).

51. Wu X*, et al.* Adsorption-Assisted Interfacial Polymerization toward Ultrathin Active Layers for Ultrafast Organic Permeation. *ACS Appl. Mater. Interfaces* **10**, 10445-10453 (2018).

52. Loh XX, Sairam M, Steinke JHG, Livingston AG, Bismarck A, Li K. Polyaniline hollow fibres for organic solvent nanofiltration. *Chem. Commun.*, 6324-6326 (2008).

53. Sairam M*, et al.* Spiral-wound polyaniline membrane modules for organic solvent nanofiltration (OSN). *J. Membr. Sci.* **349**, 123-129 (2010).

54. Loh XX, Sairam M, Bismarck A, Steinke JHG, Livingston AG, Li K. Crosslinked integrally skinned asymmetric polyaniline membranes for use in organic solvents. *J. Membr. Sci.* **326**, 635-642 (2009).

55. Sarihan A, Shahid S, Shen J, Amura I, Patterson DA, Emanuelsson EAC. Exploiting the electrical conductivity of poly-acid doped polyaniline membranes with enhanced durability for organic solvent nanofiltration. *J. Membr. Sci.* **579**, 11-21 (2019).

56. Siddique H, Bhole Y, Peeva LG, Livingston AG. Pore preserving crosslinkers for polyimide OSN membranes. *J. Membr. Sci.* **465**, 138-150 (2014).

57. Dutczak SM, Cuperus FP, Wessling M, Stamatialis DF. New crosslinking method of polyamide–imide membranes for potential application in harsh polar aprotic solvents. *Sep. Purif. Technol.* **102**, 142-146 (2013).

58. Jimenez Solomon MF, Bhole Y, Livingston AG. High flux membranes for organic solvent nanofiltration (OSN)—Interfacial polymerization with solvent activation. *J. Membr. Sci.* **423-424**, 371-382 (2012).

59. Shi GM, Chung T-S. Teflon AF2400/polyethylene membranes for organic solvent nanofiltration (OSN). *J. Membr. Sci.* **602**, 117972 (2020).

60. Li X*, et al.* Ordered nanoporous membranes based on diblock copolymers with high chemical stability and tunable separation properties. *J. Mater. Chem.* **20**, 4333-4339 (2010).

61. Fritsch D, Merten P, Heinrich K, Lazar M, Priske M. High performance organic solvent nanofiltration membranes: Development and thorough testing of thin film composite membranes made of polymers of intrinsic microporosity (PIMs). *J. Membr. Sci.* **401-402**, 222-231 (2012).

62. Xu Q, Jiang J. Effects of functionalization on the nanofiltration performance of PIM-1: Molecular simulation investigation. *J. Membr. Sci.* **591**, 117357 (2019).

63. Goh KS, Chong JY, Chen Y, Fang W, Bae T-H, Wang R. Thin-film composite hollow fibre membrane for low pressure organic solvent nanofiltration. *J. Membr. Sci.* **597**, 117760

(2020).

64. Gorgojo P, Karan S, Wong HC, Jimenez-Solomon MF, Cabral JT, Livingston AG. Ultrathin Polymer Films with Intrinsic Microporosity: Anomalous Solvent Permeation and High Flux Membranes. *Adv. Funct. Mater.* **24**, 4729-4737 (2014).

65. Cook M, Gaffney PRJ, Peeva LG, Livingston AG. Roll-to-roll dip coating of three different PIMs for Organic Solvent Nanofiltration. *J. Membr. Sci.* **558**, 52-63 (2018).

66. Cook M, Peeva L, Livingston A. Solvent-Free Coating of Epoxysilicones for the Fabrication of Composite Membranes. *Ind. Eng. Chem. Res.* **57**, 730-739 (2018).

67. Shi X*, et al.* Design of Three-Dimensional Covalent Organic Framework Membranes for Fast and Robust Organic Solvent Nanofiltration. *Angew. Chem. Int. Ed.* **61**, e202207559 (2022).

68. Fu W, Huang Y, Deng L, Sun J, Li S-L, Hu Y. Ultra-thin microporous membranes based on macrocyclic pillar[n]arene for efficient organic solvent nanofiltration. *J. Membr. Sci.* **655**, 120583 (2022).

69. He A*, et al*. A smart and responsive crystalline porous organic cage membrane with switchable pore apertures for graded molecular sieving. *Nat. Mater.* **21**, 463-470 (2022).

70. Zhang Y*, et al.* Robust natural nanocomposites realizing unprecedented ultrafast precise molecular separations. *Mater. Today* **36**, 40-47 (2020).

71. Yao A*, et al.* Microporous polyarylate membranes based on 3D phenolphthalein for molecular sieving. *Sci. Adv.* **10**, eado7687 (2024).